

1

²A SEARCH FOR LONG-LIVED, CHARGED, SUPERSYMMETRIC PARTICLES
³USING IONIZATION WITH THE ATLAS DETECTOR

4

BRADLEY AXEN

5

September 2016 – Version 0.54

6



⁸ Bradley Axen: *A Search for Long-Lived, Charged, Supersymmetric Particles using*
⁹ *Ionization with the ATLAS Detector*, Subtitle, © September 2016

¹⁰

Usually a quotation.

¹¹

Dedicated to.

₁₂ ABSTRACT

₁₃ How to write a good abstract:

₁₄ <https://plg.uwaterloo.ca/~migod/research/beck00PSLA.html>

₁₅ PUBLICATIONS

₁₆ Some ideas and figures have appeared previously in the following publications:

₁₇

₁₈ Put your publications from the thesis here. The packages `multibib` or `bibtopic`
₁₉ etc. can be used to handle multiple different bibliographies in your document.

²¹ ACKNOWLEDGEMENTS

²² Put your acknowledgements here.

²³

²⁴ And potentially a second round.

²⁵

26 CONTENTS

27	I	INTRODUCTION	1
28	1	INTRODUCTION	3
29	II	THEORETICAL CONTEXT	5
30	2	STANDARD MODEL	7
31	2.1	Action and the Lagrangian	7
32	2.2	Gauge Invariance and Forces	8
33	2.2.1	$SU(2) \times U(1)$ and the Electroweak Force	10
34	2.2.2	$SU(3)$ and the Strong Force	10
35	2.3	Noether's Theorem, Charges, and Matter	10
36	2.3.1	Quarks	11
37	2.3.2	Leptons	12
38	2.3.3	Chirality	12
39	2.4	Higgs Mechanism and Mass	13
40	2.5	Phenomenology	14
41	2.5.1	Electroweak Physics	14
42	2.5.2	Strong Physics	15
43	2.5.3	Proton-Proton Collisions	15
44	2.6	Limitations	16
45	2.6.1	Theoretical Concerns	16
46	2.6.2	Cosmological Observations	18
47	3	SUPERSYMMETRY	21
48	3.1	Structure and the MSSM	21
49	3.2	Motivation	22
50	4	LONG-LIVED PARTICLES	23
51	4.1	Mechanisms	23
52	4.1.1	Examples in Supersymmetry	23
53	4.2	Phenomenology	23
54	4.2.1	Disimilarities to Prompt Decays	23
55	4.2.2	Characteristic Signatures	23
56	III	EXPERIMENTAL STRUCTURE AND RECONSTRUCTION	25
57	5	THE LARGE HADRON COLLIDER	27
58	5.1	Injection Chain	28
59	5.2	Design	29
60	5.2.1	Layout	29
61	5.2.2	Magnets	30
62	5.2.3	RF Cavities	31
63	5.2.4	Beam	33
64	5.3	Luminosity Parameters	33
65	5.4	Delivered Luminosity	34

66	6	THE ATLAS DETECTOR	37
67	6.1	Coordinate System	39
68	6.2	Magnetic Field	40
69	6.3	Inner Detector	42
70	6.3.1	Pixel Detector	45
71	6.3.2	Semiconductor Tracker	47
72	6.3.3	Transition Radiation Tracker	49
73	6.4	Calorimetry	50
74	6.4.1	Electromagnetic Calorimeter	52
75	6.4.2	Hadronic Calorimeters	53
76	6.5	Muon Spectrometer	55
77	6.5.1	Monitored Drift Tube	57
78	6.5.2	Resistive Plate Chamber	58
79	6.5.3	Cathode Strip Chamber	58
80	6.5.4	Thin Gap Chamber	58
81	6.6	Trigger	60
82	7	EVENT RECONSTRUCTION	63
83	7.1	Tracks and Vertices	63
84	7.1.1	Pixel Neural Network	65
85	7.1.2	Pixel dE/dx	66
86	7.1.3	Vertex Reconstruction	66
87	7.2	Electrons and Photons	67
88	7.2.1	Photon Identification	68
89	7.2.2	Electron Identification	68
90	7.3	Muons	68
91	7.3.1	Muon Identification	69
92	7.4	Jets	69
93	7.4.1	Topological Clustering	70
94	7.4.2	Jet Algorithms	71
95	7.4.3	Jet Energy Scale	72
96	7.5	Missing Transverse Energy	72
97	IV	CALORIMETER RESPONSE	75
98	8	RESPONSE MEASUREMENT WITH SINGLE HADRONS	77
99	8.1	Dataset and Simulation	78
100	8.1.1	Data Samples	78
101	8.1.2	Simulated Samples	78
102	8.1.3	Event Selection	78
103	8.2	Inclusive Hadron Response	79
104	8.2.1	E/p Distribution	79
105	8.2.2	Zero Fraction	80
106	8.2.3	Neutral Background Subtraction	81
107	8.2.4	Corrected Response	83
108	8.2.5	Additional Studies	85
109	8.3	Identified Particle Response	88
110	8.3.1	Decay Reconstruction	88

111	8.3.2	Identified Response	89
112	8.3.3	Additional Species in Simulation	91
113	8.4	Summary	92
114	9	JET ENERGY RESPONSE AND UNCERTAINTY	95
115	9.1	Motivation	95
116	9.2	Uncertainty Estimate	95
117	9.3	Summary	98
118	V	SEARCH FOR LONG-LIVED PARTICLES	101
119	10	LONG-LIVED PARTICLES IN ATLAS	103
120	10.1	Event Topology	103
121	10.1.1	Detector Interactions	104
122	10.1.2	Lifetime Dependence	105
123	10.2	Simulation	108
124	11	EVENT SELECTION	111
125	11.1	Trigger	112
126	11.2	Kinematics and Isolation	113
127	11.3	Particle Species Rejection	117
128	11.4	Ionization	120
129	11.4.1	Mass Estimation	121
130	11.5	Efficiency	122
131	12	BACKGROUND ESTIMATION	125
132	12.1	Background Sources	125
133	12.2	Prediction Method	126
134	12.3	Validation	127
135	12.3.1	Closure in Simulation	127
136	12.3.2	Validation Region in Data	128
137	13	SYSTEMATIC UNCERTAINTIES AND RESULTS	131
138	13.1	Systematic Uncertainties	131
139	13.1.1	Background Estimate	131
140	13.1.2	Signal Yield	132
141	13.2	Final Yields	138
142	13.3	Cross Sectional Limits	139
143	13.4	Mass Limits	141
144	13.5	Context for Long-Lived Searches	143
145	VI	CONCLUSIONS	147
146	14	SUMMARY AND OUTLOOK	149
147	14.1	Summary	149
148	14.2	Outlook	149
149	VII	APPENDIX	151
150	A	INELASTIC CROSS SECTION	153
151	B	EXPANDED R-HADRON YIELDS AND LIMITS	155
152		BIBLIOGRAPHY	161

153 LIST OF FIGURES

154	Figure 1	A Feynman diagram representing the interaction of the A field with a generic fermion, f	10
155			
156	Figure 2	The particle content of the Standard Model (SM)	12
157	Figure 3		
158			
159			
160			
161	Figure 4	The Feynman diagrams representing the decays of the W and Z bosons to fermions. Here f indicates a generic fermion, \bar{f} its antiparticle, and f' the partner of that fermion in the same generation.	15
162			
163			
164			
165			
166	Figure 5	The parton distribution functions (PDFs) for proton-proton collisions at $Q^2 = 10 \text{ GeV}^2$ and $Q^2 = 10^4 \text{ GeV}^2$. Each shows the fraction of particles which carry a fraction x of the total proton energy at the specified scale [1].	16
167			
168	Figure 6	An approximation of the running of the coupling constants in the SM up to the Planck scale [unification_plot].	17
169			
170			
171			
172	Figure 7	The distribution of velocities of stars as a function of the radius from the center of the galaxy. The contributions to the velocity from the various components of matter in the galaxy are shown [2].	18
173			
174			
175			
176	Figure 8	The four collision points and corresponding experiments of the Large Hadron Collider (LHC). The image includes the location of the nearby city of Geneva as well as the border of France and Switzerland.	28
177			
178			
179			
180			
181	Figure 9	The cumulative luminosity over time delivered to the A Toroidal LHC ApparatuS (ATLAS) experiment from high energy proton-proton collisions since 2011. The energies of the collisions are listed for each of the data-taking periods.	29
182			
183			
184			
185	Figure 10	The accelerator complex that builds up to the full design energies at the LHC . The protons are passed in order to Linac 2, the PSB , the PS , the SPS and then the LHC	30
186			
187			
188			
189	Figure 11	A schematic of the layout of the LHC , not to scale. The arched and straight sections are illustrated at the bottom of the schematic, and all four crossing sites are indicated with their respective experiments.	31
190			
191			
192			
193			
194			
		A cross section of the the cryodipole magnets which bend the flight path of protons around the circumference of the LHC . The diagram includes both the superconducting coils which produce the magnetic field and the structural elements which keep the magnets precisely aligned.	32

195	Figure 12	The arrangement of four radiofrequency (RF) cavities within a cryomodule.	32
196			
197	Figure 13	The cumulative luminosity versus time delivered to ATLAS (green), recorded by ATLAS (yellow), and certified to be good quality data (blue) during stable beams for pp collisions at 13 TeV in 2015.	35
198			
199			
200			
201	Figure 14	The luminosity-weighted distribution of the mean number of interactions per crossing for the 2015 pp collision data at 13 TeV.	36
202			
203			
204	Figure 15	A cut-away schematic of the layout of the ATLAS detector. Each of the major subsystems is indicated.	38
205			
206	Figure 16	A cross-sectional slice of the ATLAS experiment which illustrates how the various SM particles interact with the detector systems.	38
207			
208			
209	Figure 17	The layout of the four superconducting magnets in the ATLAS detector.	41
210			
211	Figure 18	The arrangement of the subdetectors of the ATLAS inner detector. Each of the subdetectors is labeled in the cut-away view of the system.	43
212			
213			
214	Figure 19	A quarter section of the ATLAS inner detector which shows the layout of each of the subdetectors in detail. The lower panel shows an enlarged view of the pixel detector. Example trajectories for a particle with $\eta = 1.0, 1.5, 2.0, 2.5$ are shown. The Insertible B-Layer (IBL), which was added after the original detector commissioning, is not shown.	43
215			
216			
217			
218			
219			
220			
221	Figure 20	A computer generated three-dimensional view of the inner detector along the line of the beam axis. The subdetectors and their positions are labeled.	44
222			
223			
224	Figure 21	An alternative computer generated three-dimensional view of the inner detector transverse to the beam axis. The subdetectors and their positions are labeled.	44
225			
226			
227	Figure 22	The integrated radiation lengths traversed by a straight track at the exit of the ID envelope, including the services and thermal enclosures. The distribution is shown as a function of $ \eta $ and averaged over ϕ . The breakdown indicates the contributions of individual subdetectors, including services in their active volume.	45
228			
229			
230			
231			
232			
233	Figure 23	48
234	Figure 24	An image of the insertion of the IBL into the current pixel detector.	48
235			
236	Figure 25	A three-dimensional computer-generated image of the geometry of the IBL with a view (a) mostly transverse to the beam pipe (b) mostly parallel to the beam pipe.	49
237			
238			
239	Figure 26	An exploded view of the geometry of the silicon microstrip (SCT) double layers in the barrel region.	50
240			

241	Figure 27	51
242	Figure 28	The depth of (a) the electromagnetic barrel calorimeter in radiation lengths and (b) all calorimeters in interaction lengths as a function of pseudorapidity.	52
243			
244			
245	Figure 29	A schematic of the Liquid Argon (LAr) calorimeter in the barrel region, highlighting the accordion structure.	52
246			
247	Figure 30	A schematic of a hadronic tile module which shows the alternating layers of steel and plastic scintillator.	54
248			
249	Figure 31	The segmentation in depth and η of the tile-calorimeter modules in the central (left) and extended (right) barrels.	54
250			
251	Figure 32	A cut-away diagram of the muon systems on ATLAS	55
252	Figure 33	A quarter view of the muon spectrometer which highlights the layout of each of the detecting elements. The BOL, BML, BIL, EOL, EML, and EIL are all Monitored Drift Tube (MDT) elements, where the acronyms encode their positions.	56
253			
254			
255			
256			
257	Figure 34	A schematic of the cross-section of the muon spectrometer in the barrel region.	56
258			
259	Figure 35	A schematic of a single MDT chamber, which shows the multilayers of drift tubes as well as the alignment system.	57
260			
261			
262	Figure 36	A schematic of the Cathode Strip Chamber (CSC) end-cap, showing the overlapping arrangement of the eight large and eight small chambers.	59
263			
264			
265	Figure 37	A schematic of the Thin Gap Chamber (TGC) doublet and triplet layers.	59
266			
267	Figure 38	The L1 Trigger rate broken down into the types of triggers as a function of the luminosity block for the 2015 data collection period.	61
268			
269			
270	Figure 39	The HLT Trigger rate broken down into the types of triggers as a function of the luminosity block for the 2015 data collection period.	62
271			
272			
273	Figure 40	The x and y locations of the hits generated in a simulated $t\bar{t}$ event in the inner detector. The hits which belong to tracks formed using the inside-out algorithm are highlighted in red, while the hits which belong to tracks formed using the outside-in algorithm are circled in black.	64
274			
275			
276			
277			
278			
279	Figure 41	Examples of the clusters formed in a single layer of the pixel detector for (a) a single isolated particle, (b) two nearly-overlapping particles, and (c) a particle which emits a δ -ray [15].	65
280			
281			
282			
283	Figure 42	The total, fractional jet energy scale (JES) uncertainties estimated for 2015 data as a function of jet p_T	73
284			

285	Figure 43	An illustration (a) of the E/p variable used throughout this paper. The red energy deposits come from the charged particle targeted for measurement, while the blue energy deposits are from nearby neutral particles and must be subtracted. The same diagram (b) for the neutral-background selection, described in Section 8.2.3.	80
286			
287			
288			
289			
290			
291	Figure 44	The E/p distribution and ratio of simulation to data for isolated tracks with (a) $ \eta < 0.6$ and $1.2 < p/\text{GeV} < 1.8$ and (b) $ \eta < 0.6$ and $2.2 < p/\text{GeV} < 2.8$	80
292			
293			
294	Figure 45	The fraction of tracks as a function (a, b) of momentum, (c, d) of interaction lengths with $E \leq 0$ for tracks with positive (on the left) and negative (on the right) charge.	82
295			
296			
297			
298	Figure 46	$\langle E/p \rangle_{\text{BG}}$ as a function of the track momentum for tracks with (a) $ \eta < 0.6$, (b) $0.6 < \eta < 1.1$, and as a function of the track pseudorapidity for tracks with (c) $1.2 < p/\text{GeV} < 1.8$, (d) $1.8 < p/\text{GeV} < 2.2$	83
299			
300			
301			
302	Figure 47	$\langle E/p \rangle_{\text{COR}}$ as a function of track momentum, for tracks with (a) $ \eta < 0.6$, (b) $0.6 < \eta < 1.1$, (c) $1.8 < \eta < 1.9$, and (d) $1.9 < \eta < 2.3$	84
303			
304			
305	Figure 48	$\langle E/p \rangle_{\text{COR}}$ calculated using LCW-calibrated topological clusters as a function of track momentum for tracks with (a) zero or more associated topological clusters or (b) one or more associated topological clusters.	85
306			
307			
308			
309	Figure 49	Comparison of the $\langle E/p \rangle_{\text{COR}}$ for tracks with (a) less than and (b) greater than 20 hits in the TRT.	86
310			
311	Figure 50	Comparison of the $\langle E/p \rangle_{\text{COR}}$ for (a) positive and (b) negative tracks as a function of track momentum for tracks with $ \eta < 0.6$	86
312			
313			
314	Figure 51	Comparison of the E/p distributions for (a) positive and (b) negative tracks with $0.8 < p/\text{GeV} < 1.2$ and $ \eta < 0.6$, in simulation with the FTFP_BERT and QGSP_BERT physics lists.	87
315			
316			
317			
318	Figure 52	Comparison of the response of the hadronic calorimeter as a function of track momentum (a) at the EM-scale and (b) after the LCW calibration.	87
319			
320			
321	Figure 53	Comparison of the response of the EM calorimeter as a function of track momentum (a) at the EM-scale and (b) with the LCW calibration.	88
322			
323			
324	Figure 54	The reconstructed mass peaks of (a) K_S^0 , (b) Λ , and (c) $\bar{\Lambda}$ candidates.	89
325			
326	Figure 55	The E/p distribution for isolated (a) π^+ , (b) π^- , (c) proton, and (d) anti-proton tracks.	90
327			
328	Figure 56	The fraction of tracks with $E \leq 0$ for identified (a) π^+ and π^- , and (b) proton and anti-proton tracks	90
329			

330	Figure 57	The difference in $\langle E/p \rangle$ between (a) π^+ and π^- (b) p and π^+ , and (c) \bar{p} and π^-	91
331		$\langle E/p \rangle_{\text{COR}}$ as a function of track momentum for (a) π^+ tracks and (b) π^- tracks.	92
332	Figure 58		
333		The ratio of the calorimeter response to single particles of various species to the calorimeter response to π^+ with the physics list FTFP_BERT.	92
334	Figure 59		
335		The spectra of true particles inside anti- k_t , $R = 0.4$ jets with (a) $90 < p_T/\text{GeV} < 100$, (b) $400 < p_T/\text{GeV} < 500$, and (c) $1800 < p_T/\text{GeV} < 2300$	96
336			
337	Figure 60	The JES uncertainty contributions, as well as the total JES uncertainty, as a function of jet p_T for (a) $ \eta < 0.6$ and (b) $0.6 < \eta < 1.1$	98
338			
339		The JES correlations as a function of jet p_T and $ \eta $ for jets in the central region of the detector.	99
340	Figure 61		
341		A schematic diagram of an R-Hadron event with a lifetime around 0.01 ns. The diagram includes one charged R-Hadron (solid blue), one neutral R-Hadron (dashed blue), Lightest Supersymmetric Particles (LSPs) (dashed green) and charged hadrons (solid orange). The pixel detector, calorimeters, and muon system are illustrated but not to scale.	105
342			
343	Figure 62		
344			
345	Figure 63		
346			
347			
348			
349			
350			
351			
352	Figure 64		
353			
354			
355			
356			
357			
358	Figure 65		
359			
360			
361			
362			
363			
364	Figure 66		
365			
366			
367			
368			
369			
370	Figure 67		
371			
372			
373			
374			

375	Figure 68	The distribution of (a) E_T^{miss} and (b) Calorimeter E_T^{miss} for simulated signal events before the trigger requirement.	112
376			
377			
378	Figure 69	The distribution of E_T^{miss} for data and simulated signal events, after the trigger requirement.	114
379			
380	Figure 70	The trigger efficiency for the HLT_xe70 trigger requirement as a function of (a) E_T^{miss} and (b) Calorimeter E_T^{miss} for simulated signal events.	115
381			
382			
383	Figure 71	The dependence of dE/dx on N_{split} in data after basic track hit requirements have been applied.	116
384			
385	Figure 72	The distribution of dE/dx with various selections applied in data and simulated signal events.	116
386			
387	Figure 73	The distribution of track momentum for data and simulated signal events, after previous selection requirements have been applied.	117
388			
389			
390	Figure 74	The distribution of M_T for data and simulated signal events, after previous selection requirements have been applied.	118
391			
392			
393	Figure 75	The distribution of summed tracked momentum within a cone of $\Delta R < 0.25$ around the candidate track for data and simulated signal events, after previous selection requirements have been applied.	119
394			
395			
396			
397	Figure 76	The normalized, two-dimensional distribution of E/p and f_{EM} for simulated (a) $Z \rightarrow ee$, (b) $Z \rightarrow \tau\tau$, (c) 1200 GeV Stable R-Hadron events, and (d) 1200 GeV, 10 ns R-Hadron events.	120
398			
399			
400			
401	Figure 77	Two-dimensional distribution of dE/dx versus charge signed momentum (qp) for minimum-bias tracks. The fitted distributions of the most probable values for pions, kaons and protons are superimposed.	121
402			
403			
404			
405	Figure 78	The distribution of mass estimated using dE/dx for simulated stable R-Hadrons with masses between 1000 and 1600 GeV.	122
406			
407			
408	Figure 79	The acceptance \times efficiency as a function of R-Hadron (a) mass and (b) lifetime. (a) shows all of the combinations of mass and lifetime considered in this search, and (b) highlights the lifetime dependence for 1000 GeV and 1600 GeV R-Hadrons.	124
409			
410			
411			
412			
413	Figure 80	The distribution of (a) dE/dx and (b) momentum for tracks in data and simulated signal after requiring the event level selection and the track selection on p_T , hits, and N_{split} . Each sub-figure shows the normalized distributions for tracks classified as hadrons, electrons, and muons in data and R-Hadrons in the simulated signal.	126
414			
415			
416			
417			
418			
419			

420	Figure 81	The distribution of $M_{dE/dx}$ (a) before and (b) after the ionization requirement for tracks in simulated W boson decays and for the randomly generated background estimate.	128
421			
422			
423			
424	Figure 82	The distribution of $M_{dE/dx}$ (a) before and (b) after the ionization requirement for tracks in the validation region and for the randomly generated background estimate.	129
425			
426			
427			
428	Figure 83	The trigger efficiency for the HLT_xe70 trigger requirement as a function of Calorimeter E_T^{miss} for simulated data events with a W boson selection. Simulated signal events and simulated W boson events are also included.	134
429			
430			
431			
432			
433	Figure 84	The efficiency of the muon veto for R-hadrons of two different masses, as a function of $\frac{1}{\beta}$ for simulated R-Hadron tracks.	136
434			
435			
436	Figure 85	The average reconstructed MDT β distribution for $Z \rightarrow \mu\mu$ events in which one of the muons is reconstructed as a slow muon, for both data and simulation. A gaussian fit is superimposed.	137
437			
438			
439			
440	Figure 86	The observed mass distribution of events in data and the generated background distribution in (a) the stable and (b) the metastable signal region. A few example simulated signal distributions are superimposed.	138
441			
442			
443			
444	Figure 87	The observed and expected cross section limits as a function of mass for the stable simulated signal. The predicted cross section values for the corresponding signals are included.	141
445			
446			
447			
448	Figure 88	The observed and expected cross section limits as a function of mass for each generated lifetime. The predicted cross section values for the corresponding signals are included.	142
449			
450			
451			
452	Figure 89	The excluded range of masses as a function of gluino lifetime. The expected lower limit (LL), with its experimental $\pm 1\sigma$ band, is given with respect to the nominal theoretical cross-section. The observed 95% LL obtained at $\sqrt{s} = 8$ TeV [71] is also shown for comparison.	144
453			
454			
455			
456			
457	Figure 90	The constraints on the gluino mass as a function of lifetime for a split-supersymmetry model with the gluino R-Hadrons decaying into a gluon or light quarks and a neutralino with mass of 100 GeV. The solid lines indicate the observed limits, while the dashed lines indicate the expected limits. The area below the curves is excluded. The dots represent results for which the particle is assumed to be prompt or stable.	145
458			
459			
460			
461			
462			
463			
464			

465 LIST OF TABLES

466 Table 1	The particles in the SM and their corresponding super-
467	partners in the Minimal Supersymmetric Model (MSSM). 22
468 Table 2	The design parameters of the LHC beam that deter-
469	mines the energy of collisions and the luminosity, for
470	both the injection of protons and at the nominal cir-
471	culation. 34
472 Table 3	The performance goals for each of the subsystems of
473	the ATLAS detector. The $ \eta $ coverage specifies the range
474	where the subsystem needs to be able to provide mea-
475	surements with the specified resolution. The resolu-
476	tions include a p_T or E dependence that is added in
477	quadrature with a p_T/E independent piece. 39
478 Table 4	A summary of the parameters of each of the three mag-
479	net systems on ATLAS 41
480 Table 5	A summary of the parameters of the inner detector
481	and each of the subdetectors [6]. 46
482 Table 6	A summary of the expected performance of the com-
483	bined inner detector [11]. Included are the reconstruc-
484	tion efficiencies for multiple particle types as well as the
485	momentum and impact parameter (IP) resolution for
486	various momenta. 47
487 Table 7	The trigger menu for the 2015 data collection with
488	$L = 5 \times 10^{33} \text{ cm}^{-2} \text{ s}^{-1}$. Both the L1 and high level trig-
489	ger (HLT) selection requirements and their trigger rates
490	are shown measured at the specified luminosity are
491	shown. The typical offline selections represent a typi-
492	cal set of offline requirements imposed after the trig-
493	ger in an analysis. 61
494 Table 8	The dominant sources of corrections and systematic
495	uncertainties in the JES estimation technique, includ-
496	ing typical values for the correcting shift (Δ) and the
497	associated uncertainty (σ). 97
498 Table 9	The expected number of events at each level of the se-
499	lection for metastable 1600 GeV, 10 ns R-Hadrons,
500	along with the number of events observed in data, for
501	3.2 fb^{-1} . The simulated yields are shown with statis-
502	tical uncertainties only. The total efficiency \times accep-
503	tance is also shown for the signal. 123

504	Table 10	A summary of the sources of systematic uncertainty for the data-driven background in the signal region. If the uncertainty depends on the mass, the maximum values are reported.	131
505			
506			
507			
508	Table 11	A summary of the sources of systematic uncertainty for the simulated signal yield. The uncertainty depends on the mass and lifetime, and the maximum negative and positive values are reported in the table.	133
509			
510			
511			
512	Table 12	Example of the contributing systematic variations to the total systematic for the E_T^{miss} Scale, as measured in a 1200 GeV, Stable R-Hadron signal sample.	135
513			
514			
515	Table 13	The estimated number of background events and the number of observed events in data for the specified selection regions prior to the requirement on mass. The background estimates show statistical and systematic uncertainties.	138
516			
517			
518			
519			
520	Table 14	The left and right extremum of the mass window for each generated mass point with a 10 ns lifetime.	139
521			
522	Table 15	The left and right extremum of the mass window used for each generated stable mass point.	139
523			
524	Table 16	The expected number of signal events, the expected number of background events, and the observed number of events in data with their respective statistical errors within the respective mass window for each generated stable mass point	140
525			
526			
527			
528			
529	Table 17	The expected number of signal events, the expected number of background events, and the observed number of events in data with their respective statistical errors within the respective mass window for each generated mass point with a lifetime of 10 ns.	140
530			
531			
532			
533			
534	Table 18	The observed and expected 95% CL lower limit on mass for gluino R-Hadrons for each considered lifetime.	143
535			
536	Table 19	The left and right extremum of the mass window for each generated mass point with a 50 ns lifetime.	155
537			
538	Table 20	The left and right extremum of the mass window for each generated mass point with a 30 ns lifetime.	155
539			
540	Table 21	The left and right extremum of the mass window for each generated mass point with a 10 ns lifetime.	156
541			
542	Table 22	The left and right extremum of the mass window used for each generated mass point with a lifetime of 3 ns.	156
543			
544	Table 23	The left and right extremum of the mass window used for each mass point with a lifetime of 1 ns.	156
545			
546	Table 24	The left and right extremum of the mass window for each generated mass point with a lifetime of 0.4 ns.	157
547			
548	Table 25	The left and right extremum of the mass window used for each generated stable mass point.	157
549			

550	Table 26	The expected number of signal events, the expected number of background events, and the observed number of events in data with their respective statistical errors within the respective mass window for each generated mass point with a lifetime of 50 ns.	157
551			
552			
553			
554			
555	Table 27	The expected number of signal events, the expected number of background events, and the observed number of events in data with their respective statistical errors within the respective mass window for each generated mass point with a lifetime of 30 ns.	158
556			
557			
558			
559			
560	Table 28	The expected number of signal events, the expected number of background events, and the observed number of events in data with their respective statistical errors within the respective mass window for each generated mass point with a lifetime of 10 ns.	158
561			
562			
563			
564			
565	Table 29	The expected number of signal events, the expected number of background events, and the observed number of events in data with their respective statistical errors within the respective mass window for each generated mass point with a lifetime of 3 ns.	159
566			
567			
568			
569			
570	Table 30	The expected number of signal events, the expected number of background events, and the observed number of events in data with their respective statistical errors within the respective mass window for each generated mass point with a lifetime of 1 ns.	159
571			
572			
573			
574			
575	Table 31	The expected number of signal events, the expected number of background events, and the observed number of events in data with their respective statistical errors within the respective mass window for each generated mass point with a lifetime of p4 ns.	160
576			
577			
578			
579			
580	Table 32	The expected number of signal events, the expected number of background events, and the observed number of events in data with their respective statistical errors within the respective mass window for each generated stable mass point	160
581			
582			
583			
584			

586 ACRONYMS

- 587 SM Standard Model
588 CERN European Organization for Nuclear Research
589 SUSY Supersymmetry
590 LSP Lightest Supersymmetric Particle
591 LHC Large Hadron Collider
592 ATLAS A Toroidal LHC ApparatuS
593 CMS Compact Muon Solenoid
594 ALICE A Large Ion Collider Experiment
595 LHCb Large Hadron Collider beauty experiment
596 LEP the Large Electron Positron collider
597 PS Proton Synchrotron
598 PSB Proton Synchrotron Booster
599 SPS Super Proton Synchrotron
600 SCT silicon microstrip
601 TRT transition radiation tracker
602 LAr Liquid Argon
603 EM electromagnetic
604 RPC Resistive Plate Chamber
605 TGC Thin Gap Chamber
606 MDT Monitored Drift Tube
607 CSC Cathode Strip Chamber
608 ToT time over threshold
609 RoI Region of Interest
610 LCW local cluster weighted
611 MIP minimally ionizing particle
612 IP impact parameter

- 613 EPJC European Physical Journal C
614 JES jet energy scale
615 LLP Long-Lived Particle
616 CR Control Region
617 NLO next-to-leading order
618 NLL next-to-leading logarithmic
619 PDF parton distribution function
620 ISR initial state radiation
621 RMS root mean square
622 IBL Insertible B-Layer
623 CP Combined Performance
624 MDT Monitored Drift Tube
625 RF radiofrequency
626 HLT high level trigger
627 QCD quantum chromodynamics
628 BSM beyond the Standard Model
629 MSSM Minimal Supersymmetric Model

630

PART I

631

INTRODUCTION

632

You can put some informational part preamble text here.

1

633

634 INTRODUCTION

635

PART II

636

THEORETICAL CONTEXT

637

You can put some informational part preamble text here.

2

638

639 STANDARD MODEL

640 The SM of particle physics seeks to explain the symmetries and interactions of
641 fundamental particles. The SM provides predictions in particle physics for in-
642 teractions up to the Planck scale (10^{15} - 10^{19} GeV). It has been tested by several
643 generations of experiments and has been remarkably successful; no significant
644 deviations from its predictions have been found.

645 The theory itself is a quantum field theory grown from an underlying sym-
646 metry, $SU(3) \times SU(2) \times U(1)$, that generates all of the interactions consistent
647 with experimental observations. These interactions are referred to as the Strong,
648 Weak, and Electromagnetic forces. Each postulated symmetry necessitates the
649 existence of an associated conserved charge, which appear as properties of the
650 observed particles in nature.

651 Although this model has been very predictive, the theory is incomplete; for
652 example, it is not able to describe gravity or astronomically observed dark mat-
653 ter. These limitations suggest a need for an extension or new theory to describe
654 physics at higher energies.

655 2.1 ACTION AND THE LAGRANGIAN

Originally, both action and the Lagrangian were constructed for an integral reformulation of the laws of classical mechanics, which is a purely mathematical step: any differential equation can be re-expressed in terms of an integral equation. The Lagrangian, \mathcal{L} , is classically given by the difference of kinetic energy and potential energy. The Lagrangian is defined this way so that the action, \mathcal{S} , given by

$$\mathcal{S}[\mathbf{q}(t)] = \int_{t_1}^{t_2} \mathcal{L}(\mathbf{q}, \dot{\mathbf{q}}, t) dt \quad (1)$$

656 returns the classical equations of motion when one requires it to be stationary
657 in the path, $\mathbf{q}(t)$. This formulation of classical mechanics is extremely useful in
658 calculations, and generalizes beautifully to cover all types of physics.

659 In particular, with the development of quantum mechanics in the twentieth
660 century, the concepts of action and the Lagrangian were found to generalize to
661 more complicated physics for which the classical laws do not hold. Quantum
662 mechanics and quantum field theory can be constructed from the action, using
663 the path integral formulation, by assuming that a particle undergoes all possible
664 paths $\mathbf{q}(t)$ with an imaginary phase given by $e^{i\mathcal{S}[\mathbf{q}(t)]/\hbar}$. This reduces to classical
665 mechanics in the limit as \hbar goes to zero, as all paths for which the action is not
666 stationary interfere with each other so as to cancel their contributions. Because
667 the wavefunction of a particle can be completely determined through the action

668 and the action depends only on the Lagrangian, the Lagrangian itself is sufficient
 669 to describe the physics governing the particle.

670 So, in both classical and quantum mechanics, the Lagrangian of a system con-
 671 tains everything there is to know about the system, apart from initial conditions.
 672 Thus, the most natural way to express that a system has a certain symmetry is to
 673 require that the Lagrangian is invariant under a corresponding symmetry trans-
 674 formation. This makes the Lagrangian the central piece of the discussion of
 675 gauge invariance; the mathematical representation of gauge invariance is that a
 676 gauge transformation on the appropriate components of the Lagrangian returns
 677 an identical Lagrangian. That is,

$$\mathcal{L}(\psi, D^\mu) = \mathcal{L}(U\psi, D'^\mu) \quad (2)$$

678 where ψ is the wavefunction and D^μ is the covariant derivative, both of which
 679 transform under a symmetry operation. There are a number of immediate and
 680 surprisingly powerful consequences of requiring that the Lagrangian is invariant
 681 under a symmetry operation.

682 2.2 GAUGE INVARIANCE AND FORCES

683 The simplest possible relativistic, quantum Lagrangian is the free Dirac Lagrangian,
 684 which describes a relativistic fermion in a vacuum.

$$\mathcal{L} = i\bar{\psi}\not{d}\psi - m\bar{\psi}\psi \quad (3)$$

685 A fermion denotes a particle with spin-1/2, and the kinematic term is chosen to
 686 correctly describe the free propagation of a fermionic particle with mass m . This
 687 equation is clearly invariant under a global $U(1)$ transformation, that is chang-
 688 ing ψ by a complex phase has no effect. The derivative operator commutes with
 689 a constant phase factor, and wherever ψ appears its complex conjugate also ap-
 690 pears so as to cancel out the change of phase. However, the Lagrangian as written
 691 is not invariant under the local $U(1)$ symmetry postulated for the SM, which can
 692 be written as $U = e^{ia(x)}$. The piece of the Lagrangian involving a derivative will
 693 return an extra term that will break the invariance of the Lagrangian under this
 694 transformation:

$$\begin{aligned} \mathcal{L}' &= i(\bar{\psi}U^\dagger)\not{d}(U\psi) - m(\bar{\psi}U^\dagger)(U\psi) \\ &= i(\bar{\psi}U^\dagger)U(\not{d} - \gamma^\mu\partial_\mu\alpha(x))\psi - m(\bar{\psi}U^\dagger)(U\psi) \\ &= i\bar{\psi}\not{d}\psi - m\bar{\psi}\psi - i\gamma^\mu\partial_\mu\alpha(x)\bar{\psi}\psi \\ &= \mathcal{L} - i\gamma^\mu\partial_\mu\alpha(x)\bar{\psi}\psi \\ &\neq \mathcal{L} \end{aligned}$$

695 So, in order to enforce the required symmetry, the typical approach is to con-
 696 struct a covariant derivative, that is to add a term to the derivative operator

so that the unwanted term in \mathcal{L}' is exactly canceled. A generic form for such a derivative is given by

$$D^\mu = \partial^\mu - iqA^\mu$$

where at this point A^μ is an arbitrary field that transforms under the $U(1)$ operator and q is a scaling factor. Adding this component to the above Lagrangian gives

$$\mathcal{L}' = i(\bar{\psi}U^\dagger)U(\not{d} - \gamma^\mu\partial_\mu\alpha(x) - iq\gamma^\mu A'_\mu)\psi - m(\bar{\psi}U^\dagger)(U\psi) \quad (4)$$

$$\mathcal{L}' = \mathcal{L} + \gamma^\mu(-i\partial_\mu\alpha(x) - iqA'_\mu + iqA_\mu)\bar{\psi}\psi \quad (5)$$

and because the transformation of A^μ is unspecified, $\mathcal{L} = \mathcal{L}'$ whenever

$$A'_\mu = A_\mu - \frac{1}{q}\partial_\mu\alpha(x)$$

The above procedure demonstrated that beginning with the Lagrangian for a free fermion and imposing a local $U(1)$ symmetry required the existence of a vector field A^μ , and specified its transformation under the $U(1)$ gauge group. The additional term in the derivative can be expanded to form a completely separate term in the Lagrangian,

$$\mathcal{L} = i\bar{\psi}\not{d}\psi - m\bar{\psi}\psi - (q\bar{\psi}\gamma^\mu\psi)A^\mu \quad (6)$$

and in this form it is clear that the A^μ term has the exact form of the electromagnetic interaction. That is, this is the Lagrangian which reproduces the relativistic form of Maxwell's equations for a particle interacting with an electromagnetic field. It is natural to also introduce a term to the Lagrangian at this point to describe the free propagation of the vector A field, where the propagation of a vector field has the form of

$$-\frac{1}{16\pi}F^{\mu\nu}F_{\mu\nu} \quad \text{with} \quad F_{\mu\nu} = \partial_\mu A_\nu - \partial_\nu A_\mu \quad (7)$$

This then also describes the electromagnetic interactions in a vacuum and the propagation of a photon. The photon is an example of a gauge boson, a spin-0 particle required to exist by a gauge symmetry of the Lagrangian and one that corresponds to a force. In summary, requiring the $U(1)$ symmetry was enough to recover all of electromagnetism and to predict the existence of a photon in the SM.

The interaction term that was placed into the Lagrangian by this procedure can be conveniently summarized with Feynman diagrams, which diagrammatically represent a transition from an initial state to a final state. All diagrams that start with the same initial state and end with the same final state must be considered, but more complicated diagrams can be built by linking together the simplest versions. A diagram that corresponds to the above term, $(q\bar{\psi}\gamma^\mu\psi)A^\mu$, is shown in Figure 1, for an interaction with a generic fermion.

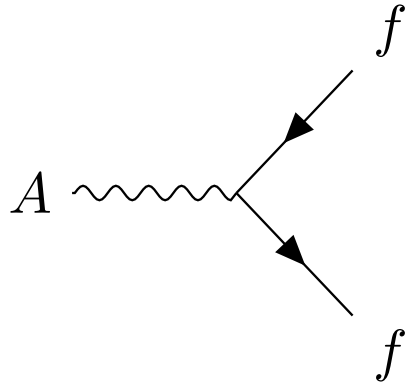


Figure 1: A Feynman diagram representing the interaction of the A field with a generic fermion, f .

727 2.2.1 $SU(2) \times U(1)$ AND THE ELECTROWEAK FORCE

728 The full picture of the electroweak section of the SM is more complicated than the
729 simplified explanation of the electromagnetic piece described above. In practice,
730 it is necessary to consider the entire $SU(2) \times U(1)$ symmetry together, but the
731 procedure is the same. Enforcing the symmetry on the Lagrangian requires the
732 introduction of a covariant derivative, this time with four total distinct terms,
733 one for each of the generators of $SU(2) \times U(1)$. The result is a series of terms
734 in the Lagrangian which describe the interaction of a fermion with four vector
735 fields, the W_1 , W_2 , W_3 , and B fields. These fields can mix in the quantum sense,
736 and linear combinations form the W^+ , W^- , Z , and A fields that are considered
737 actual particles in the SM¹.

738 2.2.2 $SU(3)$ AND THE STRONG FORCE

739 The same procedure can be applied starting with the $SU(3)$ symmetry require-
740 ment, where eight additional fields must be introduced, one for each of the gen-
741 erators of $SU(3)$. The resulting Lagrangian describes quantum chromodynam-
742 ics (QCD) and predicts the existence of eight gauge bosons known collectively as
743 gluons.

744 2.3 NOETHER'S THEOREM, CHARGES, AND MATTER

745 Another direct consequence of the symmetries stipulated in the SM are a series
746 of conserved quantities, Noether charges, named after the mathematician and
747 physicist Emmy Noether. The charges arise as a direct consequence of Noether's
748 theorem, which can be informally stated as

1 These states are the actual particles because they are mass eigenstates, but the full explanation of this will have to wait for the discussion of the Higgs mechanism.

749 *For every symmetry of the Lagrangian, there exists a corresponding phys-*
 750 *ical quantity whose value is conserved in time.*

751 Or, stated another way, symmetries of the Lagrangian mathematically require
 752 the conservation of specific quantities taken from the Lagrangian. This rela-
 753 tionship can also be thought of as operating in the other direction, the exis-
 754 tence of a conserved charge can be shown to generate the symmetry in the La-
 755 grangian. This theorem is actually quite striking in a somewhat unexpected re-
 756 lation between simple geometric symmetries and physically observable conser-
 757 vation laws. For example, the theorem connects the translation invariance of
 758 the Lagrangian in space to the conservation of momentum and the translation
 759 invariance in time to the conservation of energy.

760 In the context of the SM, the required symmetries of $U(1) \times SU(2) \times SU(3)$
 761 correspond to the charges that are considered properties of all elementary par-
 762 ticles. The most familiar of these properties is the electric charge, Q , which is
 763 one of the conserved quantities of $SU(2) \times U(1)$. The remaining pieces of
 764 $SU(2) \times U(1)$ correspond to weak isospin, T and T_3 , where T has only non-
 765 negative values and T_3 can be positive and negative. The $SU(3)$ symmetry is
 766 generated by the three colors of QCD, red, green, and blue, each with a corre-
 767 sponding opposite color, anti-red, anti-green, and anti-blue.

768 The matter in the observable universe consists of a collection of particles which
 769 carry these charges, in addition to spin and mass. The particles typically thought
 770 of as matter are all fermions: particles with spin-1/2. All of the fermions belong
 771 to one of two groups, quarks and leptons, and one of three generations. Each
 772 of the generations have similar properties but significantly different masses; the
 773 particles in consecutive generations have increasing mass. Quarks are distin-
 774 guished from leptons in that they carry color charge, in addition to electric charge
 775 and weak isospin. The particles in the SM are summarized in Figure 2, and the
 776 matter particles are the twelve types of fermions displayed on the left side of the
 777 graphic.

778 2.3.1 QUARKS

779 The three generations of quarks each have a particle with electric charge +2/3
 780 and one with charge -1/3. They are referred to us up and down, charm and
 781 strange, and top and bottom respectively, and these are referred to as the quark
 782 flavors. Although Figure 2 only shows these six flavors, there is a unique particle
 783 for each combination of the three colors and flavor. And each quark has an anti-
 784 particle with the opposite electric and color charge values.

785 However, individual quarks are never observed in nature, but instead form
 786 color-neutral bound states. One way to form a color neutral combination is a
 787 bound state of three quarks with three different color charges, called a baryon.
 788 Baryons are the most common type of quark configuration in conventional mat-
 789 ter, and include protons and neutrons. The other common configuration is a
 790 bound state of a quark and an anti-quark, called a meson, where the two quarks
 791 have the same type but opposite colors. The conservation of the various charges
 792 carried by quarks, along with the requirement that quarks appear in color-neutral

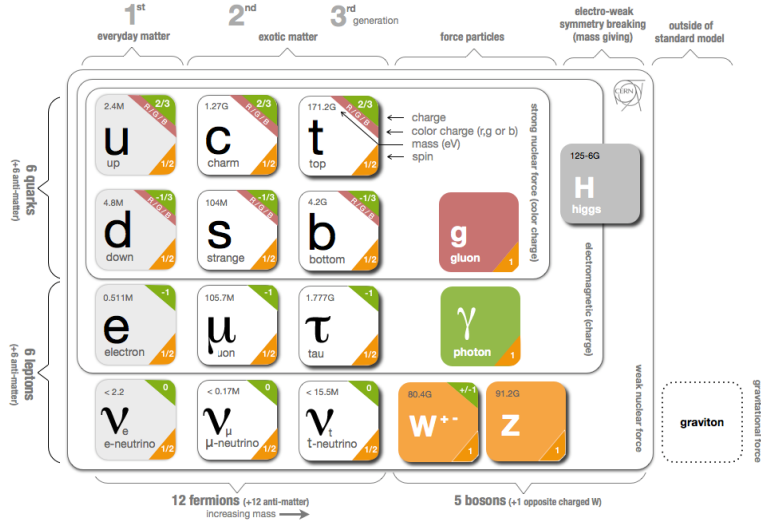


Figure 2: The particle content of the SM.

793 states, result in the observed conservation of baryon number, B , where baryons
 794 have $B = 1$ and mesons have $B = 0$.

795 2.3.2 LEPTONS

796 The remaining fermions, the leptons, do not carry color charge. Each generation
 797 contains an electrically charged lepton, the electron, muon, and tau, and an elec-
 798 trically neutral lepton called a neutrino. For the charged leptons, the flavors are
 799 mass eigenstates, with the masses listed in Figure 2. The flavors of the neutrinos,
 800 on the other hand, are not mass eigenstates: they propagate in mass eigenstates
 801 and so can oscillate between different flavors. The absolute masses of the neu-
 802 trinos are not currently known, but the phenomenon of oscillations shows that
 803 they have three different mass values. Although there is no direct conservation
 804 law resulting from the symmetries of the SM Lagrangian, no interactions have
 805 been observed which alter lepton number, L , the difference in the number of lep-
 806 tons and anti-leptons.

807 2.3.3 CHIRALITY

808 All of the fermions described above have two possible values of the magnitude
 809 of weak isospin, T , either 0 or 1/2. The fermions with $T = 0$ are called right-
 810 handed, while those with $T = 1/2$ are called left-handed. For left-handed fermions,
 811 each of the quark and lepton generations have one particle with $T_3 = -1/2$ and
 812 one with $T_3 = +1/2$. The neutrinos have $T_3 = +1/2$, while the charged leptons
 813 have $T_3 = -1/2$. Similarly, the positively charged quarks have $T_3 = +1/2$ and the
 814 negatively charged quarks have $T_3 = -1/2$. Because the right-handed neutrinos
 815 would have no charge of any type, it is not clear if they exist at all.

816 2.4 HIGGS MECHANISM AND MASS

817 The description of the electroweak forces above left out an important part of the
 818 observed nature of the electroweak force. Many physical experiments observed
 819 phenomena corresponding to the interaction of the weak bosons that were best
 820 explained if they had significant masses. A large mass for the W and Z bosons
 821 would explain the relative weakness of their interactions compared to the elec-
 822 tromagnetic field. The Lagrangian's discussed above did not include a mass term
 823 for the gauge bosons, and in fact such a term would not be allowed by the require-
 824 ment of gauge invariance. This was a significant problem for the SM, and the
 825 symmetry of the electroweak sector would have to be broken in order to allow
 826 for non zero masses for some of the gauge bosons.

827 One mechanism to allow for this spontaneous symmetry breaking is the Higgs
 828 mechanism, which posits the existence of an additional scalar field. It begins
 829 with a $SU(2) \times U(1)$ invariant Lagrangian of the form

$$\mathcal{L} = |D_\mu \phi|^2 - \frac{1}{2}\mu^2\phi^+\phi - \frac{1}{4}\lambda(\phi^+\phi)^2 \quad (8)$$

830 where ϕ is the new scalar field and, importantly, μ^2 is negative. This leads to a
 831 minimum value of the field at a non-zero value of ϕ , specifically where

$$\langle \phi \rangle = \frac{1}{\sqrt{2}} \begin{pmatrix} 0 \\ v \end{pmatrix} \quad \text{with} \quad v = \frac{2\mu^2}{\lambda} \quad (9)$$

832 Expanding the original Lagrangian about its expectation value,

$$\langle \phi \rangle = \frac{1}{\sqrt{2}} \begin{pmatrix} 0 \\ v + H \end{pmatrix} \quad (10)$$

833 gives potential terms in the Lagrangian like

$$\mathcal{L}_H = -\frac{1}{2}m_H^2H^2 - \sqrt{\frac{\lambda}{2}}m_HH^3 - \frac{1}{4}\lambda H^4 \quad (11)$$

834 where $m_H = \sqrt{2}\mu$. The form of this Lagrangian shows that the non-zero ex-
 835 pectation value of the ϕ field has introduced a massive scalar field H with self
 836 interaction terms. It has an additional important consequence on the description
 837 of the gauge bosons, through the expansion of the term involving the covariant
 838 derivative:

$$|D_\mu \phi|^2 \supset \frac{1}{8} (g^2(W_{1\mu}W_1^\mu + W_{2\mu}W_2^\mu) + (g'B_\mu - gW_3\mu)^2) \quad (12)$$

839 where the W_i and B fields are the original $SU(2) \times U(1)$ gauge fields men-
 840 tioned previously. The above equation can be rearranged using linear combina-
 841 tions of the fields to from mass terms for the gauge bosons, and the mass eigen-
 842 states are exactly the W^\pm , Z , and A fields. Only the A field, corresponding to

843 the photon, results in a zero mass, and the remaining three fields acquire masses.
 844 Because the originally introduced Lagrangian, written in terms of ϕ , was clearly
 845 gauge invariant, this resulting configuration must also be gauge invariant.

846 This is the Higgs mechanism, where the introduction of a gauge invariant
 847 scalar field with a non-zero expectation value can generate masses for the gauge
 848 bosons without violating the underlying symmetries. The particle that is asso-
 849 ciated with the perturbations of this field, H , is called the Higgs boson, and is
 850 said to generate the masses of the remaining bosons. The resulting masses are
 851 listed in Figure 2. Because this mechanism was so successful in describing the
 852 observed properties of the W and Z bosons, it has been considered part of the
 853 SM for decades, although the actual Higgs boson was only recently observed in
 854 2012, confirming the theory.

855 The Higgs mechanism is also responsible for generating the masses of the
 856 fermions. The original mass terms that were listed in the Lagrangian for fermions
 857 are replaced with Yukawa coupling terms, which introduce interactions between
 858 the ϕ field and the fermions. Like with the gauge bosons, the non-zero expec-
 859 tation value of the field yields mass terms, and the expansion about that value
 860 introduces interaction terms between the fermions and the Higgs boson. The
 861 masses are different between each fermion because each has a different Yukawa
 862 coupling, which results in the masses listed in Figure 2.

863 2.5 PHENOMENOLOGY

864 The SM Lagrangian described above contains all of the information necessary
 865 to describe particle physics through the path integral formulation. However, a
 866 tremendous amount of complexity emerges from that description because of the
 867 diverse allowed interactions between the ensemble of particles in the SM. A qual-
 868 itative understanding of the phenomenology produced by those interactions is
 869 immensely helpful in understanding the analysis of particle physics.

870 2.5.1 ELECTROWEAK PHYSICS

871 The masses of the W and Z bosons result in significantly different processes
 872 for the weak fields than the electromagnetic field, despite their interactions be-
 873 ing similar before symmetry breaking. The massless photon is stable, and can
 874 propagate in a vacuum, resulting in the familiar long range interactions of elec-
 875 tromagnetism. The W and Z bosons, however, are unstable, as they have large
 876 enough masses to decay to fermions, such as the decays shown in Figure 3. For
 877 this reason, photons can be observed directly, while the other bosons are suffi-
 878 ciently short-lived that they can only be measured from their decay products.

879 Because the W and Z bosons interact with both quarks and leptons, they are
 880 responsible for the production of leptons in proton-proton collisions. Z bosons
 881 produce pairs of opposite sign, same flavor leptons. W bosons, on the other hand,
 882 produce a single lepton and the corresponding neutrino.

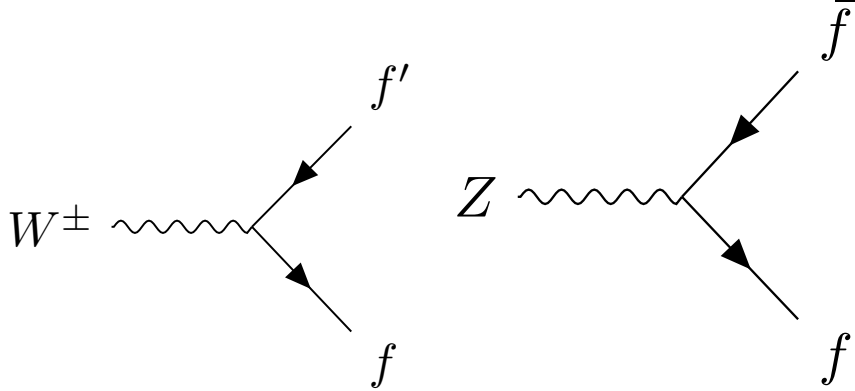


Figure 3: The Feynman diagrams representing the decays of the W and Z bosons to fermions. Here f indicates a generic fermion, \bar{f} its antiparticle, and f' the partner of that fermion in the same generation.

883 2.5.2 STRONG PHYSICS

884 The phenomenology of the strong sector differs significantly from the weak sec-
 885 tor because the gluons are massless but color charged. Because of this, gluons
 886 can interact with each other, and contributions from multiple gluon interactions
 887 lead to a significant growth in the strength of the field at low energies. The depen-
 888 dence of the field strength on the energy scale is described by renormalization,
 889 and in QCD the coupling is only small at high energies. Above around the GeV
 890 scale, the interactions of quarks become perturbative, similar to the electroweak
 891 fields; this phenomenon is known as asymptotic freedom.

892 At lower energies, however, the strength of the strong interaction is so signif-
 893 icant that the interactions of color-charged particles create additional particles
 894 until they form neutral bound-states. This process is known as hadronization,
 895 and explains why no quarks are observed isolated in nature: they all form bound
 896 states of hadrons like protons, neutrons, and pions. The hadronization process
 897 can produce a significant number of particles, so that a single energetic quark
 898 recoiling against another quark can generate a cascade of dozens of hadrons.
 899 Because of the initial boost of such an energetic configuration, the resulting
 900 hadrons are collimated, and conical spray of particles often referred to as a jet.

901 2.5.3 PROTON-PROTON COLLISIONS

902 Proton-proton collisions are a convenient way to generate high energy interac-
 903 tions to probe the SM and to search for new physics. At the energies that will be
 904 discussed in this analysis, the substructure of the protons is very important to the
 905 description of the resulting interactions. At lowest order, protons are composed
 906 of two up quarks and one down quark, but this description is incomplete. The
 907 actual bound state includes a chaotic sea of additional quarks and gluons, each of
 908 which carries a variable fraction of the proton's energy. When a proton-proton

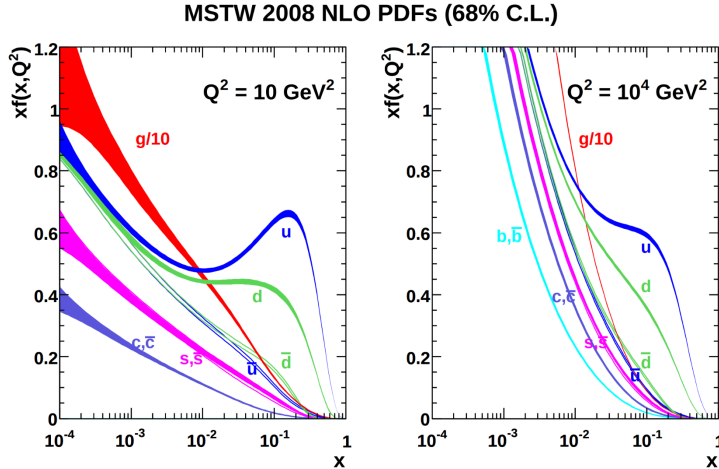


Figure 4: The PDFs for proton-proton collisions at $Q^2 = 10 \text{ GeV}^2$ and $Q^2 = 10^4 \text{ GeV}^2$. Each shows the fraction of particles which carry a fraction x of the total proton energy at the specified scale [1].

909 collision takes place, it is these constituents that interact with each other, resulting
 910 in a highly variable collision energy even when the proton-proton energy is
 911 consistent.

912 The fraction of the energy carried by each constituent varies moment to moment,
 913 but can be modelled probabilistically by PDFs. These are difficult to predict
 914 theoretically, as the QCD calculations are extremely complex, and instead
 915 are measured in hard-scattering experiments. They are usually represented by
 916 how often a given type of particle carries a fraction x of the total proton energy.
 917 Those fraction change significantly with the scale of the interaction; the PDFs of
 918 proton-proton collisions at both $Q^2 = 10 \text{ GeV}^2$ and $Q^2 = 10^4 \text{ GeV}^2$ are shown
 919 in Figure 4.

920 26 LIMITATIONS

921 Despite the great success of the relatively simple SM in describing such a broad
 922 range of emergent phenomena, it is clear that the picture it presents of the interactions
 923 of fundamental particles is incomplete. The SM contains concerning
 924 coincidences that suggest a more ordered underlying substructure that is not ex-
 925 pressed in the current form. It also fails to explain a number of cosmological
 926 measurements of the nature of matter in the universe. These limitations suggest
 927 the need for new, beyond the Standard Model (BSM) physics that would provide
 928 a more complete description at higher energies.

929 2.6.1 THEORETICAL CONCERNS

930 There have been no successful integrations of the SM's description of the elec-
 931 troweak and strong forces with the description of gravity, and it is still unclear
 932 how to account for the effects of gravity at the Plank scale of approximately 10^{19}

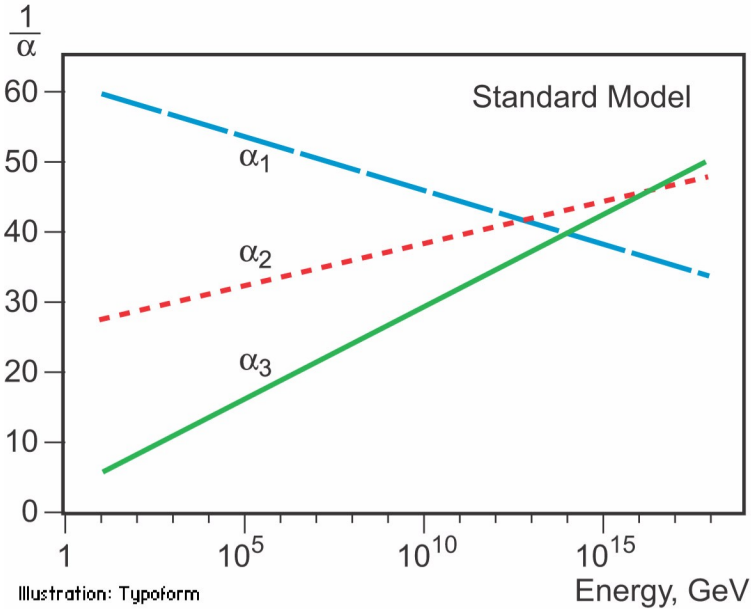


Figure 5: An approximation of the running of the coupling constants in the SM up to the Planck scale [unification_plot].

933 GeV, where it can no longer be ignored. The Plank scale is an important cutoff
 934 for the SM, as it is clear that the SM must break down somewhere between the
 935 current highest energy tests of the SM, around 1 TeV, and the Plank scale.

936 One example of this is the Higgs mass, which is determined in the SM by a
 937 sum of its bare mass and the interactions in the vacuum with all massive parti-
 938 cles. As their must be new physics at the Plank scale to describe gravity, some
 939 of those corrections would include contributions at a scale seventeen orders of
 940 magnitude above the mass of the Higgs. Either the bare mass of the Higgs boson
 941 precisely cancels those contributions to leave a remainder seventeen orders of
 942 magnitudes smaller, or a new theory exists at a lower scale the shields the Higgs
 943 mass from those terms. A theory where such a unlikely cancellation of free pa-
 944 rameters occurs is called fine-tuned, and one that is free from such cancellations
 945 is called natural. Theories where the mass of the Higgs is natural are usually
 946 preferred, as the suggest an underlying, coherent structure.

947 There is also a compelling argument that the $SU(3) \times SU(2) \times U(1)$ gauge
 948 structure of the SM might originate from a single, unified gauge theory. For ex-
 949 ample, it is possible to represent that gauge structure as a $SU(5)$ gauge group
 950 with only a few inconsistencies with the current implementation. This unifica-
 951 tion is suggested by the scaling of the coupling constants for each of the forces
 952 under renormalization, they come close to converging to a single value at higher
 953 energies, as seen in Figure 5. An additional correction to the scaling of the cou-
 954 pling constants from new physics above the TeV scale could cause them to merge
 955 into a single value at high energies.

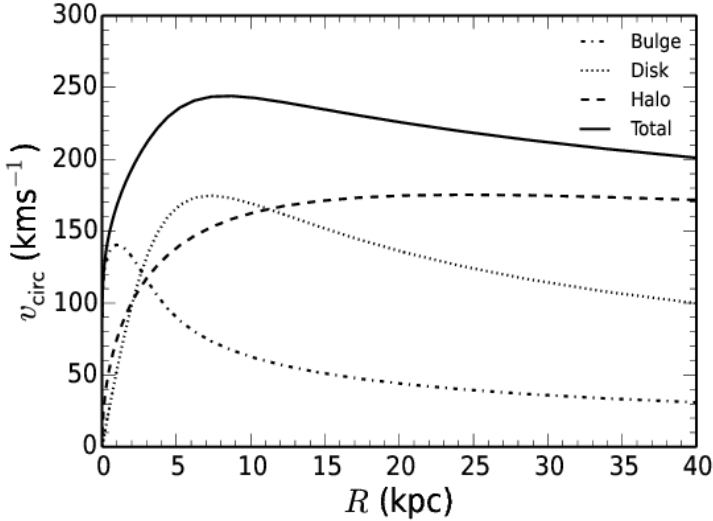


Figure 6: The distribution of velocities of stars as a function of the radius from the center of the galaxy. The contributions to the velocity from the various components of matter in the galaxy are shown [2].

956 2.6.2 COSMOLOGICAL OBSERVATIONS

957 The SM contains a symmetry in the description of matter and antimatter that is
 958 not reflected in cosmological observations. The process of the standard model
 959 create or remove matter and antimatter in equal amounts, so a universe that be-
 960 gins with an equal quantity of each should result in a universe with an approxi-
 961 mate balance of matter and antimatter. However, cosmological observations of
 962 the relative amount of each type clearly show that the directly observable mass
 963 of the universe is overwhelmingly made of matter. As this difference is largely
 964 a difference in the generation of baryons and anti-baryons, this discrepancy is
 965 often referred to as the baryogenesis problem.

966 A number of astrophysical observations of large scale gravitational interac-
 967 tions suggest the presence of a significant amount of non-luminous matter that
 968 interacts with the normal matter only gravitationally. The first evidence of this
 969 came from the observation of galactic rotation curves, the velocities of stars as
 970 a function of the radius from the center of a galaxy. These can be directly pre-
 971 dicted from the amount of matter contained within the sphere up to the radius
 972 of the star. An estimate based only on the luminous matter in the galaxies would
 973 predict a dependence that falls off with the radius, but the observed curves show
 974 a mostly constant distribution of velocities [2], as seen in Figure 6. The higher
 975 velocities than predicted by the luminous matter can be explained by a halo of
 976 dark matter that extends significantly outside the galactic disk.

977 This dark matter accounts for a majority of the matter in the universe, and is
 978 incompatible with the matter particles predicted by the SM. Many observations
 979 support its existence, but there have been no direct detections of a particle which
 980 could account for the large quantity of gravitationally interacting dark matter.
 981 The SM would have to require a significant extension to include the particles

982 needed to explain dark matter and the processes needed to explain the observed
983 matter-antimatter asymmetry.

984

985 SUPERSYMMETRY

986 The theory of Supersymmetry (**SUSY**) presents an extension to the **SM** that solves
987 a number of the outstanding issues. It is based on another proposed symmetry,
988 one which introduces an equality between the fermionic particles and proposed
989 bosonic partners. The symmetry is defined by extended spacetime into a super-
990 space, which includes on dimension that describes a particle's spin: a transfor-
991 mation in this spacetime moves a fermion with spin-1/2 to a boson with spin-0 or
992 vice-versa. Requiring the **SM** to be symmetrical under these transformations re-
993 quires the existence of a bosonic partner for every current matter fermion in the
994 **SM** and a fermionic partner for every boson. The partners are called sparticles,
995 where quarks partner with squarks and leptons partner with sleptons, and each
996 boson has a fermionic partner called a gaugino, such as the wino for the W boson.
997 The superpartners, in the original form of the theory, should be identical to the
998 original particle in every way except for spin; that is they would have the same
999 quantum charges and the same mass.

1000 However, the simplest version of the theory, where the symmetry is unbroken,
1001 is incompatible with current observations of physics in a number of systems. For
1002 example, the existence of an electron with spin-0 would introduce a stable, elec-
1003 trically charged constituent of atoms that would not follow the Pauli exclusion
1004 principle and would thus significantly change atomic structure. Various high en-
1005 ergy physics measurements have also confirmed the spin of the W and Z bosons,
1006 for example, and a fermionic gaugino has never been produced at those masses.
1007 The solution to this incompatibility with observation is to conjecture that the
1008 symmetry exists but is broken, where the masses of the supersymmetric parti-
1009 cles are significantly larger than those of the current **SM** particles.

1010 3.1 STRUCTURE AND THE MSSM

1011 There are a number of ways to model **SUSY**, but many of the resulting phenomena
1012 are similar, and a discussion of an example is sufficient to describe the structure
1013 and results of the theory. The **MSSM** is one example of a complete description
1014 that includes the necessary symmetry breaking to result in the different masses
1015 between particles and sparticles. It is called minimal because it is designed to
1016 use the simplest possible extension to the **SM** that incorporates **SUSY** and remains
1017 self-consistent. The theory includes a sparticle partner for every standard model
1018 particle, which are listed in Table 1.

1019 To then provide the different masses for those sparticles, the **MSSM** then intro-
1020 duces a second Higgs interaction. The resulting scalar field, along with the origi-
1021 nal Higgs field, generates five total particles, h^0 , the original Higgs boson, A^0 , H^0 ,
1022 and H^\pm , where the last two are electrically charged. These Higgs bosons can mix
1023 with the supersymmetric gauginos to form a series of mass eigenstates. These

Sector	Particles	Sparticles
Baryonic Matter	(u, d)	(\tilde{u}, \tilde{d})
	(c, s)	(\tilde{c}, \tilde{s})
	(t, b)	(\tilde{t}, \tilde{b})
Leptonic Matter	(ν_e, e)	$(\tilde{\nu}_e, \tilde{e})$
	(ν_μ, μ)	$(\tilde{\nu}_\mu, \tilde{\mu})$
	(ν_τ, τ)	$(\tilde{\nu}_\tau, \tilde{\tau})$
Higgs	(H_u^+, H_u^0)	$(\tilde{H}_u^+, \tilde{H}_u^0)$
	(H_d^0, H_d^-)	$(\tilde{H}_d^0, \tilde{H}_d^-)$
Strong	g	\tilde{g}
Electroweak	(W^\pm, W^0)	$(\tilde{W}^\pm, \tilde{W}^0)$
	B^0	\tilde{B}^0

Table 1: The particles in the **SM** and their corresponding superpartners in the **MSSM**.

1024 are usually referred to by the order of their masses, where the neutral gauginos
 1025 (neutralinos) are labelled $\tilde{\chi}_1^0, \tilde{\chi}_2^0, \tilde{\chi}_3^0$, and $\tilde{\chi}_4^0$. The charged gauginos (charginos)
 1026 are similarly labelled $\tilde{\chi}_1^\pm$ and $\tilde{\chi}_2^\pm$.

1027 In addition to the new particle content, the **MSSM** introduces new interactions
 1028 for the gauge bosons and gauginos. All interaction terms are added to the La-
 1029 grangian which describe the interaction of a gauge boson or gaugino with a par-
 1030 ticle or sparticle with the appropriate charge. Such terms include a few interac-
 1031 tions which would violate the observed $B - L$ symmetry that prevents proton
 1032 decay. Either the couplings on these terms must be fine-tuned to match the ex-
 1033 perimental limits on those decays, or an additional symmetry must be imposed
 1034 to exclude the terms. The **MSSM** and several other **SUSY** models choose to intro-
 1035 duce a new symmetry known as R-parity. Sparticles are R-parity odd while **SM**
 1036 particles are R-parity even. And by requiring that each term in the supersymmet-
 1037 ric Lagrangian conserves R-parity, it is enforced that sparticles are produced in
 1038 pairs.

1039 The conservation of R-parity removes the $B - L$ violating terms naturally
 1040 from the Lagrangian. The remaining terms include all of the interactions of the
 1041 **SM** where two of the particles are replaced with their **SUSY** partners, so that R-
 1042 parity is conserved in the interactions. This also has an important significance in
 1043 making the **LSP**, the $\tilde{\chi}_1^0$, stable, as it cannot decay to only **SM** particles without vi-
 1044 olating the conservation of R-parity. The heavier sparticles then decay in chains,
 1045 emitting an **SM** particle in each step, and leaving behind the **LSP** at the end of the
 1046 chain.

1047 3.2 MOTIVATION

4

1048

1049 LONG-LIVED PARTICLES

1050 4.1 MECHANISMS

1051 4.1.1 EXAMPLES IN SUPERSYMMETRY

1052 4.2 PHENOMENOLOGY

1053 4.2.1 DISIMILARITIES TO PROMPT DECAYS

1054 4.2.2 CHARACTERISTIC SIGNATURES

1055

PART III

1056

EXPERIMENTAL STRUCTURE AND RECONSTRUCTION

1057

You can put some informational part preamble text here.

1058

1059 THE LARGE HADRON COLLIDER

1060 The LHC, a two-ring superconducting hadron accelerator, provides high energy
 1061 proton-proton collisions for several large experiments at European Organization
 1062 for Nuclear Research (CERN) in Geneva, Switzerland [3, 4]. It is the largest,
 1063 highest-luminosity, and highest-energy proton collider ever built, and was con-
 1064 structed by a collaboration of more than 10,000 scientists from the more than
 1065 100 countries that contribute to CERN. The original design of the LHC focused on
 1066 providing collision energies of up to 14 TeV and generating enough collisions to
 1067 reveal physics beyond the SM which is predicted to exist at higher energy scales.

1068 The LHC was installed in an existing 27 km tunnel at CERN which was orig-
 1069 inally designed to house the Large Electron Positron collider (LEP) [5]. This al-
 1070 lows the collider to use existing accelerators at the same complex to provide the
 1071 initial acceleration of protons up to 450 GeV before injecting into LHC. The in-
 1072 jected hadrons are accelerated up to as much as 14 TeV while being focused into
 1073 two beams traveling in opposite directions. During this process the protons cir-
 1074 culate around the tunnel millions of times, while the beams are intermittently
 1075 crossed at the four locations of the experiments to provide collisions. These col-
 1076 lision points correspond to the four major LHC experiments: ATLAS, Compact
 1077 Muon Solenoid (CMS), Large Hadron Collider beauty experiment (LHCb), and
 1078 A Large Ion Collider Experiment (ALICE), and Figure 7 shows the layout of the
 1079 experiments both on the surface and below. ATLAS and CMS are both general pur-
 1080 pose, high-luminosity detectors which search for a wide range of new types of
 1081 physics [6, 7]. LHCb studies the interactions of b-hadrons to explore the asymme-
 1082 try between matter and antimatter [8]. ALICE focuses on the collisions of lead
 1083 ions, which the LHC also provides, in order to study the properties of quark-
 1084 gluon plasma [9].

1085 During the first five years of continued operation, after the LHC turned on in
 1086 2010, the LHC has provided four major data collecting periods. In 2010 the LHC
 1087 generated collisions at several energies, starting at 900 GeV. It increased the
 1088 energy from 900 GeV to 2.76 TeV and then subsequently to 7 TeV, with a peak
 1089 luminosity of $2 \times 10^{32} \text{ cm}^{-2}\text{s}^{-1}$, and a total delivered luminosity of 50 pb^{-1} .
 1090 The next run, during 2011, continued the operation at 7 TeV and provided an
 1091 additional 5 fb^{-1} with a peak luminosity of $4 \times 10^{33} \text{ cm}^{-2}\text{s}^{-1}$. The energy was
 1092 then increased to 8 TeV for the data collection during 2012, which provided 23 fb^{-1}
 1093 with a peak luminosity of $7.7 \times 10^{33} \text{ cm}^{-2}\text{s}^{-1}$. After the first long shutdown
 1094 for 2013 and 2014, the LHC resumed operation and increased the energy to 13
 1095 TeV in 2015, where it delivered 4.2 fb^{-1} with a peak luminosity of $5.5 \times 10^{33} \text{ cm}^{-2}\text{s}^{-1}$.
 1096 The LHC is currently providing additional 13 TeV collisions in 2016 with higher
 1097 luminosities than during any previous data collection periods. These running
 1098 periods are summarized in Figure 8, which shows the total delivered

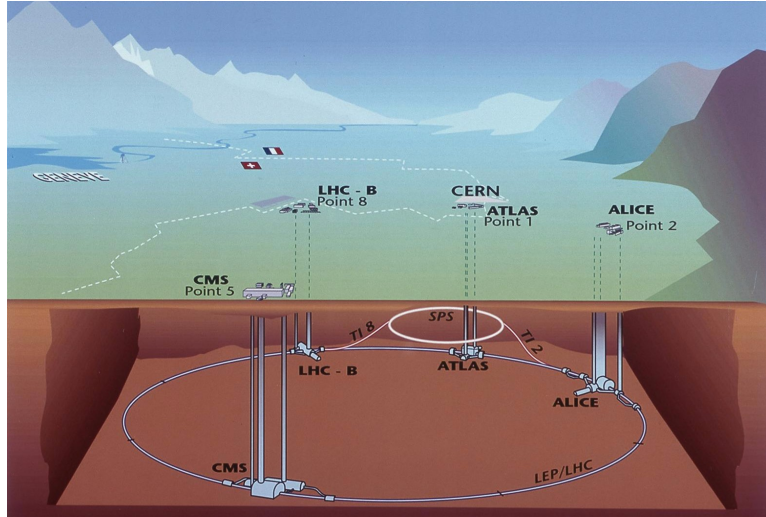


Figure 7: The four collision points and corresponding experiments of the [LHC](#). The image includes the location of the nearby city of Geneva as well as the border of France and Switzerland.

1099 luminosity over time for the [ATLAS](#) experiment during each of the four years of
1100 data collection since 2011.

1101 5.1 INJECTION CHAIN

1102 The [LHC](#) takes advantage of the presence of previously built accelerators at [CERN](#)
1103 to work up to the target energy in consecutive stages. The series of accelerators
1104 that feed into the [LHC](#) are known collectively as the injection chain, and together
1105 with the [LHC](#) form the accelerator complex. The full complex is illustrated in
1106 Figure 9, which details the complex series required to reach collisions of 13 or
1107 14 TeV.

1108 Protons at the [LHC](#) begin as hydrogen atoms in the Linac 2, a linear accelerator
1109 which replaced Linac 1 as the primary proton accelerator at CERN in 1978. In
1110 Linac 2, the hydrogen atoms are stripped of their electrons by a strong magnetic
1111 field, and the resulting protons are accelerated up to 50 MeV by cylindrical con-
1112 ductors charged by radio frequency cavities. The protons are then transferred
1113 to the Proton Synchrotron Booster ([PSB](#)), which uses a stack of four synchrotron
1114 rings to accelerate the protons up to 1.4 GeV. Then the protons are injected
1115 into the Proton Synchrotron ([PS](#)) which again uses synchrotron rings to bring
1116 the energy up to 25 GeV. The intermediate step between Linac 2 and the [PS](#) is
1117 not directly necessary, as the [PS](#) can accelerate protons starting from as low as
1118 50 MeV. The inclusion of the [PSB](#) allows the [PS](#) to accept a higher intensity of
1119 injection and so increases the deliverable luminosity in the [LHC](#). The penulti-
1120 mate stage of acceleration is provided by the Super Proton Synchrotron ([SPS](#)), a
1121 large synchrotron with a 7 km circumference that was commissioned at CERN
1122 in 1976. During this step the protons increase in energy to 450 GeV, after which
1123 they can be directly injected into the [LHC](#).

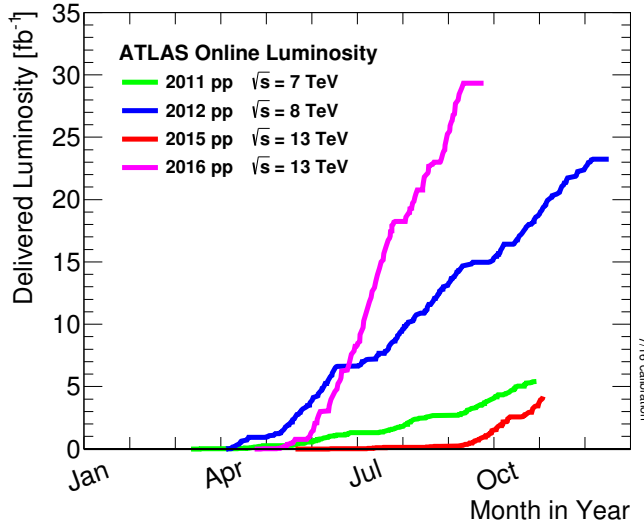


Figure 8: The cumulative luminosity over time delivered to the ATLAS experiment from high energy proton-proton collisions since 2011. The energies of the collisions are listed for each of the data-taking periods.

The final step is the LHC itself, which receives protons from the SPS into two separate beam pipes which circulate in opposite directions. The filling process at this steps takes approximately 4 minutes, and the subsequent acceleration to the final energy (6.5 TeV during 2015 and up to 7 TeV by design) takes approximately half an hour. At this point the protons circulate around the circumference tens of thousands of times a second and continue for up to two hours.

5.2 DESIGN

5.2.1 LAYOUT

Many of the aspects of the LHC design are driven by the use of the existing LEP tunnel. This tunnel slopes gradually, with a 1.4% decline, with 90% of its length built into molasse rock which is particularly well suited to the application. The circumference is composed of eight 2987 meter arcs and eight 528 meter straight sections which connect them; this configuration is illustrated in Figure 10. The tunnel diameter is 3.7 m throughout its length.

The design energy is directly limited by the size of this tunnel, with its radius of curvature of 2804 m. A significant magnetic field is required to curve the protons around that radius of curvature; the relationship is given by

$$p \simeq 0.3BR \quad (13)$$

where p is the momentum of the particle in GeV, B is the magnetic field in Tesla, and R is the radius of curvature in meters. From the target design energy of 14 TeV, or 7 TeV of momentum for protons in each beam, the required magnetic field is 8.33 Tesla. This is too large a field strength to be practical with

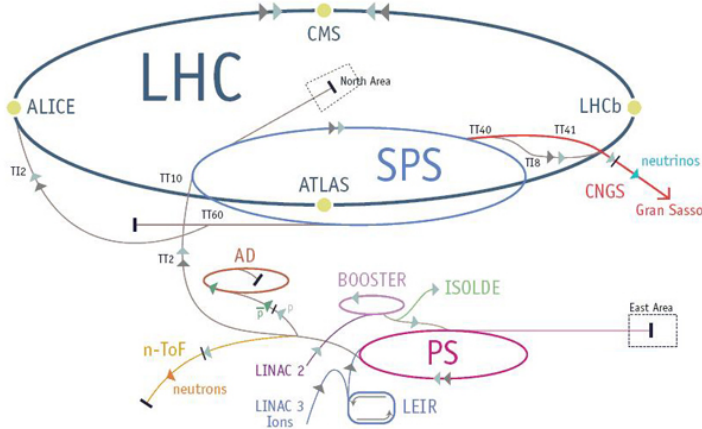


Figure 9: The accelerator complex that builds up to the full design energies at the LHC. The protons are passed in order to Linac 2, the PSB, the PS, the SPS and then the LHC.

iron electromagnets, because of the enormous power required and the resulting requirements for cooling. Because of these constraints, the LHC uses superconducting magnets which can maintain that field strength with significantly less power consumption.

5.2.2 MAGNETS

The magnets chosen were Niobium and Titanium (NbTi) which allow for field strengths as high as 10 Tesla when cooled down to 1.9 K. Reaching the target temperature of 1.9 K for all of the magnets requires superfluid helium and a large cryogenic system along the entire length of the tunnel. During normal operation, the LHC uses 120 tonnes of helium within the magnets, and the entire system is cooled by eight cryogenic helium refrigerators. The temperature increase that occurs during transit from the refrigerator along the beam necessitates that the refrigerators cool the helium down to 1.8 K. Any significant increase above this temperature range can remove the superconductive properties of the magnets, which in turn generates drastically larger heat losses from the current within the magnets and causes a rapid rise in temperature called a quench.

There are approximately 8000 superconducting magnets distributed around the LHC. The 1232 bending magnets, which keep the protons curving along the length of the beam, are twin bore cryodipoles, which allow both proton beams to be accommodated by one magnet and all of the associated cooling structure. Figure 11 shows the cross section of the design for these dipoles. The magnets are very large, 16.5 m long with a diameter of 0.57 meters and a total weight of 28 tonnes. They are slightly curved, with an angle of 5.1 mrad, in order to carefully match the beam path. The twin bore accommodates both magnets inside the two 5 cm diameter holes which are surrounded by the superconducting coils. The coils require 12 kA of current in order to produce the required magnetic field. These coils are comprised of NbTi cable wound in two layers; the wire in

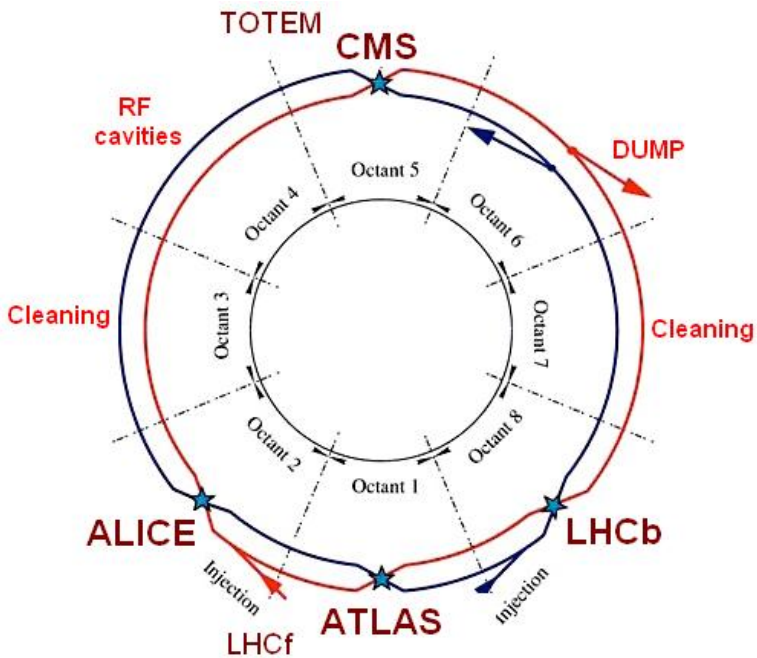


Figure 10: A schematic of the layout of the LHC, not to scale. The arched and straight sections are illustrated at the bottom of the schematic, and all four crossing sites are indicated with their respective experiments.

the inner layer has a diameter of 1.065 mm while the wire in the outer layer has a diameter of 0.825 mm.

The large currents in the wires, along with the magnetic field produced, result in forces on the magnets which would tend to push them apart with over 10,000 Newtons per meter. Constraining the magnets requires a significant amount of structure including non-magnetic stainless steel collars. Both the presence of these electromagnetic forces and the varying thermal contraction coefficient of the pieces of the magnet produce significant forces on the cold mass structure. The cold mass is carefully engineered to so that these stresses do not significantly alter the magnetic field shape, which must be maintained between magnets to a precision of approximately 10^{-4} for successful operation.

The remaining 6800 magnets are a variety of quadrupole, sextapole, octopole, and single bore dipole magnets. These are used to damp oscillations, correct beam trajectories, focus the beams during circulation, and to squeeze the beams before collisions.

5.2.3 RF CAVITIES

Sixteen RF cavities produce the actual acceleration of the proton beam up to the design energy. These RF cavities are tuned to operate at 400 MHz, and are powered by high-powered electron beams modulated at the same frequency, called klystrons. The resonance within the cavity with the oscillating electric field establishes a voltage differential of 2 MV per cavity. The sixteen cavities are split between the two beams, so combined the cavities provide 16 MV per beam,

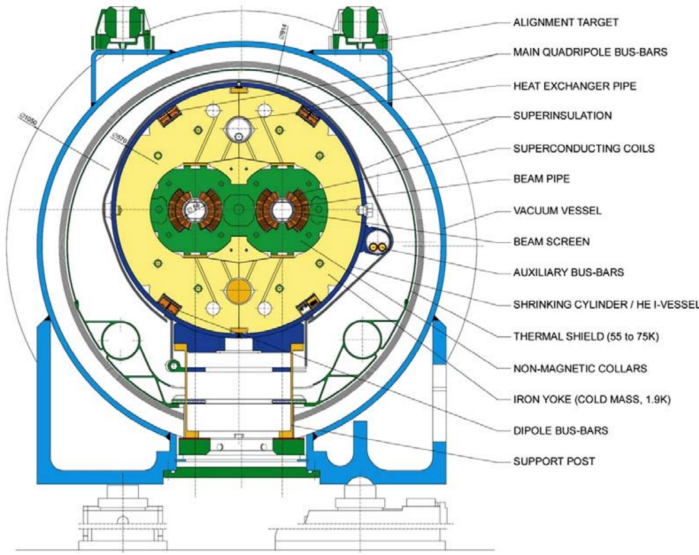


Figure 11: A cross section of the cryodipole magnets which bend the flight path of protons around the circumference of the LHC. The diagram includes both the superconducting coils which produce the magnetic field and the structural elements which keep the magnets precisely aligned.

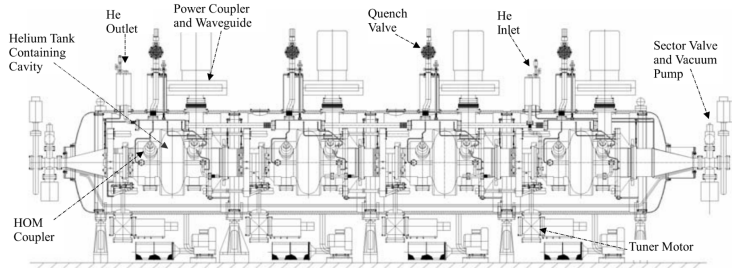


Figure 12: The arrangement of four RF cavities within a cryomodule.

which accelerate the protons on each consecutive pass through the cavity. This acceleration is also necessary during circulation even after the target energy has been reached in order to compensate for losses from synchrotron radiation.

The cavities are arranged in cryomodules which contain four cavities, with two cryomodules per beam; this arrangement is illustrated in Figure 12. These cryomodules are necessary to maintain the superconducting state of the cavities, which are also constructed from niobium. The RF cavities use niobium along with copper to allow for low power losses in the superconductors. The copper provides a reduced susceptibility to quenching, as it rapidly conducts away heat generated by imperfections in the niobium, as well as natural shielding from the earth's magnetic field which can interfere with the RF system.

The nature of the radio frequency oscillations tends to group protons together into buckets. A proton traveling exactly in phase with the RF oscillations will not be displaced at all during a single circulation, and those slightly ahead or behind of that phase will slightly decelerate or accelerate, respectively. This produces

1209 separate clusters of protons which arrive in phase to the cavities every 2.5 ns,
 1210 corresponding to the 400 MHz frequency.

1211 5.2.4 BEAM

1212 The beams of protons circulate within 54 km of 5 cm diameter beam pipe. This
 1213 entire structure is kept under vacuum at 1.9 K to prevent interactions between
 1214 the beam pipe and the magnets as well as to prevent any interactions between the
 1215 circulating protons and gas in the pipe. The vacuum within the pipe establishes
 1216 a pressure as low as 10^{-9} mbar before the protons are introduced.

1217 Because of the very high energies of the circulating protons, synchrotron ra-
 1218 diation is not negligible in the bending regions. The protons are expected to
 1219 radiate 3.9 kW per beam at 14 TeV, with 0.22 W/m, which is enough power to
 1220 heat the liquid helium and cause a quench were it absorbed by the magnets. To
 1221 prevent this, a copper screen is placed within the vacuum tube that absorb the
 1222 emitted photons. This screen is kept between 5 and 20 K by the liquid helium
 1223 cooling system.

1224 5.3 LUMINOSITY PARAMETERS

1225 In addition to the high energy of the collisions, the rate of collisions is extremely
 1226 important to enabling the discovery of new physics. Many measurements and
 1227 searches require a large number of events in order to be able to make statistically
 1228 significant conclusions. The rate of collisions is measured using luminosity, the
 1229 number of collisions per unit time and unit cross section for the proton-proton
 1230 collisions. From the beam parameters, luminosity is given by

$$\mathcal{L} = \frac{N_b^2 n_b f_{rev} \gamma}{4\pi\epsilon_n \beta^*} F \quad (14)$$

1231 where N_b is the number of protons per bunch, n_b is the number of bunches per
 1232 beam, f_{rev} is the frequency of revolution, γ is the Lorentz factor for the protons
 1233 at the circulating energy, ϵ_n is the emittance, β^* is the amplitude function at the
 1234 collision point, and F is a geometric factor that accounts for the crossing angle of
 1235 the beams at the collision point. The emittance measures the average spread of
 1236 particles in both position and momentum space, while the amplitude function
 1237 is a beam parameter which measures how much the beam has been squeezed.
 1238 Together ϵ_n and β^* give the size of the beam in the transverse direction, $\sigma = \sqrt{\epsilon \beta^*}$. β changes over the length of the beam as the accessory magnets shape the
 1239 distribution of protons, but only the value at the point of collisions, β^* , affects
 1240 the luminosity.

1241 The luminosity is maximized to the extent possible by tuning the parameters
 1242 in Equation 14. A number of these are constrained by the design decisions. The
 1243 revolution frequency is determined entirely by the length of the tunnel, as the
 1244 protons travel at very close to the speed of light. The geometric factor F is de-
 1245 termined by the crossing angle of the beams at the collision points, again a com-

Parameter	Unit	Injection	Nominal
Beam Energy	TeV	0.450	7
Peak Instantaneous Luminosity	$\text{cm}^{-2}\text{s}^{-1}$	-	10^{34}
Bunch Spacing	ns	25	25
Number of Filled Bunches	-	2808	2808
Normalized Transverse Emittance	μm	3.75	3.75
Frequency	MHz	400.789	400.790
RF Voltage/Beam	MV	8	16
Stored Energy	MJ	-	362
Magnetic Field	T	0.54	8.33
Operating Temperature	K	1.9	1.9

Table 2: The design parameters of the [LHC](#) beam that determines the energy of collisions and the luminosity, for both the injection of protons and at the nominal circulation.

ponent of the tunnel design; this angle is already very small at $285 \mu\text{rad}$, which helps to maximize the geometric factor.

The major pieces that can be adjusted are the number of protons per bunch, N_b , the number of bunches in the beam, n_b , and the amplitude function β . Increasing either N_b or n_b increases the amount of energy stored in the beam, which presents a danger if control of the beam is lost. At design specifications, the beam stores 362 MJ, which is enough energy to damage the detectors or accelerator if the beam were to wander out of the beam pipe. So, the luminosity is primarily controlled at the [LHC](#) by adjusting β^* , where lowering β^* increases the luminosity. β^* is tuned to provide the various values of luminosity used at the [LHC](#) which can be raised to as much as 10^{34} .

The nominal bunch structure consists of 3654 bunches, each holding 10^{11} protons, which cross a collision point in 25 ns. These are further subdivided into the buckets mentioned in Section 5.2.3 by the clustering properties of the RF cavities. The bunches are further grouped into trains of 72 bunches which are separated by a gap which would otherwise hold 12 bunches. At nominal operation 2808 of the bunches will actually be filled with protons, while the remainder are left empty to form an abort gap that can be used in case the beam needs to be dumped.

The various beam parameters are summarized in Table 2 for the designed operation. In practice, the beam has operated at lower energies and lower luminosities than the design values for the majority of its lifetime, but the [LHC](#) has begun to operate at full design values during Run 2.

5.4 DELIVERED LUMINOSITY

During the data collection of 2015, the [LHC](#) operated at luminosities as large as $5 \times 10^{33} \text{ cm}^{-2}\text{s}^{-1}$. It is convenient to refer to the integrated luminosity, the inte-

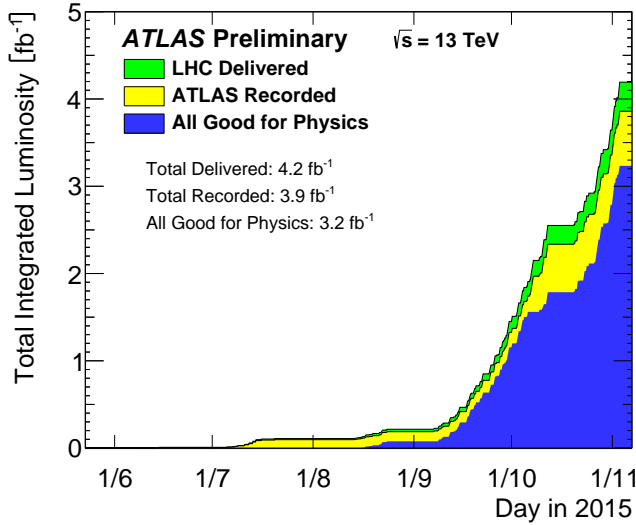


Figure 13: The cumulative luminosity versus time delivered to ATLAS (green), recorded by ATLAS (yellow), and certified to be good quality data (blue) during stable beams for pp collisions at 13 TeV in 2015.

gral of the instantaneous luminosity, which corresponds directly to the number of delivered events for a given process.

$$N = \sigma \times \int \mathcal{L}(t) dt$$

where σ is the cross section for the process of interest. The integrated luminosity over time is shown in Figure 13. This includes the luminosity delivered by the LHC as well as the luminosity that was recorded by ATLAS. ATLAS only records collisions when the LHC reports that the beam conditions are stable, so some of the delivered luminosity is not recorded. The figure also includes the amount of luminosity marked as good for physics, which includes additional requirements on the operation of the detector during data collection that are necessary for precise measurements.

Because the beam circulates and collides bunches of protons, it is possible for a single crossing to produce multiple proton-proton collisions. As the instantaneous luminosity is increased, the average number of collisions generated per bunch crossing increases. An event refers to the entire collection of interactions during a single bunch crossing, while interactions refer to the individual proton-proton collisions. The additional interactions produced during each bunch crossing are referred to as pileup, which can be more precisely defined quantified using the average number of additional proto-proton interactions per crossing, often denoted μ . Figure 14 shows the luminosity-weighted distribution of the mean number of interactions for events collected in 2015. The presence of as many as twenty interactions in a single collision provides a significant challenge in reconstructing events and isolating the targeted physical processes.

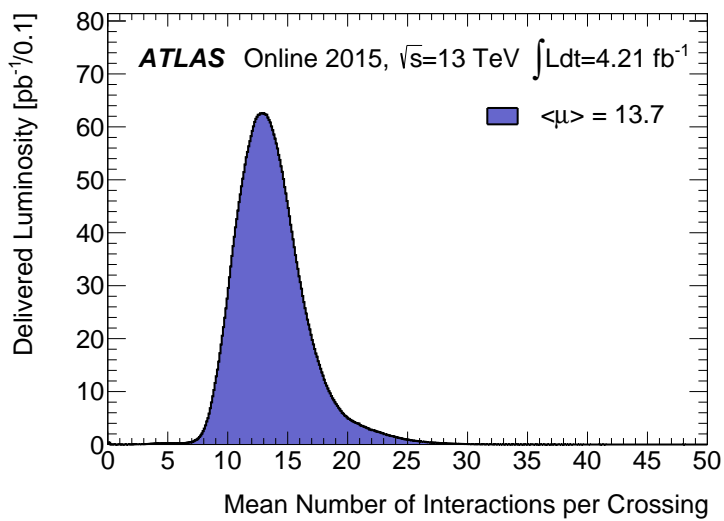


Figure 14: The luminosity-weighted distribution of the mean number of interactions per crossing for the 2015 pp collision data at 13 TeV.

1290

1291 THE ATLAS DETECTOR

1292 The four major LHC experiments at CERN seek to use the never before matched
1293 energies and luminosities of the new collider to explore the boundaries of par-
1294 ticle physics and to gain insight into the fundamental forces of nature. Two of
1295 these experiments, ATLAS and CMS, are general purpose detectors that seek to
1296 measure a variety of processes in the up to 14 TeV proton-proton collisions that
1297 occur as much as 40 million times per second at the LHC at the design luminosity
1298 of $10^{34} \text{ cm}^{-2}\text{s}^{-1}$. ATLAS employs a hermetic detector design, one which encloses
1299 the particle collisions as completely as possible with detecting elements, that al-
1300 lows it to study a wide range of physics from SM and Higgs measurements to
1301 searches for new physics in models like Supersymmetry [6].

1302 Accommodating this wide variety of goals is a challenge for the design of the
1303 detector. The wide range of energies involved requires high measurement pre-
1304 cision over several orders of magnitude and the ability to measure a variety of
1305 particle types. At the time of the construction of ATLAS, the Higgs boson had yet
1306 to be discovered, but the diphoton decay mode was (correctly) expected to be
1307 important and necessitated a high resolution photon measurement. The poten-
1308 tial for decays of new heavy gauge bosons, W' and Z' , required a similarly high
1309 momentum resolution for leptons with momentum up to several TeV. Hadronic
1310 decay modes of several possible new high energy particles could result in very
1311 energetic jets, again up to several TeV, and reconstructing the decay resonances
1312 would again require good energy resolution. Several models, such as SUSY or Ex-
1313 tra Dimensions, predict the existence of particles which would not interact with
1314 traditional detecting elements. However these particles can still be observed in a
1315 hermetic detector by accurately measuring the remaining event constituents to
1316 observe an imbalance in energy called missing energy or E_T^{miss} . Measuring E_T^{miss}
1317 implicitly requires a good resolution on all SM particles that can be produced.
1318 And at the lower end of the energy spectrum, precision SM measurements would
1319 require good resolution of a variety of particle types at energies as low as a few
1320 GeV, so the design needs to accommodate roughly three orders of magnitude.

1321 This broad spectrum of measurements requires a variety of detector systems
1322 working together to form a cohesive picture of each collision. Two large magnet
1323 systems provide magnetic fields that provide a curvature to the propagation of
1324 charged particles and allows for precision momentum measurements by other
1325 systems. The inner detector uses a combination of tracking technologies to re-
1326 construct particle trajectories and vertices for charged particles. A variety of
1327 calorimeters measure the energies of hadrons, electrons, and photons over a
1328 large solid angle. A large muon spectrometer identifies muons and uses the sec-
1329 ond magnet system to provide an independent measurement of their momentum
1330 from the inner detector and improve the resolution. The layout of all of these
1331 systems is shown in Figure 15.

1332 The performance goals needed to achieve the various targeted measurements
 1333 and searches discussed above can be summarized as resolution and coverage re-
 1334 quirements on each of these systems. Those requirements are listed in Table 3.

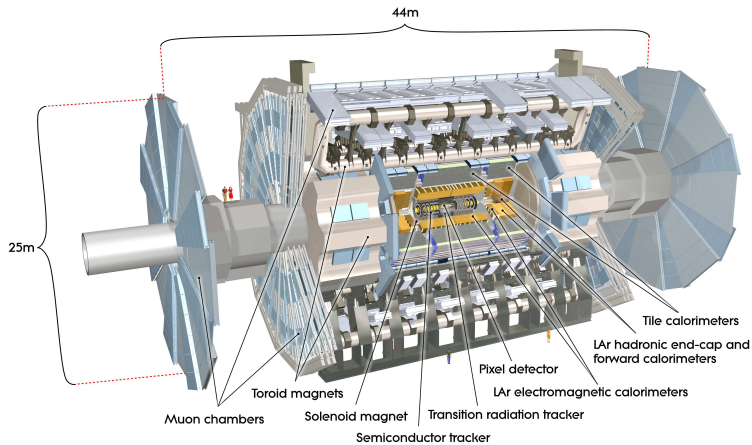


Figure 15: A cut-away schematic of the layout of the [ATLAS](#) detector. Each of the major subsystems is indicated.

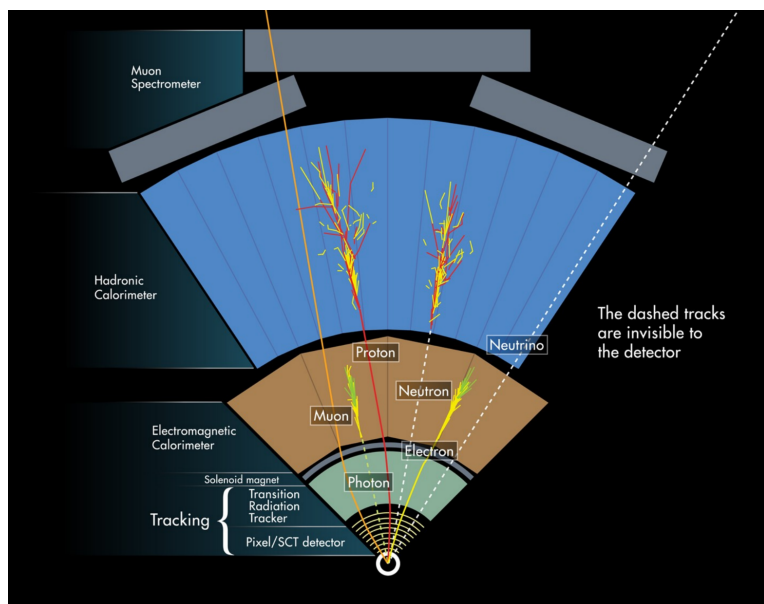


Figure 16: A cross-sectional slice of the [ATLAS](#) experiment which illustrates how the various SM particles interact with the detector systems.

1335 Incorporating these various pieces into a single detector is a significant tech-
 1336 nical challenge. The resulting detector has a diameter of 22 m, is 46 m long,
 1337 and weighs 7,000 tons; it is the largest volume particle detector ever constructed.
 1338 The various detector elements need to be constructed and assembled with pre-
 1339 cision as low as micrometers. These systems all need to function well even after
 1340 exposure to the significant radiation dose from the collisions. Designing, con-
 1341 structing, and installing the detector took the combined effort of more than 3000
 1342 scientists from 38 countries over almost two decades.

Detector Component	Required Resolution	$ \eta $ Coverage	
		Measurement	Trigger
Tracking	$\sigma_{p_T}/p_T = 0.05\% p_T + 1\%$	2.5	-
EM Calorimetry	$\sigma_E/E = 10\%/\sqrt{E} + 0.7\%$	3.2	2.5
Hadronic Calorimetry			
Barrel and Endcap	$\sigma_E/E = 50\%/\sqrt{E} + 3\%$	3.2	3.2
Forward	$\sigma_E/E = 100\%/\sqrt{E} + 10\%$	3.1 – 4.9	3.1 – 4.9
Muon Spectrometer	$\sigma_{p_T}/p_T = 10\% \text{ at } p_T = 1 \text{ TeV}$	2.7	2.4

Table 3: The performance goals for each of the subsystems of the [ATLAS](#) detector. The $|\eta|$ coverage specifies the range where the subsystem needs to be able to provide measurements with the specified resolution. The resolutions include a p_T or E dependence that is added in quadrature with a p_T/E independent piece.

1343 6.1 COORDINATE SYSTEM

1344 The coordinate system defined for the [ATLAS](#) detector is used throughout all of
 1345 the sections of this thesis. The choice of coordinate system reflects the cylindri-
 1346 cal symmetry of the [ATLAS](#) detector, and is oriented by the direction of the
 1347 beamline which defines the z -direction. The positive z side of the detector is
 1348 commonly referred to as the A -side, and the negative z side is referred to as
 1349 the C -side. The $x - y$ plane is then the plane transverse to the beam direction,
 1350 with the x direction defined as pointing from the interaction point to the center
 1351 of the [LHC](#) ring and the y direction defined as pointing upwards. The nominal
 1352 interaction point is the origin of this system.

1353 It is more convenient in practice to use a cylindrical coordinate system. The
 1354 angle from the z -axis is θ . The azimuthal angle uses the usual definition, with ϕ
 1355 running around the z -axis and $\phi = 0$ corresponding to the x -axis. Many aspects
 1356 of the detector are independent of the this coordinate to first order. The re-
 1357 maining direction is typically specified using rapidity or pseudorapidity, where
 1358 rapidity is defined as

$$y = \frac{1}{2} \ln \frac{E + p_z}{E - p_z} \quad (15)$$

1359 Rapidity is particularly useful to indicate the component along the z direction
 1360 because differences in rapidity are invariant to boosts along the z -direction. A
 1361 similar quantity which depends only the θ is pseudorapidity,

$$\eta = -\ln \tan \frac{\theta}{2} \quad (16)$$

1362 which is the same as rapidity when the particle is massless and in the limit where
 1363 the energy is much larger than the particle's mass. It is often useful to refer to
 1364 differences in solid angle using the pseudorapidity and the azimuthal angle:

$$\Delta R = \sqrt{\Delta\phi^2 + \Delta\eta^2} \quad (17)$$

1365 The pseudorapidity is also invariant to boosts along the z -axis for high mo-
 1366 mentum particles, and is preferable to rapidity because it does not depend on
 1367 the specific choice of particle. Pseudorapidity is also preferable to θ because
 1368 of the aforementioned boost-invariance and also because particle production is
 1369 roughly uniform in equal-width intervals of η up to about $\eta = 5.0$. A particle
 1370 traveling along the beampipe has $\eta = \text{inf}$ and a particle traveling perpendicular
 1371 to the beampipe has $\eta = 0$. The extent of the tracker, $|\eta| < 2.5$, corresponds
 1372 to approximately $0.05\pi < \theta[\text{rad}] < 0.95\pi$ and the extent of the calorimeters,
 1373 $|\eta| < 4.9$ corresponds to approximately $0.005\pi < \theta[\text{rad}] < 0.995\pi$. Many de-
 1374 tector components are broken into multiple subsystems to provide coverage at
 1375 greater $|\eta|$. The lower $|\eta|$ region is referred to as the barrel, typically with $|\eta| \lesssim 2$,
 1376 and the greater $|\eta|$ region is often referred to as the endcap.

1377 The initial energy and momentum of a proton-proton collision along the z di-
 1378 rection is unknown in hadron colliders because different energies and momenta
 1379 can be carried by the partons. Along the transverse plane, however, the vector
 1380 sum of momentum will be zero. For this reason, many physical quantities are
 1381 quantified in terms of their projection onto the transverse plan, such as p_T or
 1382 E_T . In addition, p_T alone determines the amount of curvature in the magnetic
 1383 field, and can be measured independently by measuring the curvature of a parti-
 1384 cle's propagation.

1385 6.2 MAGNETIC FIELD

1386 The magnet system used in [ATLAS](#) is designed to provide a substantial magnetic
 1387 field in the two regions where the trajectory of particles is measured, the inner
 1388 detector and the muon spectrometer. The magnetic field provides a curvature
 1389 to the trajectory of charged particles and allows the precision tracking measure-
 1390 ments to make high resolutions measurements of p_T . To provide a magnetic field
 1391 in these regions, [ATLAS](#) uses a hybrid system with four separate, superconduct-
 1392 ing magnets. A single solenoid provides a 2 T axial magnetic field for the inner
 1393 detector, while a barrel toroid and two endcap toroids produce a magnetic field
 1394 of 0.5 and 1 T, respectively, for the muon detectors. This geometry is illustrated
 1395 in Figure 17, and the parameters of the three magnet systems are summarized in
 1396 Table 4.

1397 The central solenoid uses a single-layer coil with a current of 7.730 kA to gen-
 1398 erate the 2 T axial field at the center of the magnet. The single-layer coil design
 1399 enables a minimal amount of material to be used in the solenoid's construction,
 1400 which is important because the solenoid is placed between the inner detector
 1401 and the calorimeters. At normal incidence the magnet has only 0.66 radiation
 1402 lengths worth of material, where one radiation length is the mean distance over

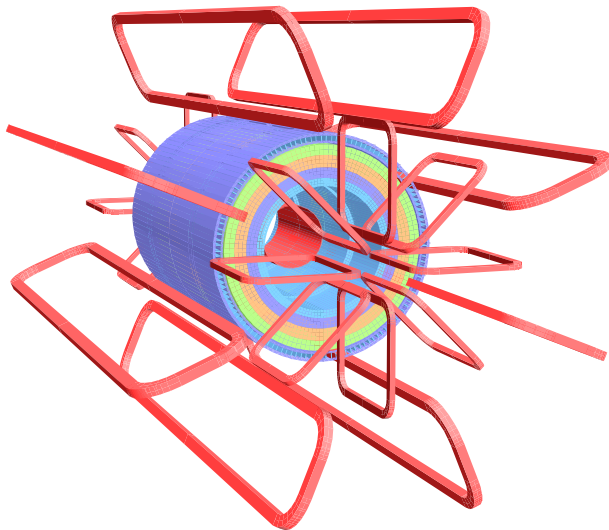


Figure 17: The layout of the four superconducting magnets in the [ATLAS](#) detector.

Parameter	Unit	Solenoid	Barrel Toroid	Endcap Toroids
Inner Diameter	m	2.4	9.4	1.7
Outer Diameter	m	2.6	20.1	10.7
Axial Length	m	5.3	25.3	5.0
Weight	tons	5.7	830	239
Conductor Size	mm ²	30×4.25	57×12	41×4.25
Peak Field	T	2.6	3.9	4.1
Heat Load	W	130	990	330
Current	kA	7.7	20.5	20.0
Stored Energy	MJ	38	1080	206

Table 4: A summary of the parameters of each of the three magnet systems on [ATLAS](#).

1403 which a high-energy electron loses all but $1/e$ of its energy through material in-
 1404 teractions [10]. The coil is made of a high-strength aluminum stabilized NbTi
 1405 superconductor which was optimized to achieve a high field with minimal thick-
 1406 ness. The axial magnetic field produced by the solenoid bends charged particles
 1407 in the ϕ direction.

1408 The barrel toroid consists of eight coils which generate a 0.5 T magnetic field
 1409 in the cylindrical region around the calorimeters with an approximately 20 kA
 1410 current. The coils are separated only by air to reduce the scattering of muons as
 1411 they propagate through the region. The coils are made of an aluminum stabilized
 1412 NbTiCu superconductor and each is separately housed in a vacuum and cold
 1413 chamber. This magnetic configuration produces a field in the ϕ and so curves
 1414 muons traversing the volume primarily in the η direction.

1415 The endcap toroids follow a similar design to the barrel toroid, with eight
 1416 separate NbTiCu coils, but in this case all eight are housed within a single cold
 1417 mass. This extra structure is necessary to withstand the Lorentz forces exerted
 1418 by the magnets. These magnets are rotated 22.5% relative to the barrel toroid to
 1419 provide a uniform field in the transition between the two systems. The endcap
 1420 toroids also produce a field in the ϕ direction and curve muons primarily in the
 1421 η direction.

1422 6.3 INNER DETECTOR

1423 The [ATLAS](#) inner detector provides excellent momentum resolution as well as
 1424 accurate primary and secondary vertex measurements through robust pattern
 1425 recognition that identifies tracks left by charged particles. These tracks fulfill
 1426 a number of important roles in the [ATLAS](#) measurement system: they measure
 1427 the momentum of charged particles including electrons and muons, they can
 1428 identify electrons or photon conversions, they assign various particles and jets
 1429 to different vertices, and they provide a correction to E_T^{miss} measurements from
 1430 low energy particles. The system has to be accurate enough to separate tracks
 1431 from dozens of vertices and to resolve each vertex individually, as well as accu-
 1432 rate enough to measure the p_T of very high momentum tracks which curve very
 1433 little even in the large magnetic field. This is accomplished by several indepen-
 1434 dent layers of tracking systems. Closest to the interaction point is the very high
 1435 granularity Pixel detector, which is followed by the [SCT](#) layers. These subdetec-
 1436 tors both use discrete space-points to reconstruct track patterns. The final layer,
 1437 the transition radiation tracker ([TRT](#)), uses many layers of straw tube elements
 1438 interleaved with transition radiation material to provide continuous tracking.
 1439 The arrangement of these subdetectors is shown in Figure 18. To provide the
 1440 desired hermetic coverage, the subdetectors are divided into barrel and endcap
 1441 geometries. Figure 19 shows the layout of the subdetectors in more detail, and
 1442 illustrates how tracks at various pseudorapidities can traverse the subdetectors;
 1443 tracks with $\eta > 1.1$ begin to traverse the endcap subdetectors rather than those
 1444 in the barrel, and tracks with $\eta > 1.7$ use primarily endcap elements. The [IBL](#)
 1445 was not present during the original commissioning of the inner detector and is
 1446 not shown in this figure.

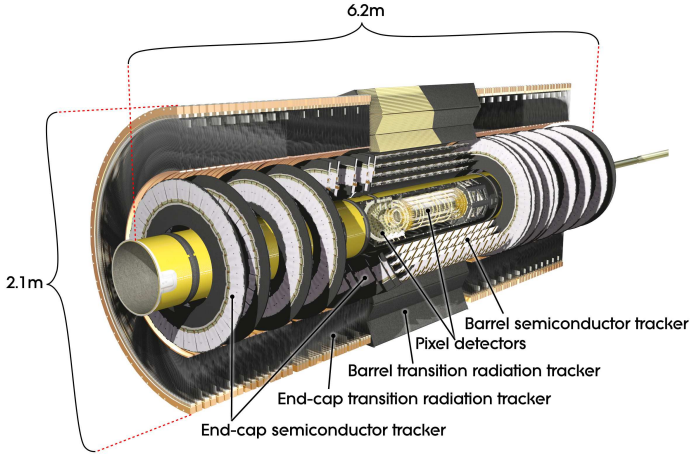


Figure 18: The arrangement of the subdetectors of the ATLAS inner detector. Each of the subdetectors is labeled in the cut-away view of the system.

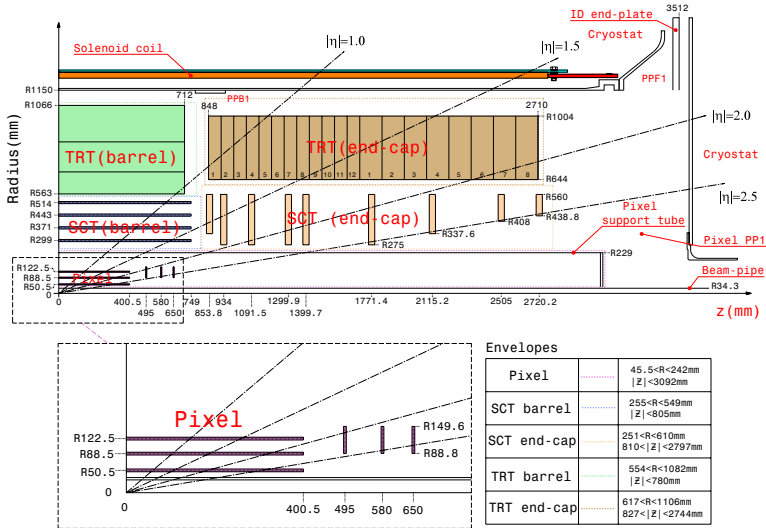


Figure 19: A quarter section of the ATLAS inner detector which shows the layout of each of the subdetectors in detail. The lower panel shows an enlarged view of the pixel detector. Example trajectories for a particle with $\eta = 1.0, 1.5, 2.0, 2.5$ are shown. The IBL, which was added after the original detector commissioning, is not shown.

1447 Figure 20 shows a computer generated three-dimensional view of the inner
 1448 detector along the beam axis, which emphasizes the straw tube structure of the
 1449 **TRT** as well as the overlapping geometry of the **SCT**. This figure also includes
 1450 the **IBL**, which was added during the long shutdown and provides an additional
 1451 measurement layer in the Pixel detector as of the beginning of Run 2. Figure 21
 1452 shows an alternative computer generated three-dimensional view transverse to
 1453 the beam axis which emphasizes the endcap structures of the **SCT** and **TRT**.

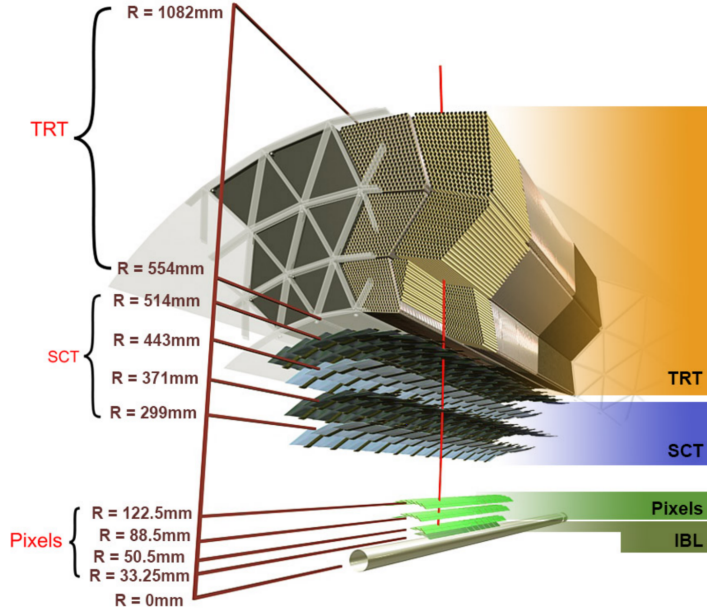


Figure 20: A computer generated three-dimensional view of the inner detector along the line of the beam axis. The subdetectors and their positions are labeled.

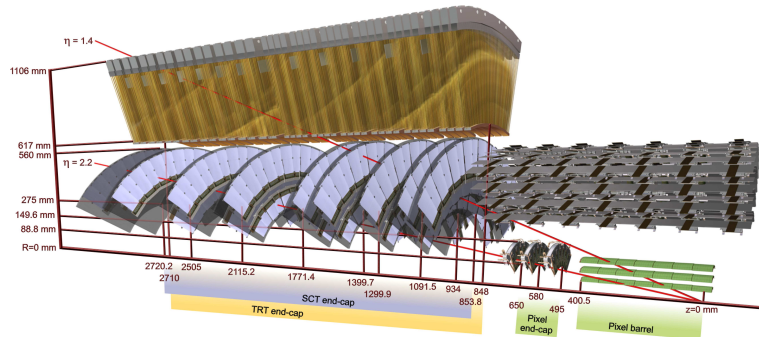


Figure 21: An alternative computer generated three-dimensional view of the inner detector transverse to the beam axis. The subdetectors and their positions are labeled.

1454 As the closest system to the interaction point, it is crucial for the inner de-
 1455 tector to use as little material as possible to avoid scattering of charged parti-
 1456 cles or photon conversions before they reach the remaining subdetectors. The
 1457 various components, including the readout electronics, cooling infrastructure,
 1458 gas volumes, and support structures, were designed to use as little material as

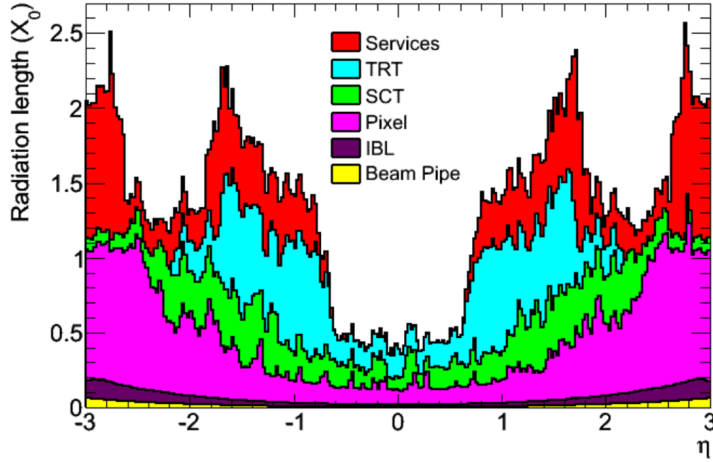


Figure 22: The integrated radiation lengths traversed by a straight track at the exit of the ID envelope, including the services and thermal enclosures. The distribution is shown as a function of $|\eta|$ and averaged over ϕ . The breakdown indicates the contributions of individual sub-detectors, including services in their active volume.

possible. Even with these optimizations, the combination of stringent performance requirements and the harsh radiation environment in the inner detector requires a significant amount of material. This material causes many electrons to lose most of their energy before reaching the electromagnetic calorimeter and approximately 40% of photons convert into an electron-positron pair while traversing the inner detector. Figure 22 shows the integrated radiation lengths traversed by a straight track in the inner detector as a function of η , grouped by subdetector. There is a large increase in the amount of material for support structures around $|\eta| = 1.7$, where the inner detector transitions from barrel to endcap.

The inner detector is designed to work as a cohesive unit to provide complete tracking information for charged particulars, and the subdetectors are complementary. Table 5 summarizes the parameters of each of the subdetectors as well as the parameters of the combined inner detector. Table 6 summarizes the expected performance that can be achieved by the inner detector as a whole.

6.3.1 PIXEL DETECTOR

The Pixel detector is the closest detector to the interaction point and therefore is designed to provide extremely high granularity while simultaneously handling a very large dose of radiation from collisions. It consists of four layers of silicon pixel modules, each of which provides a precision measurement on the trajectory of any charged particle. In the barrel region, the four layers are located at radial distances of 31 mm, 51 mm, 89 mm, and 123 mm. The three outer layers also include endcap elements, illustrated in Figure 19, which are located at 495 mm, 580 mm, and 650 mm away from the interaction point.

Parameter	Inner Detector	Pixel	SCT	TRT
Inner Radius	3.1 cm	3.1 cm	30 cm	56 cm
$ \eta $ Coverage	-	2.5	2.5	2.0
Cell Width	-	50 μm	80 μm	4 mm
Cell Length	-	400 μm	12 cm	70 cm
Material at $ \eta = 0.0$	$0.3 X/X_0$			
Material at $ \eta = 1.7$	$1.2 X/X_0$			
Material at $ \eta = 2.5$	$0.5 X/X_0$			
Number of Hits	48	4	8	36
Channels	99 M	92 M	6.3 M	350 k

Table 5: A summary of the parameters of the inner detector and each of the subdetectors [6].

1483 The pixel sensor technology uses a p-n junction of n-type bulk that contains
 1484 both p⁺ and n⁺ impurities. This combination is crucial in maintaining perfor-
 1485 mance after a significant radiation dose, as the n⁺ implants allow the sensor to
 1486 continue function after the n-type bulk has been converted to a p-type bulk by
 1487 the accumulation of radiation.

1488 The size of the pixels in the original three layers are 50 $\mu\text{m} \times$ 400 μm in the
 1489 $r - \phi$ and z directions, respectively. Those pixels are bump-bonded to front-end
 1490 readout chips, the FE-I3, which contains a total of 2880 pixels per chip. In the
 1491 three original pixel layers, the chips are grouped into modules composed of 16
 1492 chips each with 46,080 pixels per module and a total size of 20 mm x 60 mm
 1493 x 250 μm . The modules are further arranged into long rectangular structures
 1494 that run parallel to the beamline called staves. By tiling several staves with an
 1495 offset of 20°, the stave geometry provides full azimuthal coverage in the barrel
 1496 region while accommodating the readout and cable systems. The endcap regions
 1497 are instead arranged into petals and then into wheels. This arrangement can be
 1498 seen in Figure 23 which shows a computer-generated, cut-away image of the
 1499 outer three layers of the pixel detector. Together these three layers contain 1744
 1500 modules between the barrel and two endcap sections.

1501 The innermost layer, the IBL, was added during the long shutdown before Run
 1502 2, and provides the fourth track measurement. It was inserted directly into the
 1503 existing pixel detector by removing the existing beam pipe and replacing it with
 1504 a significantly smaller version. This insertion can be seen in action in Figure 24,
 1505 which emphasizes the extreme precision required to place the the 70 cm long
 1506 layer with only 2 mm of clearance. The IBL was commissioned to provide con-
 1507 tinued tracking robustness and high precision in the higher luminosity environ-
 1508 ment of Run 2 [12]. The proximity of this layer to the collisions necessitated an
 1509 even higher granularity and better radiation hardness than the other pixel lay-
 1510 ers. And the strict space requirements to add an active sensing layer so close to
 1511 the interaction point required a sensor chip with a much higher active area and
 1512 a larger overall area per chip. These requirements led to the development of a

Parameter	Particle	Value
Reconstruction Efficiency	Muon, $p_T = 1 \text{ GeV}$	96.8%
	Pion, $p_T = 1 \text{ GeV}$	84.0%
	Electron, $p_T = 5 \text{ GeV}$	90.0%
Momentum Resolution	$p_T = 1 \text{ GeV}, \eta \approx 0$	1.3%
	$p_T = 1 \text{ GeV}, \eta \approx 2.5$	2.0%
	$p_T = 100 \text{ GeV}, \eta \approx 0$	3.8%
	$p_T = 100 \text{ GeV}, \eta \approx 2.5$	11%
Transverse IP Resolution	$p_T = 1 \text{ GeV}, \eta \approx 0$	$75 \mu\text{m}\%$
	$p_T = 1 \text{ GeV}, \eta \approx 2.5$	$200 \mu\text{m}$
	$p_T = 1000 \text{ GeV}, \eta \approx 0$	$11 \mu\text{m}$
	$p_T = 1000 \text{ GeV}, \eta \approx 2.5$	$11 \mu\text{m}$
Longitudinal IP Resolution	$p_T = 1 \text{ GeV}, \eta \approx 0$	$150 \mu\text{m}\%$
	$p_T = 1 \text{ GeV}, \eta \approx 2.5$	$900 \mu\text{m}$
	$p_T = 1000 \text{ GeV}, \eta \approx 0$	$90 \mu\text{m}$
	$p_T = 1000 \text{ GeV}, \eta \approx 2.5$	$190 \mu\text{m}$

Table 6: A summary of the expected performance of the combined inner detector [11]. Included are the reconstruction efficiencies for multiple particle types as well as the momentum and IP resolution for various momenta.

1513 new chip type, the FE-I4 (compared to the FE-I3 chips used in the original pixel
 1514 detector) with improved radiation hardness and a larger active footprint of 90%.
 1515 The IBL is comprised of 448 of these individual chips arranged in 14 staves, with
 1516 26,880 pixels per chip and a chip size of 18.5 mm x 41.3 mm x 200 μm . The
 1517 staves, like in the other layers of the pixel detector, are offset by 14° to provide
 1518 full azimuthal coverage. This arrangement can be seen in Figure 25, which shows
 1519 two computer-generated images of the IBL geometry and includes the some of
 1520 the remaining pixel layers.

1521 6.3.2 SEMICONDUCTOR TRACKER

1522 The SCT, the subdetector which immediately surrounds the Pixel detector, pro-
 1523 vides additional discrete measurements of the trajectory of a charged particle.
 1524 Because the SCT is further away from the interaction point, the spatial resolution
 1525 does not need to be as high as in the pixel detector, and so the SCT uses micro-
 1526 strips instead of pixels. Although pixels provide a more accurate measurement,
 1527 the number of pixels and readout channels required to cover the cylindrical area
 1528 at the radius of the SCT layers would be prohibitively complicated and expensive.
 1529 Each individual silicon strip sensor contains 768 individual readout strips
 1530 with a total area of 6.36 cm x 6.40 cm and a pitch of 80 μm . Pairs of these sen-
 1531 sors are then bonded together to form a combined strip with a length of 12.8 cm.
 1532 Two of these combined strips are then placed back to back with a relative tilt

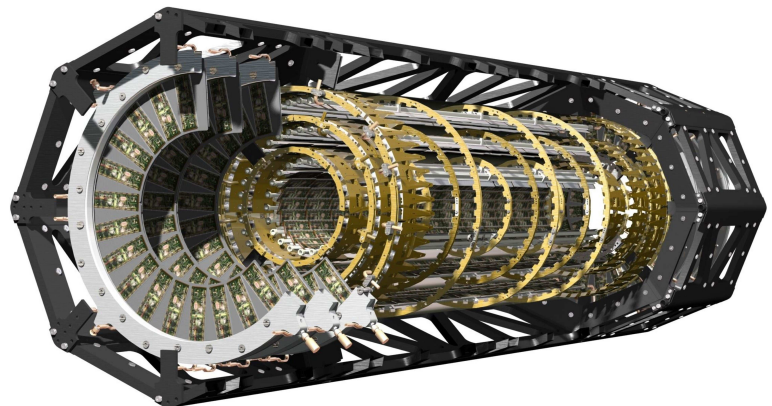


Figure 23



Figure 24: An image of the insertion of the [IBL](#) into the current pixel detector.

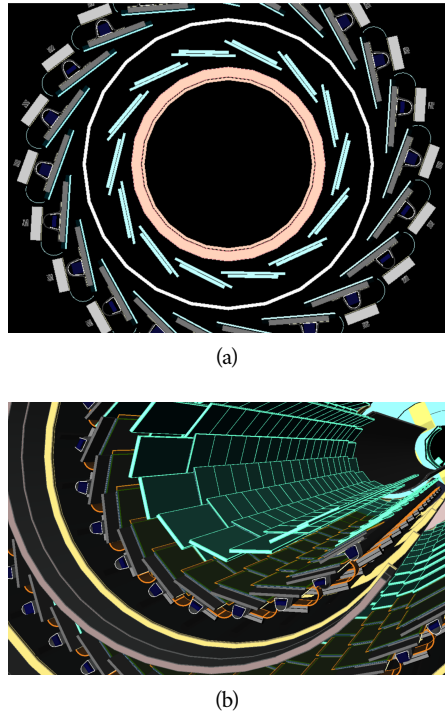


Figure 25: A three-dimensional computer-generated image of the geometry of the [IBL](#) with a view (a) mostly transverse to the beam pipe (b) mostly parallel to the beam pipe.

of 40 mrad. This geometry is illustrated in an exploded-out view in Figure 26. The purpose of angular offset of the consecutive layers is to allow the strip sensor areas to more accurately measure the position of a particle by comparing the overlap of the two strips which were traversed by a track.

Four of these double layers are placed in the barrel region, with radii of 284 mm, 355 mm, 427 mm, and 498 mm. Together these layers provide eight additional measurements for each track that traverses the central $|\eta|$ region. In the endcap region, the layers are arranged in wheels, with the double layers similarly offset to provide improved resolution. With these configurations, the [SCT](#) achieves a spatial resolution of $17 \mu\text{m}$ in the $r - \phi$ direction and $580 \mu\text{m}$ in the z direction.

6.3.3 TRANSITION RADIATION TRACKER

The final component of the inner detector, the [TRT](#), provides continuous tracking using straw drift tubes. The tubes are made of Kapton and aluminum with a diameter of 4 mm and are filled with a gas mixture of 70% Xe, 27% CO₂, and 3% O₂. At the center of each tube is a gold-plated anode tungsten wire $30 \mu\text{m}$ in diameter. When a charged particle passes through these tubes, it ionizes the gas within. The ions produced drift in the electric field established between the wire and the tube wall, and the large electric field near the wire produces avalanche multiplication and results in an electric current on the wire that is read out by the electronics and provides a track measurement. The time it takes the ioniza-

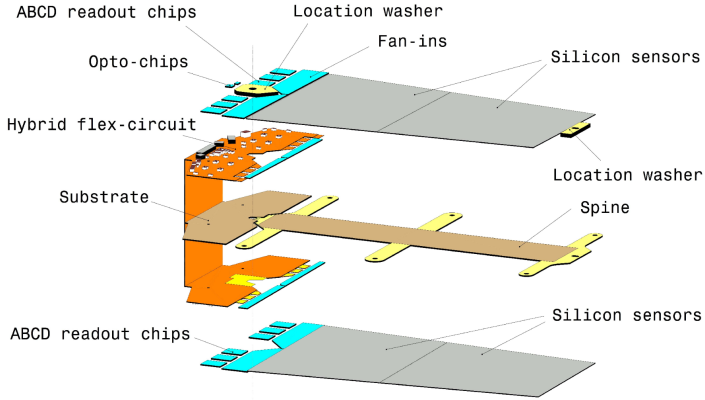


Figure 26: An exploded view of the geometry of the [SCT](#) double layers in the barrel region.

tion to drift to the wire can be used to estimate the distance from the wire that the particle passed through the tube; this gives a resolution on the distance of approximately $130\mu\text{m}$. Combining several such measurements between consecutive hits in the [TRT](#) tubes allows the trajectory of the particle to be reconstructed.

In addition to the continuous tracking, the detector can use transition radiation produced when a particle passes between the layers to distinguish between electrons and heavier charged particles. The space between the tubes is filled with CO_2 , and so has a different dielectric constant than the gas within the tubes which contains Xe. At the transition between those media, a relativistic particle emits radiation proportional to γ , so inversely proportional to mass at a fixed momentum. The photons produced in this transition then produces an ionization cascade which is significantly larger than the signal for the minimally-ionizing charged particles. To distinguish between these two cases, the [TRT](#) defines two signal thresholds, a low threshold for the typical signal produced by a minimally ionizing particle ([MIP](#)) and a high threshold for the the signal produced by transition radiation. A high momentum electron is expected to produce approximately 7 to 10 high threshold hits as it traverses the [TRT](#), and thus these hits provide a way to distinguish electrons from other charged particles.

The [TRT](#) contains 351,000 tubes in total, divided between the barrel and endcap regions. In the barrel region, the tubes are 144 cm long and arranged in 73 layers parallel to the beampipe. In the endcap region, the tubes are 37 cm long and arranged in 160 layers transverse to the beampipe. These configurations can be seen in Figure 20 and Figure 21. With this geometry the [TRT](#) achieves a resolution of $130\mu\text{m}$ in the $r - \phi$ direction.

1578 6.4 CALORIMETRY

1579 The combination of calorimeter systems used in [ATLAS](#) can measure the energy
 1580 of electrons, photons, hadrons, and hadronic jets with complete coverage up to
 1581 $|\eta| < 4.9$ and across ϕ . Unlike the inner detector, the calorimeters are capable
 1582 of measuring neutral particles. To accomplish precision measurements of these

1583 particle types, the [ATLAS](#) calorimeter system uses four individual calorimeters,
 1584 a [LAr](#) electromagnetic calorimeter in the barrel region, a tile hadronic calorime-
 1585 ter in the barrel region, a [LAr](#) hadronic endcap calorimeter, and a [LAr](#) forward
 1586 calorimeter. Together these provide hermetic coverage for the [ATLAS](#) detector.
 1587 The configuration of these calorimeters is illustrated in Figure 27. **Note: I could
 1588 make this section much longer. It might be nice to include a more com-
 1589 plete description of showers for example. I will extend this section if their
 1590 is space at the end.**

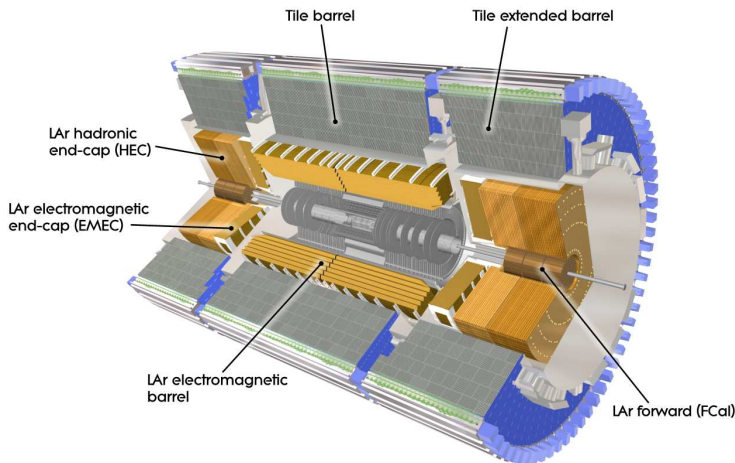


Figure 27

1591 The calorimeters are designed to absorb and measure the energy carried by
 1592 a particle, and completely stop the particle's propagation in the process. This
 1593 requires a significant amount of material to provide interactions. These interac-
 1594 tions then produce secondary particles, which can produce secondary particles
 1595 in turn, and thus form a cascade of particles called an electromagnetic ([EM](#)) or
 1596 hadronic shower, depending on the governing mechanism. Electromagnetic and
 1597 hadronic showers have very different properties and require different technolo-
 1598 gies to measure them accurately. All of the calorimeters in the [ATLAS](#) calorimeter
 1599 system are sampling calorimeters, that is they use alternating layers of absorbing
 1600 and active material. The dense absorbing layers initiate the showers while the ac-
 1601 tive layers measure the energy of the produced particles. A fraction of the energy
 1602 is lost in the inactive layers, so the energy measurement from the active layers
 1603 has to be corrected to estimate the actual energy of the particle.

1604 The [EM](#) calorimeter provides around 20 radiation lengths (X_0) while the hadronic
 1605 calorimeter provides around 10 interaction lengths (λ_0). As mentioned previ-
 1606 ously, radiation lengths measure the distance over which an electromagnetically
 1607 interacting particle loses a characteristic fraction of its energy. Interaction lengths,
 1608 on the other hand, measure the mean distance traveled by a hadronic particle be-
 1609 fore undergoing a nuclear interaction [10]. Figure 28 show the radiation lengths
 1610 in the layers of the [EM](#) calorimeter in the barrel region as well as the interaction
 1611 lengths for all calorimeters.

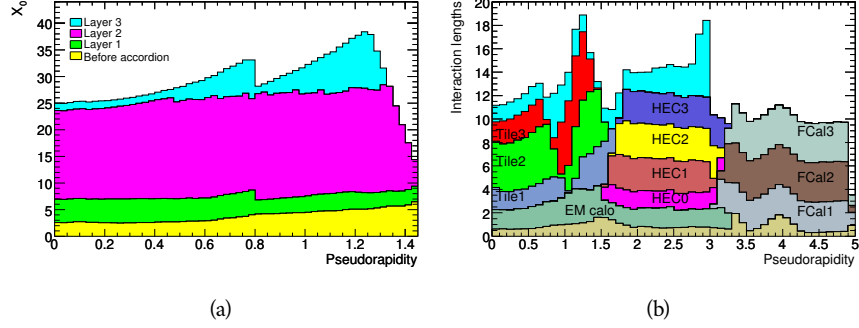


Figure 28: The depth of (a) the electromagnetic barrel calorimeter in radiation lengths and (b) all calorimeters in interaction lengths as a function of pseudorapidity.

1612 6.4.1 ELECTROMAGNETIC CALORIMETER

1613 The electromagnetic calorimeters use alternating layers of Liquid Argon and
 1614 lead in an accordion shape. The accordion shape allows a construction that pro-
 1615 vides complete coverage in the ϕ direction while also providing many alterna-
 1616 ting layers for the a particle to pass through. The configuration is detailed in
 1617 Figure 29. When an electron or photon passes through the lead, it produces an
 1618 electromagnetic shower. The particles produced in those showers then pass into
 1619 and ionize the Liquid Argon; the ions produced can then be collected by an elec-
 1620 trode in the Liquid Argon layer to provide the actual energy measurement.

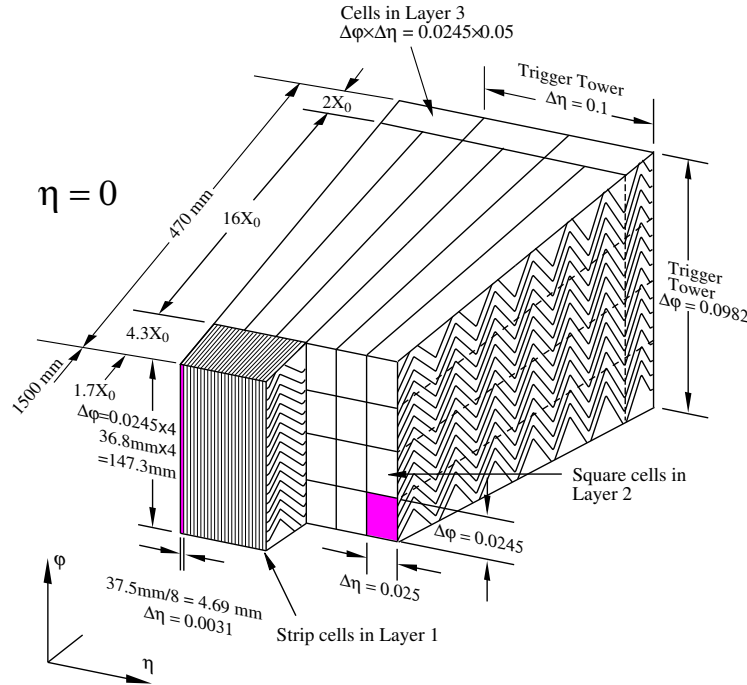


Figure 29: A schematic of the LAr calorimeter in the barrel region, highlighting the accordian structure.

The barrel region is covered by a presampler and three separate sampling layers with decreasing segmentation. The presampler is just a thin layer of Liquid Argon which measures the energy of any electromagnetic showers which are initiated before the particle reaches the calorimeter due to interactions with the detector material. The first layer is the strip layer, which has fine segmentation in η to enhance the identification of shower shapes and to provide a precise η measurement for reconstructing photons and electrons. The strip layer has only 4 radiation lengths worth of material, and has a segmentation of $\Delta\eta = 0.003$ and $\Delta\phi = 0.1$. The second layer is also finely segmented, with a segmentation of $\Delta\eta = 0.025$ and $\Delta\phi = 0.025$, and a thickness of $16 X_0$. This layer is designed to contain an electromagnetic shower and to measure the majority of the energy for photons and electrons. The third layer is only $2 X_0$ thick and measures the energy of electromagnetic showers which leak out of the second layer, and helps to separate electromagnetic showers from hadronic showers. The structure of the LAr endcap calorimeter is similar except that the layers are arranged parallel to the beampipe to measure energy deposits from high η particles.

6.4.2 HADRONIC CALORIMETERS

The hadronic calorimeters use a few different technologies to satisfy the resolution demands in the different areas of the detector, and together they cover the region $|\eta| < 2.7$. In the barrel region, for $|\eta| < 1.7$, the hadronic calorimeters are constructed of alternating tiles of steel and plastic scintillator. Like in the electromagnetic calorimeter, the dense layer initiates a shower (in this case the dense layer is the steel and the shower is hadronic) of particles which pass into and ionize the following layer. The ionization in the plastic scintillator instead produces a light signal proportional to the amount of ionization produced by the shower, and this signal is measured using photomultipliers and provides the actual energy measurement. The construction of a tile in the calorimeter is shown Figure 30, which highlights the alternating layers of steel and scintillator.

This tile calorimeter, as well as the remaining hadronic calorimeters, have a much coarser granularity than the electromagnetic calorimeters. The high granularity is not needed for an accurate energy measurement, and the hadronic calorimeters are not designed to distinguish particle types like the electromagnetic calorimeters. The tile granularity is approximately $\Delta\eta = 0.1$ and $\Delta\phi = 0.1$, and the segmentation in depth and η is shown in Figure 31.

The remaining hadronic calorimeters all use the same alternating, sampling structure but with different active and inactive materials. The hadronic endcap calorimeter covers the range of $1.5 < |\eta| < 3.2$ and uses an inactive layer of copper and an active layer of Liquid Argon. The forward calorimeter covers the range of $3.1 < |\eta| < 4.9$ and uses a dense matrix of copper and tungsten filled with Liquid Argon.

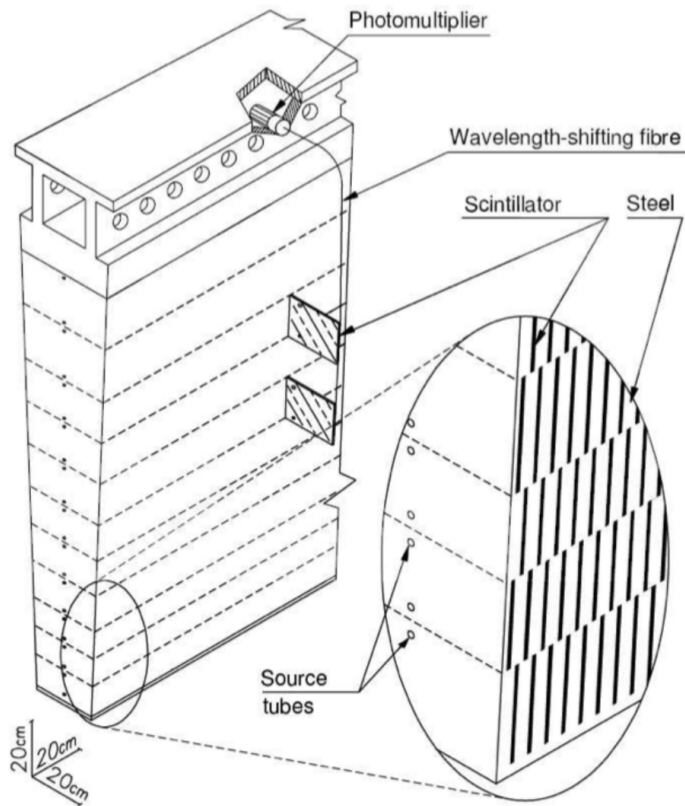


Figure 30: A schematic of a hadronic tile module which shows the alternating layers of steel and plastic scintillator.

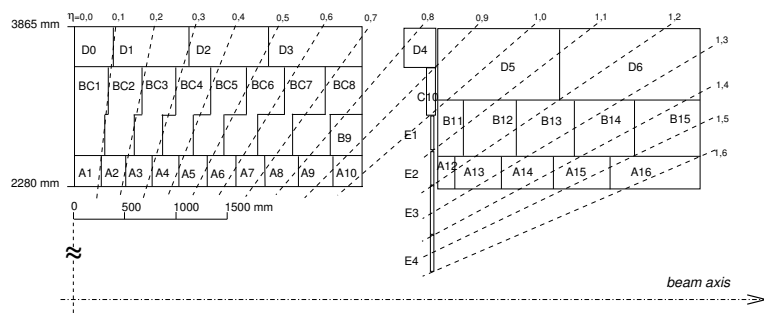


Figure 31: The segmentation in depth and η of the tile-calorimeter modules in the central (left) and extended (right) barrels.

1661 6.5 MUON SPECTROMETER

1662 Among SM particles, only muons and neutrinos consistently pass through the
 1663 calorimeters. Because the neutrinos are also electrically neutral, there is no fea-
 1664 sible option to measure them directly in ATLAS. The muons, on the other hand,
 1665 are charged and are thus already measured as a track in the inner detector. The
 1666 muon spectrometer provides a way to consistently identify muon tracks and also
 1667 a way to provide an additional measurement of their momentum.

1668 The muon spectrometer contains four subdetectors that cover the barrel and
 1669 endcap regions. In the barrel region, the muon spectrometer uses a combination
 1670 of Resistive Plate Chambers (RPCs) and MDTs to provide both a coarse, fast mea-
 1671 surement for triggering and a precise momentum measurement for offline event
 1672 reconstruction. Similarly, in the endcap region, the TGCs, MDTs, and CSCs allow
 1673 for both triggering and precise measurements. The CSCs are used only in the in-
 1674 nermost layer of the endcap region between $2.0 < |\eta| < 2.7$ where the particle
 1675 flux is too large for the MDTs to provide accurate measurements. The overall
 1676 layout of the muon systems are shown in the cut-away diagram in Figure 32,
 1677 and Figure 33 shows a precise schematic of the layout of each of the detecting
 1678 elements. The geometric arrangement shown provides consistent coverage for
 1679 muons produced up to $|\eta| < 2.7$, and takes full advantage of the bending of the
 1680 muons in the toroidal magnetic field, described in Section 6.2, to measure their
 1681 momentum. Figure 34 shows a cross-section of the arrangement of the muon
 1682 spectrometer in the barrel; the layers are divided into eight small and eight large
 1683 chambers that are overlapped to provide complete coverage in ϕ .

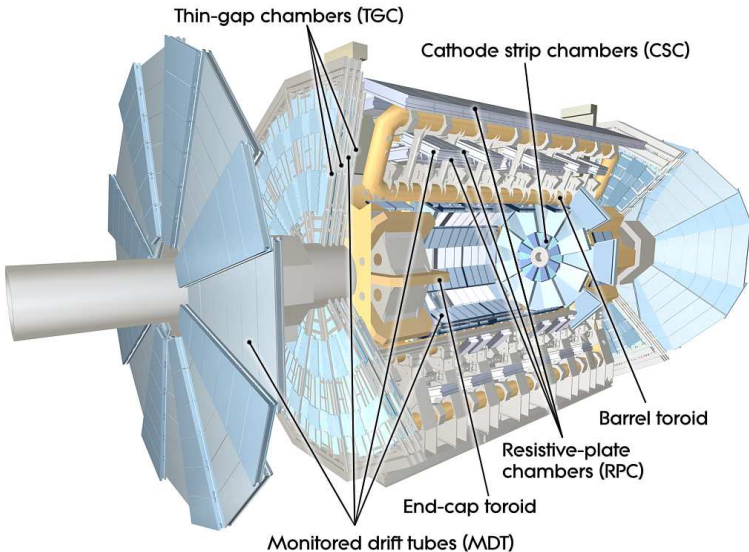


Figure 32: A cut-away diagram of the muon systems on ATLAS.

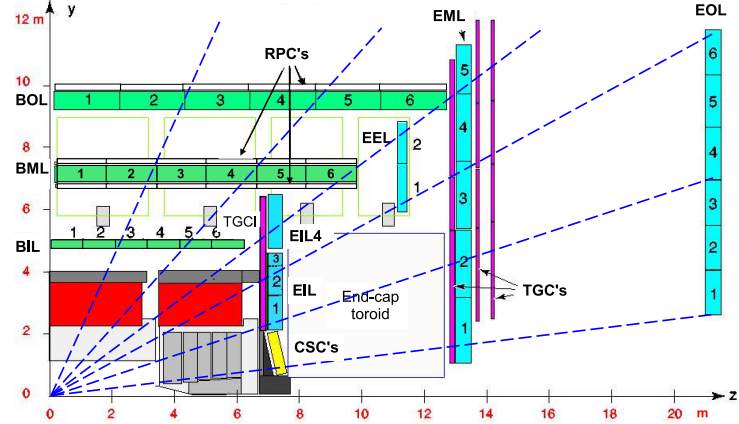


Figure 33: A quarter view of the muon spectrometer which highlights the layout of each of the detecting elements. The BOL, BML, BIL, EOL, EML, and EIL are all MDT elements, where the acronyms encode their positions.

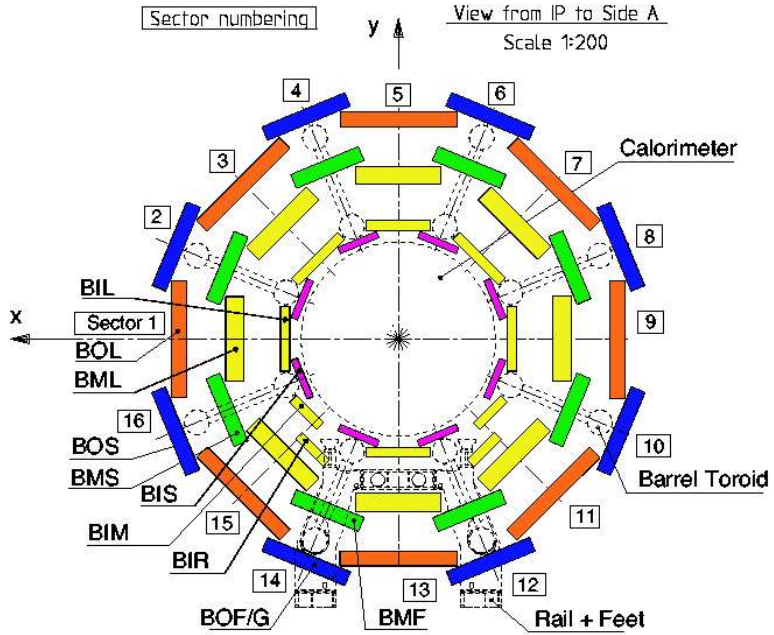


Figure 34: A schematic of the cross-section of the muon spectrometer in the barrel region.

1684 6.5.1 MONITORED DRIFT TUBE

1685 The momentum measurements in the barrel region are provided by three consecutive layers of MDT elements, located at approximately 5 m, 7 m, and 9 m from
 1686 the interaction point. Each of these layers is a composite of two multilayers of
 1687 drift tubes: two layers of three to four layers of tubes, as shown in Figure 35.
 1688 These aluminum tubes are 3 cm in diameter, with lengths between 0.9 and 6.2 m,
 1689 and are filled with a mixture of ArCO₂ kept at 3 bar absolute pressure. A central
 1690 tungsten-rhenium wire with a diameter of 50 μm runs along the length of the
 1691 tube, and is kept at a potential of 3080 V.

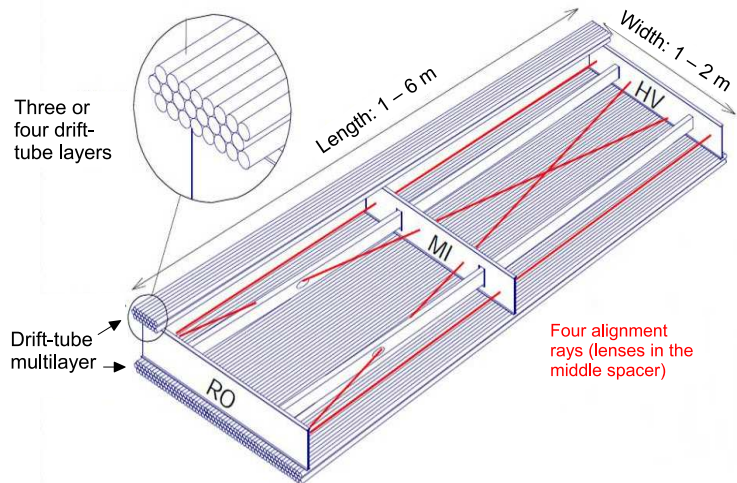


Figure 35: A schematic of a single MDT chamber, which shows the multilayers of drift tubes as well as the alignment system.

1693 A muon traversing these tubes ionizes the gas, and the ionization electrons
 1694 then drift in the electric field toward the central wire. Close to the wire, the
 1695 electric field is strong enough to cause the original ionization electrons to ionize
 1696 additional electrons, producing an avalanche that can be measured as a cur-
 1697 rent along the wire. The time of arrival of that current depends on how far the
 1698 muon entered from the wire, and can be used to achieve a position resolution of
 1699 80 μm in an individual tube. The combination of the measurements in the con-
 1700secutive layers of tubes improves this position resolution to 35 μm .

1701 To achieve a good resolution over the entire length of a muon track, the rel-
 1702 ative positions of the tubes of the muon spectrometer must be known to an ac-
 1703 curacy of 30 μm . This is achieved by an optical laser alignment system placed in
 1704 each of the individual chambers and throughout the cavern. These monitor any
 1705 changes in position or alignment due to effects like gravitational sag, tempera-
 1706 ture shifts, and the magnetic field. The configuration of the alignment system
 1707 within an individual chamber is also shown in Figure 34.

1708 6.5.2 RESISTIVE PLATE CHAMBER

1709 The **RPC** is the outermost detecting layer in the muon spectrometer in the barrel
 1710 region, and provides a fast measurement of the ϕ position of muons for trig-
 1711 gering. The speed of the measurement, with a time resolution of just a few
 1712 nanoseconds, requires a poor spatial resolution of approximately 1 cm. There
 1713 are three **RPCs** layers in the muon spectrometer, two located on either side of
 1714 the central **MDT** layer and one located outside the final **MDT** layer, as shown in
 1715 Figure 33. The **RPCs** consist of two layers of parallel plates filled with a gas mix-
 1716 ture of $C_2H_2F_4$. A muon passing through these systems ionizes the gas, like in
 1717 the **MDT**, which causes an avalanche of ionization electrons in the electric field
 1718 maintained between the plates. Metal strips on the outside of the chamber ca-
 1719 pacitively couple to the accumulated charge, and are read out to measure the η
 1720 and ϕ positions of the muon track.

1721 6.5.3 CATHODE STRIP CHAMBER

1722 The majority of the momentum measurements in the endcap region are provided
 1723 by the **MDTs**. In the most forward region of the muon spectrometer, between
 1724 $2.0 < \eta < 2.7$, the particle flux is very high due to contributions from low energy
 1725 photons and neutrons. The **MDT** can only sustain a hit rate of approximately 150
 1726 Hz/cm² because of limitations in the drift times of the gas and the capacity of
 1727 the readout electronics. The **CSCs** were designed to handle higher hit rates, up to
 1728 1000 Hz/cm², and provide the necessary coverage in that high flux region.

1729 The **CSC** consists of several multiwire proportional chambers, where the wires
 1730 are oriented in the radial direction out from the beampipe. There are eight large
 1731 and eight small chambers, arranged to partially overlap in the ϕ direction, as
 1732 shown in Figure 36. Like in the **MDT**, a muon traversing the system produces
 1733 ionization in the gas; here, however, the ionization is collected on a number of
 1734 wires. These wires couple to cathodes on the chambers which are segmented
 1735 into strips in two directions. The relative amount of charge on each of the neigh-
 1736 boring strips can be used to interpolate to the position of the muon in both η
 1737 and ϕ .

1738 6.5.4 THIN GAP CHAMBER

1739 Like in the barrel region, a separate, fast detector is required to provide position
 1740 measurements of muons for trigger in the endcap region. This is provided by
 1741 the **TGC** which consists of seven layers in the middle station of the endcap, two
 1742 doublet layers and one triplet layer, and a single doublet layer in the inner endcap
 1743 station. Figure 37 shows the arrangement of the triple and doublet layers of the
 1744 **TGCs**.

1745 Like the **CSCs**, the **TGCs** are multiwire proportional chambers with a wire-to-
 1746 cathode distance of 1.4 mm and a wire-to-wire distance of 1.8 mm. Readout
 1747 strips on the outside of the chambers run perpendicular to the wires, and couple
 1748 to the charge collected on the wires to provide a position measurement in the η

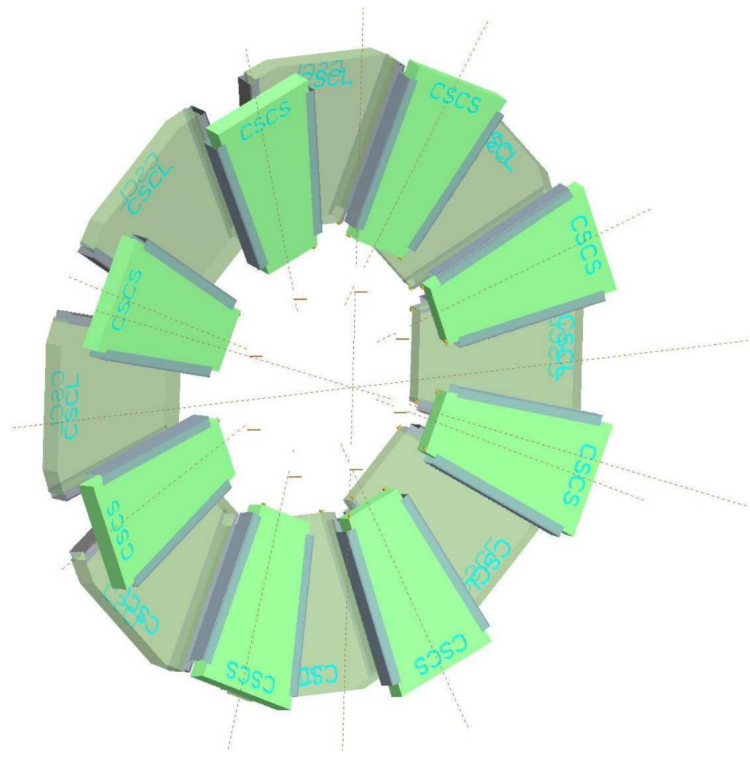


Figure 36: A schematic of the **CSC** endcap, showing the overlapping arrangement of the eight large and eight small chambers.

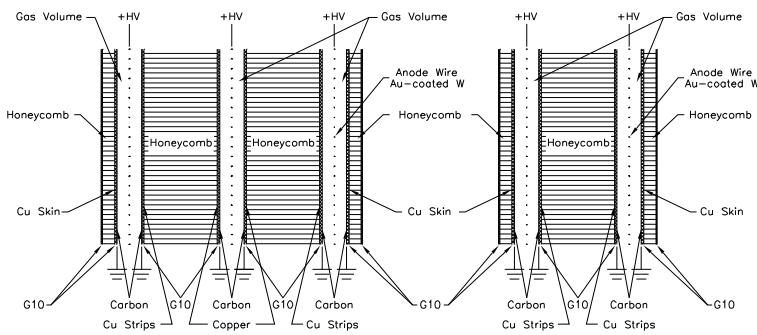


Figure 37: A schematic of the **TGC** doublet and triplet layers.

1749 direction. The current induced on the wires is also readout to provide a position
 1750 measurement in the ϕ direction. The high electric field and small wire-to-wire
 1751 distance give it the required good time resolution to be used for triggering events.

1752 6.6 TRIGGER

1753 It is not possible for the detector and the associated computing systems to record
 1754 the terabytes of data that the 40 MHz of proton-proton collisions produce every
 1755 second. Instead, a small fraction of these events are selected by the trigger sys-
 1756 tem to be recorded and later analyzed. Selecting interesting events at such a high
 1757 rate poses a significant challenge for the both the detector design and the imple-
 1758 mentation of a trigger decision and data acquisition system. The trigger must
 1759 balance the time needed to decide to keep an event, to avoid losing information,
 1760 with the filtering accuracy to consistently select a full menu of physics events
 1761 that can be used for the wide array of searches and measurements targeted by
 1762 [ATLAS](#).

1763 The [ATLAS](#) trigger system, as of Run 2, consists of two levels of decision mak-
 1764 ing. The first level, referred to as L1, is hardware based and uses inputs from
 1765 a subset of the detector elements to narrow the considered event rate from the
 1766 original 40 MHz down to 100 kHz. The 100 kHz rate is the maximal rate that
 1767 the event information can be transferred from the detector. The second level,
 1768 referred to as the [HLT](#), makes the final decisions on which events to keep for
 1769 analysis and selects a rate of around 1 kHz. The collection of selection criteria
 1770 used to make the L1 decisions feed into subsequent selection criteria in the [HLT](#),
 1771 and the set of these combinations of L1 and [HLT](#) criteria from the trigger menu
 1772 which defines exactly what events are recorded on [ATLAS](#). The entirety of the
 1773 trigger menu used for 2015 data collection is shown in Table 7, which summa-
 1774 rizes the selection requirements at both levels and additionally shows the peak
 1775 measured rates contributed by each.

1776 At L1, the trigger system uses information primarily from the calorimeters
 1777 and muon spectrometer to select high p_T jets, electrons, photons, and muons.
 1778 The electromagnetic calorimeter uses reduced granularity energy measurements
 1779 as well as isolation requirements to select electrons and photons. The hadronic
 1780 calorimeter also uses a combination of reduced granularity energy measurements
 1781 and isolation to select high momentum jets and hadronically decaying tau lept-
 1782 ons. The calorimeters are also used to provide triggers based on missing energy:
 1783 the coarse granularity energy measurements are used to calculate a directional
 1784 sum of energies and to trigger on a significant imbalance. Only the [RPCs](#) and [TGCs](#)
 1785 muon subdetectors contribute to the decision at L1, and are used to identify high
 1786 momentum muons. The contributions to the triggering rate of the various types
 1787 of L1 triggers are shown in Figure 38. The total rate is indicated in black and
 1788 is lower than the sum of individual rates because their is significant overlap be-
 1789 tween different trigger channels. The majority of the rate comes from lepton
 1790 and photon triggers.

1791 After an event is chosen by the L1 trigger, the detector measurements from the
 1792 bunch crossing which fired the trigger is read out from the front-end electronics

Trigger	Typical offline selection	Trigger Selection		Level-1 Peak Rate (kHz)	HLT Peak Rate (Hz)
		Level-1 (GeV)	HLT (GeV)	$L = 5 \times 10^{33} \text{ cm}^{-2}\text{s}^{-1}$	
Single leptons	Single iso μ , $p_T > 21$ GeV	15	20	7	130
	Single e , $p_T > 25$ GeV	20	24	18	139
	Single μ , $p_T > 42$ GeV	20	40	5	33
	Single τ , $p_T > 90$ GeV	60	80	2	41
Two leptons	Two μ 's, each $p_T > 11$ GeV	2×10	2×10	0.8	19
	Two μ 's, $p_T > 19, 10$ GeV	15	18, 8	7	18
	Two loose e 's, each $p_T > 15$ GeV	2×10	2×12	10	5
	One e & one μ , $p_T > 10, 26$ GeV	$20 (\mu)$	7, 24	5	1
	One loose e & one μ , $p_T > 19, 15$ GeV	15, 10	17, 14	0.4	2
	Two τ 's, $p_T > 40, 30$ GeV	20, 12	35, 25	2	22
	One τ , one μ , $p_T > 30, 15$ GeV	12, 10 (+jets)	25, 14	0.5	10
	One τ , one e , $p_T > 30, 19$ GeV	12, 15 (+jets)	25, 17	1	3.9
Three leptons	Three loose e 's, $p_T > 19, 11, 11$ GeV	15, 2 \times 7	17, 2 \times 9	3	< 0.1
	Three μ 's, each $p_T > 8$ GeV	3 \times 6	3 \times 6	< 0.1	4
	Three μ 's, $p_T > 19, 2 \times 6$ GeV	15	18, 2 \times 4	7	2
	Two μ 's & one e , $p_T > 2 \times 11, 14$ GeV	$2 \times 10 (\mu's)$	$2 \times 10, 12$	0.8	0.2
	Two loose e 's & one μ , $p_T > 2 \times 11, 11$ GeV	2 \times 8, 10	2 \times 12, 10	0.3	< 0.1
One photon	one γ , $p_T > 125$ GeV	22	120	8	20
Two photons	Two loose γ 's, $p_T > 40, 30$ GeV	2×15	35, 25	1.5	12
	Two tight γ 's, $p_T > 25, 25$ GeV	2×15	2×20	1.5	7
Single jet	Jet ($R = 0.4$), $p_T > 400$ GeV	100	360	0.9	18
	Jet ($R = 1.0$), $p_T > 400$ GeV	100	360	0.9	23
E_T^{miss}	$E_T^{\text{miss}} > 180$ GeV	50	70	0.7	55
Multi-jets	Four jets, each $p_T > 95$ GeV	3×40	4×85	0.3	20
	Five jets, each $p_T > 70$ GeV	4×20	5×60	0.4	15
	Six jets, each $p_T > 55$ GeV	4×15	6×45	1.0	12
b -jets	One loose b , $p_T > 235$ GeV	100	225	0.9	35
	Two medium b 's, $p_T > 160, 60$ GeV	100	150, 50	0.9	9
	One b & three jets, each $p_T > 75$ GeV	3×25	4×65	0.9	11
	Two b & two jets, each $p_T > 45$ GeV	3×25	4×35	0.9	9
b -physics	Two μ 's, $p_T > 6, 4$ GeV plus dedicated b -physics selections	6, 4	6, 4	8	52
Total				70	1400

Table 7: The trigger menu for the 2015 data collection with $L = 5 \times 10^{33} \text{ cm}^{-2}\text{s}^{-1}$. Both the L1 and HLT selection requirements and their trigger rates are shown measured at the specified luminosity are shown. The typical offline selections represent a typical set of offline requirements imposed after the trigger in an analysis.

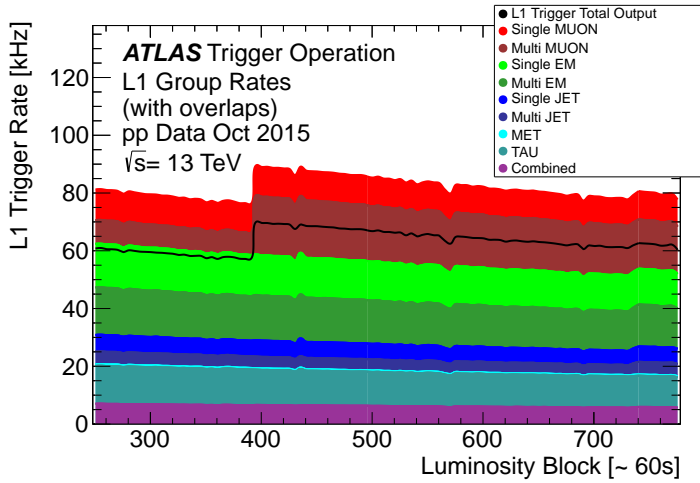


Figure 38: The L1 Trigger rate broken down into the types of triggers as a function of the luminosity block for the 2015 data collection period.

1793 and stored on read-out boards. This inclusive information is necessary to make
 1794 more the more precise event selections than is possible with the reduced infor-
 1795 mation at L1. The **HLT** then uses this information with software algorithms to
 1796 decide whether or not to permanently record the event. The L1 trigger also for-
 1797 wards which decision was made and Region of Interests (**RoIs**) to the **HLT**, which
 1798 allows the **HLT** to focus on particular algorithms and particular sections of the
 1799 detector to greatly improve the algorithmic selection speed. The additional in-
 1800 formation available to the **HLT** allows it to implement additional trigger targets,
 1801 such as identified jets from the decays of b-hadrons. The contributions to the
 1802 triggering rate of the various types of **HLT** triggers are shown in Figure 39.

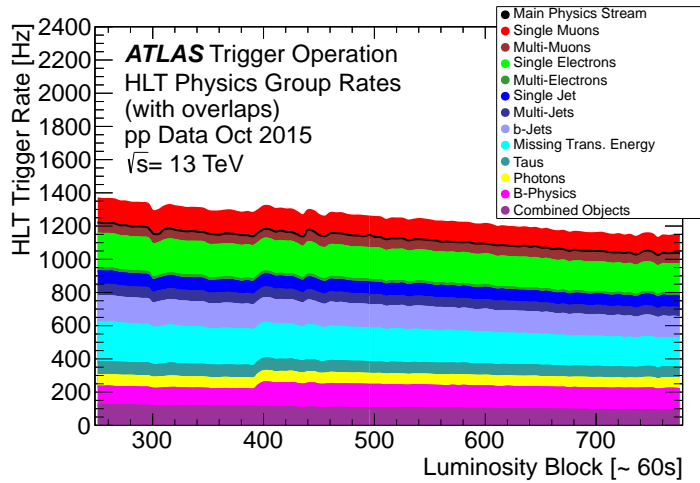


Figure 39: The HLT Trigger rate broken down into the types of triggers as a function of the luminosity block for the 2015 data collection period.

1803

1804 EVENT RECONSTRUCTION

1805 The ATLAS experiment combines measurements in the subdetectors to form a
 1806 cohesive picture of each physics event. The majority of particles that traverse
 1807 the detector leave behind some combination of ionization hits in the tracking
 1808 detectors or energy deposits in the calorimeters, and these measurements can
 1809 be used to reconstruct physical quantities like the particle's energy, momentum,
 1810 or trajectory. Even the type of the particle can be distinguished by comparing
 1811 the various ways that different species of stable particles interact with the subde-
 1812 tectors. Reconstruction is the process which takes the electronic outputs of the
 1813 detector and collects them into individual physics objects. The physics objects
 1814 summarize the properties of particles produced by the collision or subsequent
 1815 decays, either for individual isolated particles like leptons, or for a collection of
 1816 the cascade of products produced in the decay of an energetic hadron, called a
 1817 jet. These are the objects and quantities most often used in analysis to make
 1818 measurements of SM processes or to search for new physics.

1819 7.1 TRACKS AND VERTICES

1820 As described in Section 6.3, charged particles that traverse the inner detector
 1821 leave behind hits in the subdetectors. Each of these hits translates into a position
 1822 measurement along the trajectory of that particle, with position resolutions de-
 1823 pending on the subdetector that provided the measurement. Track reconstruc-
 1824 tion uses these position measurements to cluster hits in consecutive layers of
 1825 the detector into a trajectory consistent with a particle curving in a magnetic
 1826 field [13, 14]. The number of hits in the inner detector for each event makes
 1827 a combinatorial method completely infeasible: the algorithms that form tracks
 1828 must be significantly more intelligent so that event reconstruction does not ex-
 1829 haust computing resources.

1830 The first and primary algorithm employed in track reconstruction is called
 1831 the inside-out method, which begins with the assumption that the track orig-
 1832 inated from the interaction point. Its purpose is to identify primary particles,
 1833 those which originate in the proton-proton collisions and with a lifetime long
 1834 enough to reach the inner detector. Combinations of three space points are con-
 1835 sidered from measurements in the Pixel detector and the first layer of the SCT,
 1836 and form the seed for a track. The seed is then extrapolated into the SCT and
 1837 hits in each layer are considered to be added to the track using a combinatorial
 1838 Kalman filter [14]. After all of the SCT layers have been considered, tracks are
 1839 filtered to reduce ambiguities from other nearby tracks or from combinatorial
 1840 coincidences. Then the tracks are extended into the TRT in the same way. This
 1841 algorithm is how the hits are chosen to be incorporated into a single track. Once
 1842 the hits are collected, a fitting algorithm calculates the track parameters which

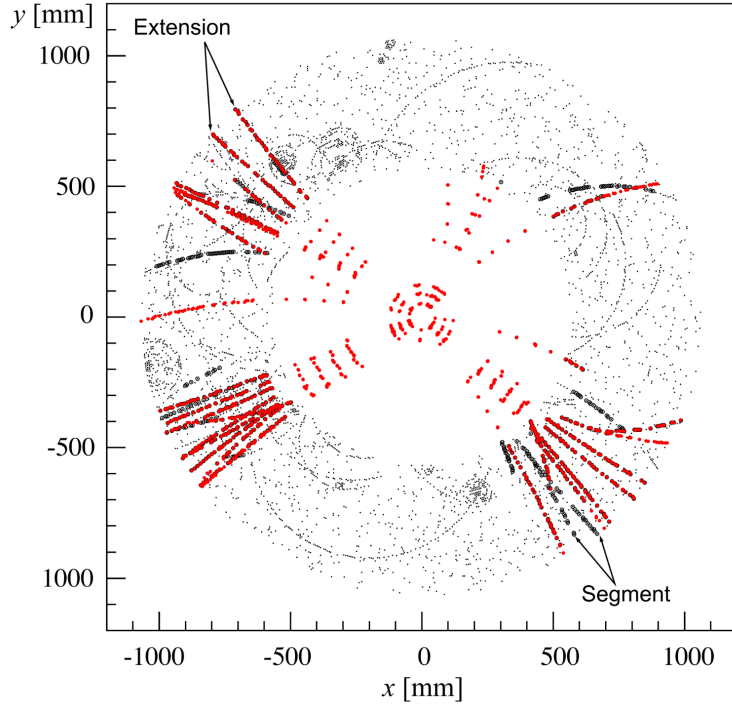


Figure 40: The x and y locations of the hits generated in a simulated $t\bar{t}$ event in the inner detector. The hits which belong to tracks formed using the inside-out algorithm are highlighted in red, while the hits which belong to tracks formed using the outside-in algorithm are circled in black.

1843 best model the locations of the hits and their resolutions. Those parameters di-
 1844 rectly determine the direction and momentum of the particle which produced
 1845 the track.

1846 This inside-out algorithm is complemented by an outside-in algorithm, which
 1847 is used to find tracks from secondary particles, those produced in the decays or
 1848 interactions of the primary particles inside the detector. As the name indicates,
 1849 the outside-in algorithm begins by seeding tracks in the outermost layers of the
 1850 inner detector, in the [TRT](#). The seed in this case is formed by a segment in the
 1851 [TRT](#), and the track is propagated backwards into the [SCT](#) before being refitted
 1852 to use all the included points. Some tracks are found with [TRT](#) segments only,
 1853 which can result from interactions with the detector following the [SCT](#). Figure 40
 1854 shows an example of the geometry of tracks formed by both algorithms, where
 1855 the hits belonging to tracks found using the inside-out algorithm are highlighted
 1856 in red, and the hits belonging to the tracks found using the outside-in algorithm
 1857 are circled in black. The figure highlights the presence of a large number of
 1858 both primary and secondary tracks in a single event, as well as the overall large
 1859 number of hits present in the inner detector.

1860 The tracks resulting from these algorithms can be contaminated by nearby
 1861 particles confusing the tracking algorithm in a high luminosity environment.
 1862 For example, enough hits present in the inner detector can lead to fake tracks
 1863 from combinations of hits from multiple individual tracks. Therefore, after the
 1864 tracks are formed and fitted, additional quality requirements are imposed in

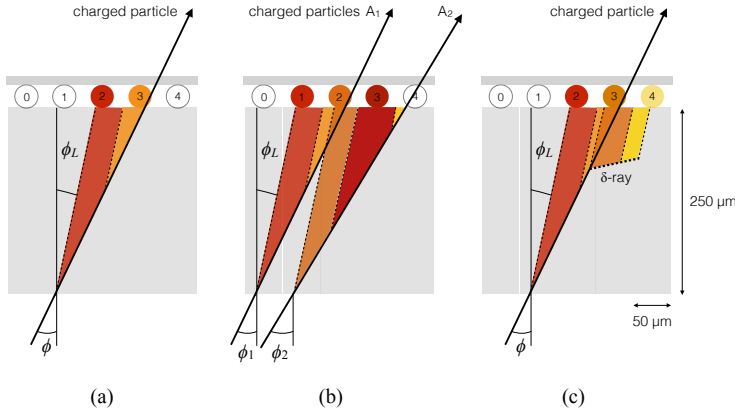


Figure 41: Examples of the clusters formed in a single layer of the pixel detector for (a) a single isolated particle, (b) two nearly-overlapping particles, and (c) a particle which emits a δ -ray [15].

order to reduce such backgrounds. Most tracking applications require at least seven silicon hits, that is, seven hits between the Pixel detector and [SCT](#). Then the tracks are required to have at most two holes in the Pixel detector, where holes are non-existing but expected measurements in a layer of the subdetector. If the missing hit corresponds to an inactive module, however, it is not counted as a hole but instead as a hit for tracking as the lack of a measurement is expected in that case.

7.1.1 PIXEL NEURAL NETWORK

The hits in the Pixel detector are not typically confined to a single pixel, but rather the charge is spread over several pixels per layer which are grouped together into clusters. The clustering of these pixels for isolated tracks is relatively straightforward, but complications can arise in the high track density environment where hits from multiple particles can overlap in a single cluster. Figure 41 shows examples of clusters generated by a single isolated particle, two nearly overlapping particles, and a particle which emits a δ -ray. A δ -ray is a secondary electron which is generated with enough energy to escape a significant distance away from the original particle and to generate additional ionization.

A series of neural-networks analyzes the shape of the clusters to determine how many particles produced the cluster and to find the positions of each of the particles within the cluster. These allow for an identification of clusters caused by more than one particle or by a particle that emits a δ -ray. In a high-density tracking environment, the multiple position outputs can be used as the locations of individual hits to allow reconstruction of tracks which almost overlap and with a much better separation than is possible without the splitting of individual clusters.

1890 7.1.2 PIXEL DE/DX

1891 A hit in the Pixel detector corresponds to the voltage generated from ionization
 1892 current rising above a threshold value that is tuned to consistently record the
 1893 passing of MIPs. A larger amount of charge deposited results in a larger voltage,
 1894 and a larger signal remains above the threshold for a longer period of time. The
 1895 time over threshold (`ToT`) is read out of the Pixel detector, and can be used to
 1896 provide a measurement of the charge deposited in each pixel. The charge mea-
 1897 surements from each of the pixels included in a pixel cluster are summed to form
 1898 one charge measurement per layer of the pixel detector. That charge measure-
 1899 ment, combined with the angle of incidence of the track and the known sizes of
 1900 each detector element, can be converted into a measurement of dE/dx , the ion-
 1901ization energy deposited per unit distance, measured in $\text{MeVg}^{-1}\text{cm}^2$. The IBL
 1902 only has sixteen available values (4 bits) of `ToT` to readout, compared to the 256
 1903 available values (8 bits) in the remaining pixel layers. To help alleviate this lack
 1904 of range, the IBL also records if it is in overflow: when the ionization is sufficient
 1905 to generate a `ToT` above the largest value that can be recorded in the 4 bits.

1906 The measurements across multiple layers are combined to form an average
 1907 value of dE/dx for the track as a whole. To reduce the influence of the typical
 1908 long Landau tails of the distribution of dE/dx deposits [10], the average is cal-
 1909 culated as a truncated mean. The value measured in the IBL is removed if it is
 1910 in overflow, as the measured value is not reliable in that case. If a track has five
 1911 measurements in the pixel detector, the two highest cluster values are removed.
 1912 If a track has two, three, or four measurements in the pixel detector, only the
 1913 single highest cluster value is removed. The remaining values are averaged to
 1914 form the pixel dE/dx .

1915 7.1.3 VERTEX RECONSTRUCTION

1916 A vertex represents the intersection of multiple tracks and corresponds to the
 1917 location of an interaction. If at least two charged particles result from the in-
 1918 teraction, the intersection of their resulting tracks reveals its position with high
 1919 precision. Vertices are divided into two groups, primary vertices which corre-
 1920 spond to the actual proton-proton collisions, and secondary vertices which cor-
 1921 respond to decays of short-lived particles or interactions with the detector. Pri-
 1922 mary vertices are particularly important, as they can provide a precise location
 1923 for the interaction which generated the observed particles. Understanding that
 1924 location is crucial in understanding the geometry of the event.

1925 Primary vertices are reconstructed by iteratively identifying seeds from re-
 1926 constructed tracks. Each track's extrapolated z position at the beamline forms a
 1927 seed, and nearby tracks are fitted using that position as a point along their trajec-
 1928 tory. The goodness of fit with that vertex is considered for each track, measured
 1929 in χ^2 . The final position of the vertex is determined by a fit to all of the con-
 1930 sidered tracks, where the contribution from each track is weighted according to
 1931 the χ^2 compatibility with that vertex. Any tracks from this procedure that are
 1932 displaced by more than 7σ from that vertex are removed from the fit and used

1933 to seed a new vertex. This procedure is iterated until no additional vertices can
 1934 be found.

1935 This procedure is typically performed twice. The first set of vertices is used
 1936 to fit a profile for the beamspot, which indicates the position of the intersection
 1937 of beams in that particular bunch crossing. The fitted beamspot then provides
 1938 a constraint for the second attempt to locate primary vertices, where both the
 1939 track fitting and seeding of vertices are required to be consistent with interac-
 1940 tions occurring within the beamspot.

1941 7.2 ELECTRONS AND PHOTONS

1942 Electrons are measured as both a charged particle track and energy deposits in
 1943 the electromagnetic calorimeter. Photons, on the other hand, leave energy de-
 1944 posits in the electromagnetic calorimeter but do not produce a corresponding
 1945 track. Because the electromagnetic interactions with the calorimeter of both
 1946 photons and electrons produces more photons and electrons, the behavior in the
 1947 calorimeter is very similar and there is significant overlap in the reconstruction
 1948 techniques for each.

1949 The reconstruction of a photon or an electron in the calorimeter is based on
 1950 clustering algorithms which identify groups of energy deposits [16]. For this
 1951 purpose, the entire electromagnetic calorimeter is subdivided into a grid of 200
 1952 by 256 towers in the η and ϕ directions, respectively, where the individual grid
 1953 units have a size of $\Delta\eta = 0.025$ and $\Delta\phi = 0.025$. These towers correspond to
 1954 individual cells in the middle, coarsest layer of the EM calorimeter, and in the
 1955 remaining layers the cells are grouped together cover the same area in $\eta - \phi$
 1956 space. The clustering begins by finding seeds with a sliding-window algorithm
 1957 based on the towers: a window of 3 by 5 towers is formed and translated until
 1958 the sum of the energy within the window is maximized. If that energy is above
 1959 2.5 GeV, then that region becomes a seed. The choice of 2.5 GeV was chosen to
 1960 compromise between maximizing reconstruction efficiency while minimizing
 1961 fake electron seeds from electronic noise or pileup. The seeds are rejected if the
 1962 energy measured in the hadronic calorimeter behind the seed is large, as this
 1963 typically indicates a hadron rather than an electron or photon.

1964 Next, the inner detector tracks within a cone of $\Delta R = 0.3$ are compared to
 1965 the location and energy of the seed. Tracks are matched to the cluster if the ex-
 1966 trapolation of the track to the energy-weighted center in the middle layer of the
 1967 EM calorimeter falls within $\Delta\phi < 0.2$ in the direction of the curvature of the
 1968 track or $\Delta\phi < 0.05$ in the direction opposite of the curvature of the track. If the
 1969 seed matches with a track that originated from a primary vertex, the combina-
 1970 tion of track and electromagnetic cluster is reconstructed as an electron. If the
 1971 seed matches with a track that did not originate from a primary vertex, then the
 1972 electromagnetic cluster is reconstructed as a converted photon. And if there is
 1973 no corresponding track in the inner detector, then the cluster is reconstructed
 1974 as a photon.

1975 After classification, the final clustering of the energy in the EM calorimeter
 1976 calorimeter is performed. The classification must be done first, as the expected

1977 size of the energy deposits in the calorimeter are different for electrons and photons.
 1978 In the barrel region, the final clusters for electrons are formed in rectangles
 1979 of 3 towers in the η -direction and 7 towers in the ϕ -direction. This asymmetric
 1980 window accounts for the curving of the produced charged particles only in the
 1981 ϕ direction. For photons, the size of the rectangle is 3 towers by 5 towers. In the
 1982 endcap region, all object types are clustered in rectangles of 5 towers by 5 tow-
 1983 ers, as the effect of the magnetic field curvature is less pronounced in this region.
 1984 The sum of the energies in these clusters provide the final energy measurement
 1985 for the electron or photon.

1986 7.2.1 PHOTON IDENTIFICATION

1987 The original requirement for constructing a photon cluster, a significant energy
 1988 deposit in the electromagnetic calorimeter without a corresponding track or en-
 1989 ergy deposits in the hadronic calorimeter, is already effective in identifying pho-
 1990 tons. However, there is a significant background for prompt photon production
 1991 from the decays of pions, $\pi^0 \rightarrow \gamma\gamma$. These can be identified using the shape of
 1992 the cluster in the narrow η granularity in the first layer of the [EM](#) calorimeter.

1993 7.2.2 ELECTRON IDENTIFICATION

1994 Prompt electrons have a number of backgrounds, such as secondary electrons
 1995 from hadron decays or misidentified hadronic jets, that can be rejected using ad-
 1996 ditional information from the [EM](#) calorimeter and the inner detector. The most
 1997 basic level of electron identification, referred to as Loose, makes requirements
 1998 on the shower shapes in the high granularity first layer of the [EM](#) calorimeter
 1999 as well as the quality of the inner detector track. It also requires a good match
 2000 between the track and the calorimeter energy deposits and a small fraction of
 2001 energy in the hadronic calorimeter behind the electromagnetic cluster. [ATLAS](#)
 2002 defines several additional working points, including Medium and Tight, which
 2003 provide progressively lower background rates for electrons by imposing addi-
 2004 tionally strict requirements on the above variables as well as new requirements
 2005 like the impact parameter of the inner detector track or the comparison of the
 2006 cluster energy to the momentum in the inner detector.

2007 7.3 MUONS

2008 Muons produced in [ATLAS](#) first traverse the inner detector and leave behind a
 2009 track as described in Section 7.1. The muon then passes through the calorimeter,
 2010 leaving behind a small, characteristic amount of energy, and then passes through
 2011 the muon spectrometer where it produces hits in the [MDTs](#) or [CSCs](#). Muon tracks
 2012 are formed from local segments of hits in each layer of the [MDTs](#) or [CSCs](#), and
 2013 then the final muon spectrometer track is formed by combining the two local
 2014 segments. When a track is reconstructed in both the inner detector and the muon
 2015 spectrometer, they are combined to form a combined muon.

2016 In a few regions of the detector, a muon may fail to leave behind both a com-
 2017 plete inner detector and muon system track. For a very small fraction of the
 2018 acceptance of the muon system, there is only one layer of muon chambers and a
 2019 global muon system track is not formed. In this case, as long as the track in the
 2020 inner detector exists and geometrically matches to a segment, a segment-tagged
 2021 muon is formed using momentum measurements from the inner detector. In
 2022 the region where the muon system has coverage but the inner detector does not,
 2023 $2.5 < |\eta| < 2.7$, a stand-alone muon is formed which uses only information
 2024 from the muon system. And for muons produced within one of the few holes in
 2025 the muon system, including $|\eta| < 0.1$, the characteristic energy deposits in the
 2026 calorimeter can be used to tag an inner detector track as a calo-tag muon. These
 2027 additional categories are used to achieve high efficiency over a larger range of
 2028 acceptance, but the combined muons are the most reliable.

2029 7.3.1 MUON IDENTIFICATION

2030 The various types of muons are incorporated into three working points: Loose,
 2031 Medium, and Tight, which reflect the increasing muon purity for each of the
 2032 selections definitions. Tight muons include only combined muons with a good
 2033 track fit quality and momentum resolution and at least two hits in a precision
 2034 muon system layer. Medium muons include those in tight as well as combined
 2035 muons with one precision hit and one precision hole, where hole is defined in
 2036 the same way as in Section 7.1. The medium working point also includes stand-
 2037 alone muons with $|\eta| > 2.5$ and at least two hits in precision layers. And finally
 2038 the loose working point includes both medium and tight muons, but additional
 2039 includes segment-tagged and calo-tagged muons in the region $|\eta| < 0.1$.

2040 7.4 JETS

2041 A jet does not directly correspond to a physical particle, unlike all of the recon-
 2042 structed objects described above, but instead tries to capture the conical cascade
 2043 of particles produced in the hadronization of a quark or gluon from the proton-
 2044 proton collision. The hadronization process creates a very large number of col-
 2045 limated particles, with a high enough density that individually reconstructing all
 2046 of the produced particles in the calorimeter is not possible within ATLAS. How-
 2047 ever most analyses are interested only in the kinematics of the particle which
 2048 produced the cascade, rather than the individual products. Therefore, jets are
 2049 a useful tool to measure the combined energy and direction of the ensemble of
 2050 products and thus represents the kinematics of the original. Jet algorithms are
 2051 very generic and can be used to group together a number of types of objects to
 2052 form aggregate representations. For example, truth particles in simulation can
 2053 be grouped in truth jets, or tracks from the inner detector can be grouped to-
 2054 gether to form track jets. This section, however, will focus on calorimeter jets
 2055 which take topoclusters of energy deposits in the calorimeter as inputs and pro-
 2056 duce a combined object which represents the energy measured by the calorime-
 2057 ter and the location where it was deposited.

2058 74.1 TOPOLOGICAL CLUSTERING

2059 Hadrons often deposit their energy into multiple individual cells in both the elec-
 2060 tromagnetic and hadronic calorimeters. The purpose of topological clustering is
 2061 to group cells in all three dimensions into clusters that represent a single energy
 2062 deposit. The procedure must be robust enough to reject noise fluctuations in
 2063 the cell energy measurements that can come from both electronic noise and ad-
 2064 dditional low energy particles produced in pileup activity. The background level
 2065 of calorimeter noise is called σ_{noise} , and is an important component of the topo-
 2066 logical clustering.

2067 The topological clusters are formed in a three step process called the 4-2-0
 2068 threshold scheme, which uses three energy thresholds to build up a cluster from
 2069 cells. First, any cells with a measured energy above $4\sigma_{\text{noise}}$ are identified as seed
 2070 cells. The cells adjacent to the seed cells with a measured energy above $2\sigma_{\text{noise}}$ are
 2071 called secondary cells. All of the cells which are adjacent to a secondary cell
 2072 with $E_{\text{cell}} > 2\sigma_{\text{noise}}$ are also labelled secondary cells. Tertiary cells are those
 2073 immediately adjacent to a seed or secondary cell with a measured energy above
 2074 zero. Adjacency in this sense is defined in three dimensions, cells are adjacent if
 2075 they are neighbors within a layer but also if they have the same $\eta - \phi$ coordinates
 2076 but are in adjacent layers or even in an adjacent layer in another calorimeter.

2077 From these definitions, clusters are built by resolving the seeds in order of
 2078 significance, the ratio $E_{\text{cell}}/\sigma_{\text{noise}}$. All adjacent secondary cells to the highest
 2079 significance seed are added to that seed's topocluster, and any of those cells which
 2080 would also have qualified as seeds are removed from the list of seeds. Once all
 2081 of the secondary cells have been added, the tertiary cells are then added to that
 2082 cluster as well. This procedure is then iterated until no seeds remain, forming
 2083 the first round of topoclusters.

2084 It is also useful to split topoclusters into multiples if local maxima are present
 2085 within the topocluster, as clusters produced by multiple nearby particles can
 2086 merge. The splitting process begins by finding local maxima cells in the middle
 2087 layer of the calorimeters with a minimum energy of 500 MeV and at least four
 2088 neighboring secondary cells. These requirements reduce the likelihood to split
 2089 a cluster due to random fluctuations, as the middle layers provide the most reli-
 2090 able energy measurements. Cells between two local maxima can then be shared
 2091 between two clusters to account for overlapping contributions from two parti-
 2092 cles. The energy sharing is weighted by the energy of each cluster as well as the
 2093 distance of the cell to the centroid of that cluster.

2094 The energies of all the cells in the cluster are then summed together to form
 2095 the energy of that cluster. The energy needs to be corrected for the various losses
 2096 expected in the calorimeter, as described in Section 6.4. The simplest correction,
 2097 scaling the measured energy by the sampling fraction, brings the cluster energies
 2098 to the EM scale. It is called the EM scale because it accurately describes the energy
 2099 of electromagnetic showers.

2100 Another scale is defined to improve accuracy for hadronic processes, the local
 2101 cluster weighted (LCW) scale, that helps to correct for the expected variations in
 2102 hadronic energy deposits. The LCW correction first determines if the shower is

hadronic or electromagnetic, based on the depth of the shower and the cluster energy density. For hadronic showers, the energy is corrected for calorimeter non-compensation, an effect which reduces the measured energy of hadronic showers because some of the energy goes into invisible processes like the break up of nuclei. All clusters are then corrected for energy that may be deposited in uninstrumented regions in that cluster's location in the calorimeter, and they are also corrected with an estimate of how much energy falls outside the extent of the cluster based on its shape and the deposit type.

7.4.2 JET ALGORITHMS

Using the topological clusters as inputs, a jet algorithm groups them together into a collection of adjacent energy deposits that is intended to correspond to a single process. Jet algorithms need a few key characteristics to be usable for physics analysis. First, the jets produced by the algorithm should have little dependence on the addition of soft particles to the event (infrared safety), as a negligible addition of energy should not significantly modify the event topology. Similarly, the jets produced by the algorithm should also not significantly depend on mostly collinear splitting of an input particle (collinear safety); that is, a single quark splitting into two nearly parallel quarks should not change the resulting jets, which are intended to capture only the properties of the aggregate and not those of individual particles. And finally the algorithm needs to be sufficiently simple and fast to be used for the large rate of collected proton-proton collisions on [ATLAS](#).

The most commonly used algorithm on [ATLAS](#) that satisfies these requirements is called the anti- k_t algorithm, and is discussed in further detail in Reference [17]. The anti- k_t , in brief, relies on iteratively combining the input objects that are closest together, where closest is defined by a particular distance metric, d_{ij} . The combinations stop when the closest remaining object is the beam itself, where the distance to the beam is called $d_{i,B}$. An entire class of algorithms follows this procedure with the following distance metrics

$$d_{ij} = \min(k_{ti}^{2p}, k_{tj}^{2p}) \frac{\Delta_{ij}^2}{R^2} \quad (18)$$

$$d_{i,B} = k_{ti}^{2p} \quad (19)$$

where $\Delta_{ij} = (y_i - y_j)^2 + (\phi_i - \phi_j)^2$, k_{ti} is the transverse momentum of the object, y is the rapidity, and p is a parameter of the algorithm. Anti- k_t is the particular case where $p = -1$, and is a choice that results in an algorithm that is both infrared and collinear safe.

The algorithm is repeated until there are no input objects remaining, which results in a series of jets. Each jet has a complete four momentum from the combination of its input clusters. The jet energies then need to be calibrated to attempt to match the energy of the object which produced the jet.

2140 74.3 JET ENERGY SCALE

2141 Though the [LCW](#) scheme attempts to correct the topoclusters to reflect the true
 2142 deposited energy, the correction does not fully account for energy lost within
 2143 the calorimeters. Because of these effects, the original reconstructed jet energy
 2144 does not reflect the true energy of the particle which initiated the jet. Therefore
 2145 it is necessary to additionally correct the reconstructed jet itself, in addition to
 2146 the corrections on the inputs. This correction is referred to as the [JES](#), which
 2147 combines several individual steps of calibration.

2148 The first calibration step corrections the direction of the jet to ensure that it
 2149 points back to the primary vertex. Next, the energy of the jet is corrected for
 2150 pileup by subtracting the expected contribution from pileup (measured in simu-
 2151 lation) based on the momentum, η , and area of the jet as well as the number of
 2152 reconstructed vertices and expected number of interactions per crossing. The
 2153 largest single correction is the absolute η and [JES](#) correction, where the jet energy
 2154 and pseudorapidity is corrected to attempt to match the energy and pseudorapid-
 2155 ity of the parton which produced it. This correction is measured in simulation
 2156 by comparing the reconstructed jet energies to the energy of the truth particle
 2157 which produced it. However the simulation is not relied on alone to estimate
 2158 this correction, and an additional step applies an additional energy correction
 2159 based on in-situ measurements in data. These corrections come from various
 2160 techniques which measure jet energies indirectly by balancing them with other,
 2161 well-measured objects. In the central region ($|\eta| < 1.2$), jets are balanced against
 2162 photons and the leptonic decays of Z bosons and high momentum jets ($p_T > 210$
 2163 GeV) are also balanced against multiple smaller jets in multijet events. Jets at
 2164 larger pseudorapidities, above $|\eta| = 1.2$, are calibrated by balancing with lower
 2165 pseudorapidity jets.

2166 These steps introduce a number of systematic uncertainties, referred to as
 2167 the [JES](#) uncertainty. The largest of these comes from the in-situ measurements,
 2168 which are statistically limited in measuring high momentum and high pseudora-
 2169 pidity jets. The total, fractional [JES](#) uncertainty is shown as a function of p_T in
 2170 Figure 42. The uncertainty falls to a minimum value of just over 1.0% around a
 2171 few hundred GeV, and rises again at high momentum because of the difficulty of
 2172 measuring jet balance in data above 2-3 TeV. The uncertainty is also minimized
 2173 at low $|\eta|$, and grows at large $|\eta|$ again where making in-situ measurements is
 2174 difficult. This technique does not actually provide a measurement of the uncer-
 2175 tainty for the highest energy jets, above 3 TeV, because there are not enough
 2176 measured data events to provide them. An alternative method for deriving the
 2177 [JES](#) and [JES](#) uncertainty that can be used even for very high p_T jets will be dis-
 2178 cussed in Chapter 9.

2179 7.5 MISSING TRANSVERSE ENERGY

2180 Among [SM](#) particles, only the neutrino cannot be directly measured in the [ATLAS](#)
 2181 detector. Because the neutrino carries neither electric nor color charge, it is very
 2182 unlikely to interact with the tracking detectors or the calorimeters, and instead

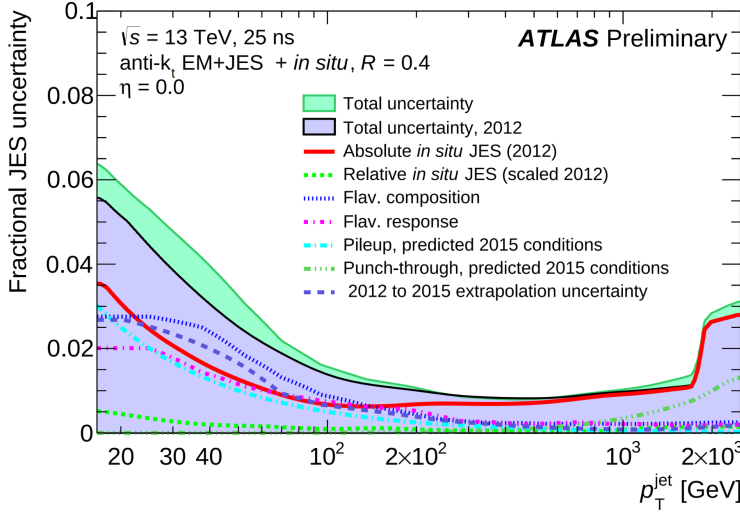


Figure 42: The total, fractional JES uncertainties estimated for 2015 data as a function of jet p_T .

2183 passes through the detector completely unobserved. Some particles which have
 2184 been conjectured to exist, like the LSP in many SUSY models, would also have
 2185 the same behavior. Therefore, it is important for ATLAS to provide some way
 2186 to assess the momentum carried away by a neutral, colorless particle. This can
 2187 be accomplished through a measurement of missing energy in the transverse di-
 2188 rection, or E_T^{miss} , which quantifies the momentum imbalance of the observed
 2189 particles. From the conservation of momentum and the lack of the initial mo-
 2190 mentum in the transverse plane in the proton-proton collisions, any imbalance
 2191 of momentum can be inferred to be carried away by an unmeasured particle.

2192 E_T^{miss} is more precisely defined as the magnitude of the vector sum of the
 2193 (p_x, p_y) components of each observed object's momentum. The definition is
 2194 simple, but there can be significant complexity in defining the inputs. As of Run
 2195 2, ATLAS uses a common algorithmic approach to carefully calculate missing en-
 2196 ergy, but each analysis is free to define its own inputs. For the analysis discussed
 2197 throughout this thesis, the missing energy inputs consist of the electrons, pho-
 2198 tons, muons, and jets discussed in the previous sections, in addition to a track-
 2199 based soft term.

2200 To produce the most precise measurement of E_T^{miss} , it is important to use the
 2201 best representation of the momentum of each of the input objects, which can
 2202 often be reconstructed as multiple different types in a single event. For example,
 2203 an electron can be reconstructed separately as an electron (Section 7.2) and a
 2204 jet (Section 7.4), but the electron representation has the highest precision for
 2205 reconstructing the true electron momentum. To ensure no duplications in the
 2206 E_T^{miss} definition, the inputs are collectively considered for overlap removal. Only
 2207 the most precise object type is kept for objects that fall within a cone of $\Delta R < 0.2$
 2208 for pairs of electrons and jets and a cone of $\Delta R < 0.4$ for other pair types.

2209 The fully reconstructed objects do not include all of the energy within the
 2210 events, as some clusters do not enter into a jet and some tracks are not classified
 2211 as electrons or muons. These momentum carried by these objects is accounted

2212 for in a soft-term, which tallies all of the energy carried by the particles too soft
2213 to form separate objects. The track soft term uses only tracking information to
2214 estimate the contribution of soft objects, and does so by vectorially summing the
2215 momentum of all well-reconstructed tracks with momentum above 400 MeV.

2216 All of these contributions together give a single E_T^{miss} value for a given event.
2217 The direction of that missing energy is taken as opposite the vector sum of all the
2218 constituents, to correspond to the momentum an invisible particle would have to
2219 have to make the event balanced. Depending on the context, this missing energy
2220 can be considered the energy of a neutrino or an LSP, with a large missing energy
2221 being a common signal criteria for searches for new physics.

2222

PART IV

2223

CALORIMETER RESPONSE

2224

You can put some informational part preamble text here.

8

2225

2226 RESPONSE MEASUREMENT WITH SINGLE HADRONS

2227 As discussed in Section 7.4, colored particles produced in collisions hadronize
2228 into jets of multiple hadrons. One approach to understanding jet energy mea-
2229 surements in the ATLAS calorimeters is to evaluate the calorimeter response to
2230 those individual hadrons; measurements of individual hadrons can be used to
2231 build up an understanding of the jets that they form. The redundancy of the
2232 momentum provided by the tracking system and the energy provided by the
2233 calorimeter provides an opportunity to study calorimeter response using real
2234 collisions, as described further in Section 8.2.

2235 Calorimeter response includes a number of physical effects that can be ex-
2236 tracted to provide insight into many aspects of jet modeling. First, many charged
2237 hadrons interact with the material of the detector prior to reaching the calorime-
2238 ters and thus do not deposit any energy. Comparing this effect in data and simu-
2239 lation is a powerful tool in validating the interactions of particles with the mate-
2240 rial of the detector and the model of the detector geometry in simulation, see Sec-
2241 tion 8.2.2. The particles which do reach the calorimeter deposit their energy into
2242 several adjacent cells, which are then clustered together. The energy of the clus-
2243 ter is then the total energy deposited by that particle. Comparing the response of
2244 hadrons in data to that of simulated hadrons provides a direct evaluation of the
2245 showering of hadronic particles and the energy deposited by particles in matter
2246 (Section 8.2.4).

2247 The above studies all use an inclusive selection of charged particles, which are
2248 comprised predominantly of pions, kaons, and (anti)protons. It is also possible to
2249 measure the response to various identified particle types separately to evaluate
2250 the simulated interactions of each particle, particularly at low energies where
2251 differences between species are very relevant. Pions and (anti)protons can be
2252 identified through decays of long-lived particles, in particular Λ , $\bar{\Lambda}$, and K_S^0 , and
2253 then used to measure response as described above. This is discussed in detail in
2254 Section 8.3.

2255 The results in this chapter use data collected at 7 and 8 TeV collected in 2010
2256 and 2012, respectively. Both are included as the calorimeter was repaired and
2257 recalibrated between those two data-taking periods. Both sets of data are com-
2258 pared to an updated simulation that includes new physics models provided by
2259 Geant4 [18] and improvements in the detector description [19, 20]. The present
2260 results are published in European Physical Journal C (EPJC) [21] and can be com-
2261 compared to a similar measurement performed in 2009 and 2010 [22], which used
2262 the previous version of the simulation framework [23].

2263 8.1 DATASET AND SIMULATION

2264 8.1.1 DATA SAMPLES

2265 The two datasets used in this chapter are taken from dedicated low-pileup runs
 2266 where the fraction of events with multiple interactions was negligible. These
 2267 datasets are used rather than those containing full-pileup events to facilitate mea-
 2268 surement of isolated hadrons. The 2012 dataset at $\sqrt{s} = 8$ TeV contains 8 mil-
 2269 lion events and corresponds to an integrated luminosity of 0.1 nb^{-1} . The 2010
 2270 dataset at $\sqrt{s} = 7$ TeV contains 3 million events and corresponds to an inte-
 2271 grated luminosity of 3.2 nb^{-1} . The latter dataset was also used for the 2010 re-
 2272 sults [22], but it has since been reanalyzed with an updated reconstruction in-
 2273 cluding the final, best understanding of the detector description for the material
 2274 and alignment from Run 1.

2275 8.1.2 SIMULATED SAMPLES

2276 The two datasets above are compared to simulated single-, double-, and non-
 2277 diffractive events generated with Pythia8 [24] using the A2 configuration of
 2278 hadronization [25] and the MSTW 2008 parton-distribution function set [26,
 2279 27]. The admixture of the single-, double-, and non-diffractive events uses the
 2280 default relative contributions from Pythia8. The conditions and energies for
 2281 the two simulations are chosen so that they match those of the corresponding
 2282 dataset.

2283 To evaluate the interaction of hadrons with detector material, the simulation
 2284 uses two different collections of hadronic physics models, called physics lists, in
 2285 Geant4 9.4 [28]. The first, QGSP_BERT, combines the Bertini intra-nuclear
 2286 cascade [29–31] below 9.9 GeV, a parametrized proton inelastic model from 9.5
 2287 to 25 GeV [32], and a quark-gluon string model above 12 GeV [33–37]. The
 2288 second, FTFP_BERT, combines the Bertini intra-nuclear cascade [29–31] below
 2289 5 GeV and the Fritiof model [38–41] above 4 GeV. In either list, Geant4 en-
 2290 forces a smooth transition between models where multiple models overlap.

2291 8.1.3 EVENT SELECTION

2292 The event selection for this study is minimal, as the only requirement is selecting
 2293 good-quality events with an isolated track. Such events are triggered by requir-
 2294 ing at least two hits in the minimum-bias trigger scintillators. After trigger, each
 2295 event is required to have exactly one reconstructed vertex, and that vertex is re-
 2296 quired to have four or more associated tracks.

2297 The particles which are selected for the response measurements are first iden-
 2298 tified as tracks in the inner detector. The tracks are required to have at least 500
 2299 MeV of transverse momentum. To ensure a reliable momentum measurement,
 2300 these tracks are required to have at least one hit in the pixel detector, six hits in
 2301 the SCT, and small longitudinal and transverse impact parameters with respect
 2302 to the primary vertex [22]. For the majority of the measurements in this chapter,

2303 the track is additionally required to have 20 hits in the TRT, which significantly
 2304 reduces the contribution from tracks which undergo nuclear interactions. This
 2305 requirement and its effect is discussed in more detail in Section 8.2.5. In addition,
 2306 tracks are rejected if there is any other reconstructed track which extrapolates
 2307 to the calorimeter within a cone of $\Delta R = \sqrt{(\Delta\phi)^2 + (\Delta\eta)^2} < 0.4$. This require-
 2308 ment guarantees that the contamination of energy from nearby charged particles
 2309 is negligible [22].

2310 8.2 INCLUSIVE HADRON RESPONSE

2311 The calorimeter response is more precisely defined as the ratio of the measured
 2312 calorimeter energy to the true energy carried by the particle, although this true
 2313 energy is unknown. For charged particles, however, the inner detector provides
 2314 a very precise measurement of momentum (with uncertainty less than 1%) that
 2315 can be used as a proxy for true energy. The ratio of the energy deposited by
 2316 the charged particle in the calorimeter, E , to its momentum measured in the
 2317 inner detector p , forms the calorimeter response measure called E/p . Though
 2318 the distribution of E/p contains a number of physical features, this study focuses
 2319 on the trends in two aggregated quantities: $\langle E/p \rangle$, the average of E/p for the
 2320 selected tracks, and the zero fraction, the fraction of tracks with no associated
 2321 energy in the calorimeter for those tracks.

2322 The calorimeter energy assigned to a track is defined using clusters. The clus-
 2323 ters are formed using a 4–2–0 algorithm [42] that begins with seeds requiring
 2324 at least 4 times the average calorimeter cell noise. The neighboring cells with
 2325 at least twice that noise threshold are then added to the cluster, and all bound-
 2326 ing cells are then added with no requirement. This algorithm minimizes noise
 2327 contributions through its seeding process, and including the bounding cells im-
 2328 proves the energy resolution [43]. The clusters are associated to a given track
 2329 if they fall within a cone of $\Delta R = 0.2$ of the extrapolated position of the track,
 2330 which includes about 90% of the energy on average [22]. This construction is
 2331 illustrated in Figure 43.

2332 8.2.1 E/P DISTRIBUTION

2333 The E/p distributions measured in both data and simulation are shown in Fig-
 2334 ure 44 for two example bins of track momentum and for tracks in the central
 2335 region of the detector. These distributions show several important features of
 2336 the E/p observable. The large content in the bin at $E = 0$ comes from tracks that
 2337 have no associated cluster, which occurs due to interactions with detector mate-
 2338 rial prior to reaching the calorimeter or the energy deposit being insufficiently
 2339 large to generate a seed, and are discussed in Section 8.2.2. The small negative
 2340 tail also comes from tracks that do not deposit any energy in the calorimeter but
 2341 are randomly associated to a cluster with an energy below the noise threshold.
 2342 The long positive tail above 1.0 comes from the contribution of neutral parti-
 2343 cles. Nearby neutral particles deposit (sometimes large) additional energy in the
 2344 calorimeter but do not produce tracks in the inner detector, so they cannot be

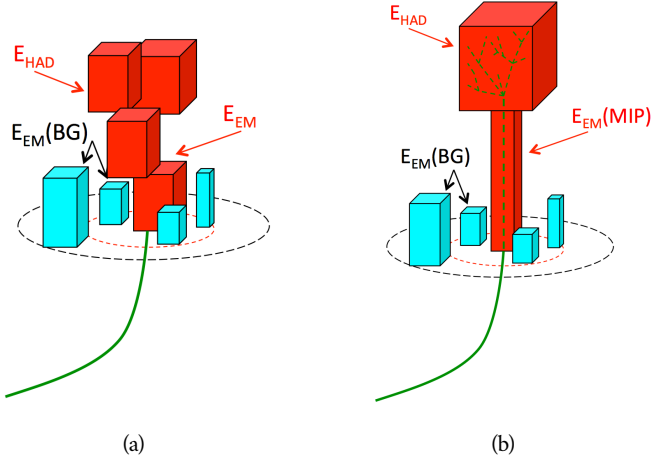


Figure 43: An illustration (a) of the E/p variable used throughout this paper. The red energy deposits come from the charged particle targeted for measurement, while the blue energy deposits are from nearby neutral particles and must be subtracted. The same diagram (b) for the neutral-background selection, described in Section 8.2.3.

2345 rejected by the track isolation requirement. Additionally the peak and mean of
 2346 the distribution falls below 1.0 because of the loss of energy not found within
 2347 the cone as well as the non-compensation of the calorimeter.

2348 The data and simulation share the same features, but the high and low tails
 2349 are significantly different. The simulated events tend to overestimate the con-
 2350 tribution of neutral particles to the long tail, an effect which can be isolated and
 2351 removed as discussed in Section 8.2.3. Additionally, the simulated clusters have
 2352 less noise on average, although this is a small effect on the overall response.

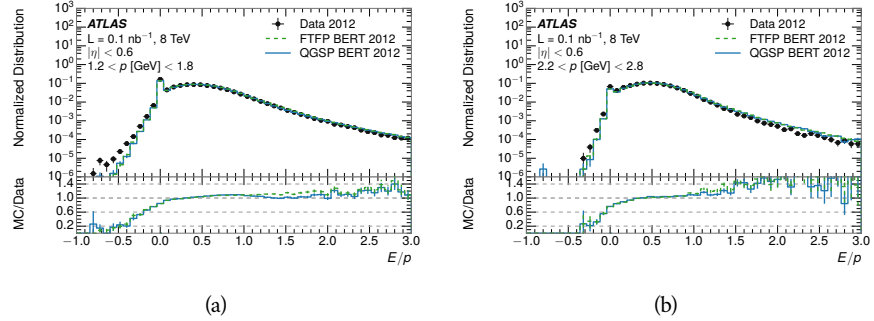


Figure 44: The E/p distribution and ratio of simulation to data for isolated tracks with
 (a) $|\eta| < 0.6$ and $1.2 < p/\text{GeV} < 1.8$ and (b) $|\eta| < 0.6$ and $2.2 < p/\text{GeV} < 2.8$.

2353 8.2.2 ZERO FRACTION

2354 The fraction of particles with no associated clusters, or similarly those with $E \leq$
 2355 0, reflects the modeling of both the detector geometry and hadronic interactions.

The zero fraction is expected to rise as the amount of material a particle traverses increases, while it is expected to decrease as the particle energy increases. This dependence can be seen in Figure 45, where the zero fraction in data and simulation is shown as a function of momentum and the amount of material measured in interaction lengths. The trends are similar between 2010 and 2012 and for positively and negatively charged particles. The zero fraction decreases with energy as expected. The absolute discrepancy in zero fraction decreases with momentum from 5% to less than 1%, but this becomes more pronounced in the ratio as the zero fraction shrinks quickly with increasing momentum. There is a small constant difference between the data and simulation in both interaction models that becomes more pronounced. The amount of material in the detector increases with η , which is used to obtain results for interaction lengths ranging between 0.1 and 0.65 λ . As the data and simulation have significant disagreement in the zero fraction over a number of interaction lengths, the difference must be primarily from the modeling of hadronic interactions with detector material and not just the detector geometry. Although two different hadronic interaction models are shown in the figure, they have very similar discrepancies to data because both use the same description (the BERT model) at low momentum.

8.2.3 NEUTRAL BACKGROUND SUBTRACTION

The isolation requirement on hadrons is only effective in removing an energy contribution from nearby charged particles. Nearby neutral particles, predominantly photons from π^0 decays, also add their energy to the calorimeter clusters, but mostly in the electromagnetic calorimeter. It is possible to measure this contribution, on average, using late-showering hadrons that minimally ionize in the electromagnetic calorimeter. Such particles are selected by requiring that they deposit less than 1.1 GeV in the EM calorimeter within a cone of $\Delta R < 0.1$ around the track. To ensure that these particles are well measured, they are additionally required to deposit between 40% and 90% of their energy in the hadronic calorimeter within the same cone.

These particles provide a clean sample to measure the nearby neutral background because they do not deposit energy in the area immediately surrounding them in the EM calorimeter, as shown in Figure 43. So, the energy deposits in the region $0.1 < \Delta R < 0.2$ can be attributed to neutral particles alone. To estimate the contribution to the whole cone considered for the response measurement, that energy is scaled by a geometric factor of 4/3. This quantity, $\langle E/p \rangle_{BG}$, measured in aggregate over a number of particles, gives the contribution to $\langle E/p \rangle$ from neutral particles in the EM calorimeter. Similar techniques were used in the individual layers of the hadronic calorimeters to show that the background from neutrals is negligible in those layers [22].

The distribution of this background estimate is shown in Figure 46 for data and simulation with the two different physics lists. The contribution from neutral particles falls from 0.1 at low momentum to around 0.03 for particles above 7 GeV. Although the simulation captures the overall trend, it significantly overestimates the neutral contribution for tracks with momentum between 2 and 8

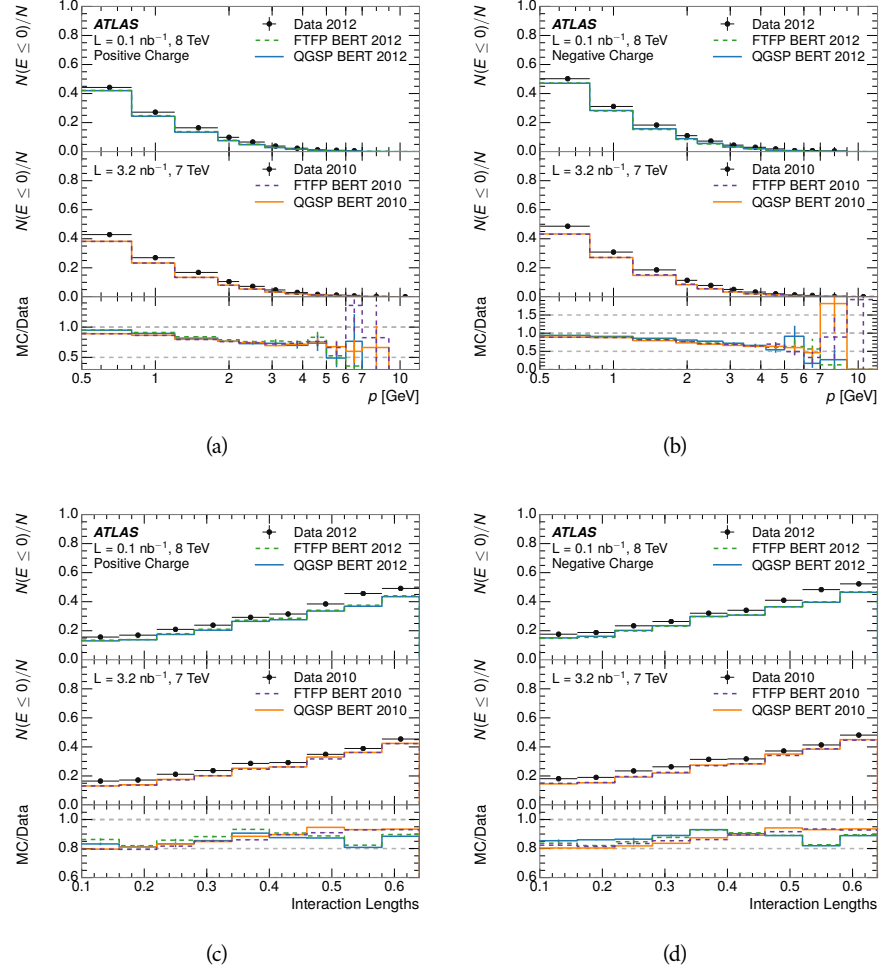


Figure 45: The fraction of tracks as a function (a, b) of momentum, (c, d) of interaction lengths with $E \leq 0$ for tracks with positive (on the left) and negative (on the right) charge.

2400 GeV. This effect was also seen in the tails of the E/p distributions in Figure 44.
 2401 This difference is likely due to modeling of coherent neutral particle radiation
 2402 in Pythia8 that overestimates the production of π^0 near the production of the
 2403 charged particles. The discrepancy does not depend on η and thus is unlikely to
 2404 be a mismodeling of the detector. This difference can be subtracted to form a
 2405 corrected average E/p , as in Section 8.2.4.

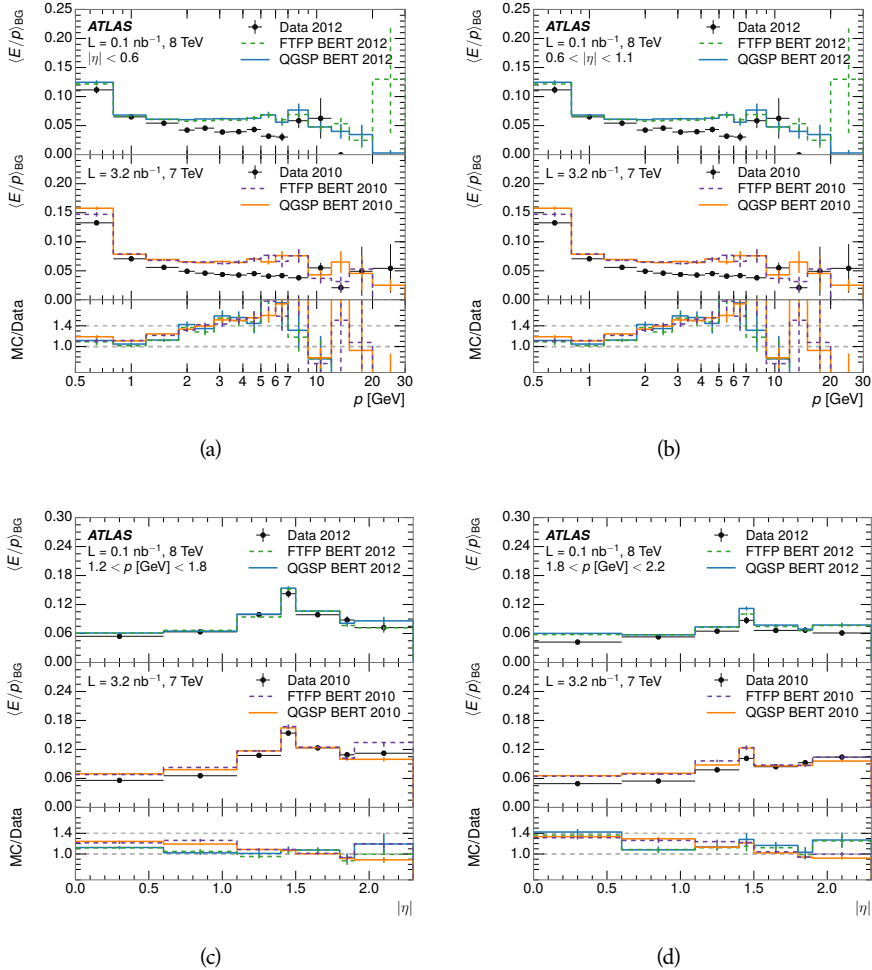


Figure 46: $\langle E/p \rangle_{BG}$ as a function of the track momentum for tracks with (a) $|\eta| < 0.6$,
 (b) $0.6 < |\eta| < 1.1$, and as a function of the track pseudorapidity for tracks
 with (c) $1.2 < p/\text{GeV} < 1.8$, (d) $1.8 < p/\text{GeV} < 2.2$.

2406 8.2.4 CORRECTED RESPONSE

2407 Figure 47 shows $\langle E/p \rangle_{COR}$ as a function of momentum for several bins of pseudo-
 2408 rapidity. This corrected $\langle E/p \rangle_{COR} \equiv \langle E/p \rangle - \langle E/p \rangle_{BG}$ measures the average
 2409 calorimeter response without the contamination of neutral particles. It is the
 2410 most direct measurement of calorimeter response in that it is the energy mea-
 2411 sured for fully isolated hadrons. The correction is performed separately in data
 2412 and simulation, so that the mismodeling of the neutral background in simulation

is removed from the comparison of response. The simulation overestimates the response at low momentum by about 5%, an effect that can be mostly attributed to the underestimation of the zero fraction mentioned previously. For $|\eta| < 0.6$, the data-simulation agreement has a larger discrepancy by about 5% for 2010 than 2012, although this is not reproduced in at higher pseudorapidity.

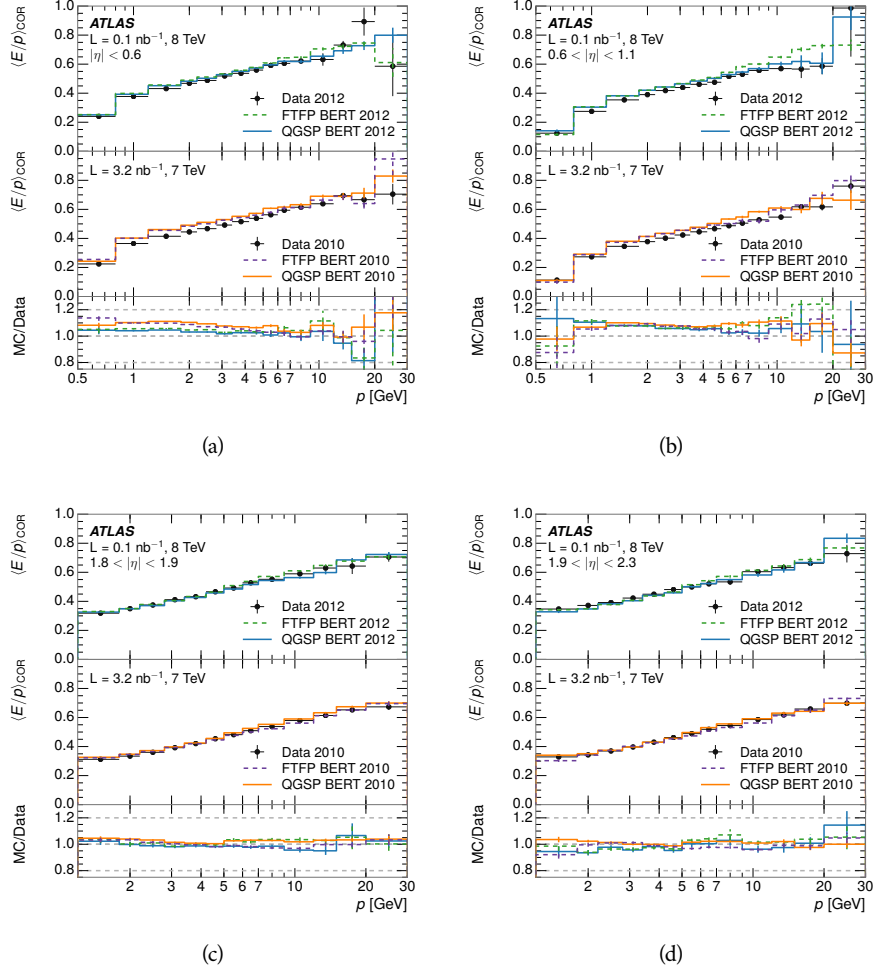


Figure 47: $\langle E/p \rangle_{\text{COR}}$ as a function of track momentum, for tracks with (a) $|\eta| < 0.6$, (b) $0.6 < |\eta| < 1.1$, (c) $1.8 < |\eta| < 1.9$, and (d) $1.9 < |\eta| < 2.3$.

The response measurement above used topological clustering at the EM scale, that is clusters were formed to measure energy but no corrections were applied to correct for expected effects like energy lost outside of the cluster or in uninstrumented material. It is also interesting to measure $\langle E/p \rangle_{\text{COR}}$ using LCW energies, which accounts for those effects by calibrating the energy based on the properties of the cluster such as energy density and depth in the calorimeter. Figure 48 shows these distributions for tracks with zero or more clusters and separately for tracks with one or more clusters. The calibration moves the mean value of $\langle E/p \rangle_{\text{COR}}$ significantly closer to 1.0 as desired. The agreement between data and simulation improves noticeably when at least one cluster is required, as this removes the contribution from the mismodeling of the zero fraction. The

good agreement in that case again demonstrates that the difference in $\langle E/p \rangle_{\text{COR}}$ between data and simulation is caused predominantly by the difference in zero fraction.

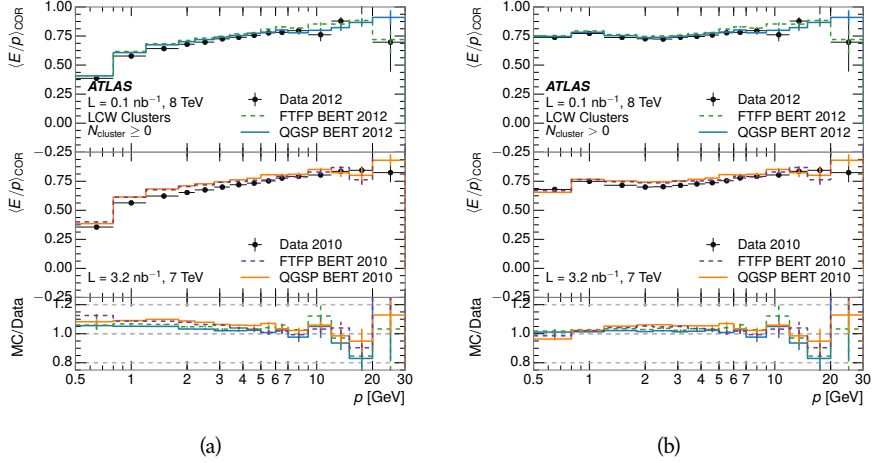


Figure 48: $\langle E/p \rangle_{\text{COR}}$ calculated using LCW-calibrated topological clusters as a function of track momentum for tracks with (a) zero or more associated topological clusters or (b) one or more associated topological clusters.

8.2.5 ADDITIONAL STUDIES

As has been seen in several measurements in previous sections, the simulation does not correctly model the chance of a low momentum hadron to reach the calorimeter. Because of the consistent discrepancy across pseudorapidity and interaction lengths, this can be best explained by incomplete understanding of hadronic interactions with the detector [21]. For example, a hadron that scatters off of a nucleus in the inner detector can be deflected through a significant angle and not reach the expected location in the calorimeter. In addition, these interactions can produce secondary particles that are difficult to model.

The requirement used throughout the previous sections on the number of hits in the TRT reduces these effects by preferentially selecting tracks that do not undergo nuclear interactions. It is interesting to check how well the simulation models tracks with low numbers of TRT hits, which selects tracks that are more likely to have undergone a hadronic interaction. Figure 49 compares the distributions with $N_{\text{TRT}} < 20$ to $N_{\text{TRT}} > 20$ for real and simulated particles. As expected, the tracks with fewer hits are poorly modeled in the simulation as $\langle E/p \rangle_{\text{COR}}$ differs by as much as 25% at low momentum.

Another interesting aspect of the simulation is the description of antiprotons at low momentum, where QGSP_BERT and FTFP_BERT have significant differences. This can be seen to have an effect in the inclusive response measurement when separated into positive and negative charge. The $\langle E/p \rangle_{\text{COR}}$ distributions for positive and negative particles are shown in Figure 50, where a small difference between QGSP_BERT and FTFP_BERT can be seen in the distribution for

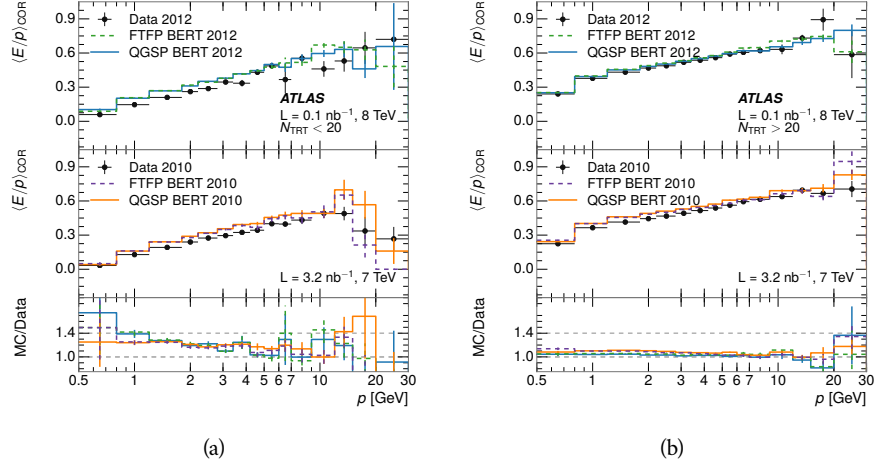


Figure 49: Comparison of the $\langle E/p \rangle_{\text{COR}}$ for tracks with (a) less than and (b) greater than 20 hits in the TRT.

negative tracks. This is demonstrated more clearly in Figure 51, which shows the E/p distribution in the two simulations separated by charge. There is a clear difference around $E/p > 1.0$, which can be explained by the additional energy deposited by the annihilation of the antiproton in the calorimeter that is modeled well only in FTFP_BERT. This is also explored with data using identified antiprotons in Section 8.3.

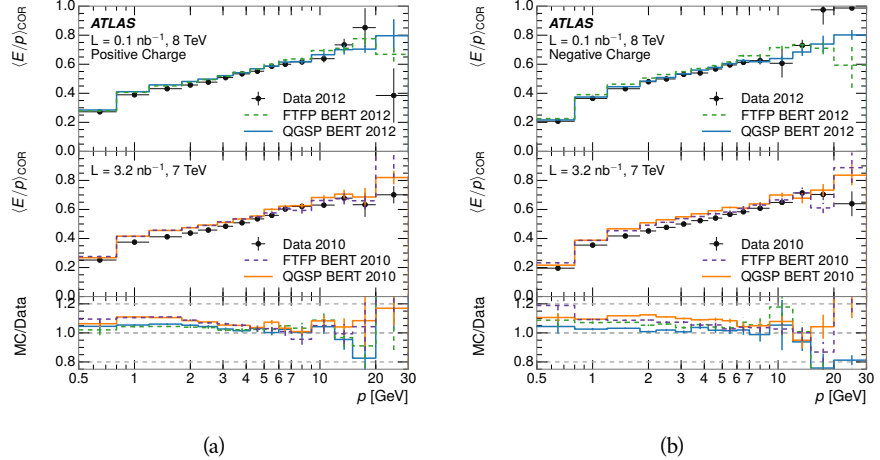


Figure 50: Comparison of the $\langle E/p \rangle_{\text{COR}}$ for (a) positive and (b) negative tracks as a function of track momentum for tracks with $|\eta| < 0.6$.

The $\langle E/p \rangle$ results in previous sections have considered the electromagnetic and hadronic calorimeters together as a single energy measurement, to emphasize the total energy deposited for a given particle. However, the deposits in each calorimeter are available separately and $\langle E/p \rangle$ can be constructed for each layer. As the layers are composed of different materials and are modeled separately in the detector geometry, confirmation that the simulation matches the data well

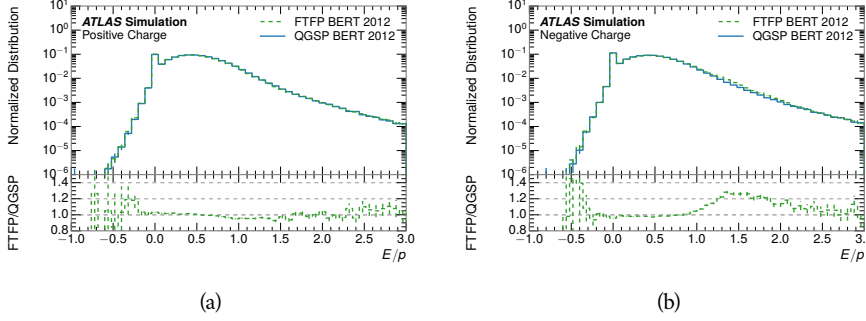


Figure 51: Comparison of the E/p distributions for (a) positive and (b) negative tracks with $0.8 < p/\text{GeV} < 1.2$ and $|\eta| < 0.6$, in simulation with the FTFP_BERT and QGSP_BERT physics lists.

in each layer adds confidence in both the description of hadronic interactions with the two different materials and also the geometric description of each.

The technique discussed in Section 8.2.3 for selecting MIPs in the electromagnetic calorimeter is also useful in studying deposits in the hadronic calorimeter. Those MIPs deposit almost all of their energy exclusively in the hadronic calorimeter. Figure 52 shows $\langle E/p \rangle_{\text{RAW}}^{\text{Had}}$, where RAW indicates that no correction has been applied for neutral backgrounds and Had indicates that only clusters for the hadronic calorimeter are included. The RAW and COR versions of $\langle E/p \rangle$ in this case are the same, as the neutral background is negligible in that calorimeter layer. The distributions are shown both for the original EM scale calibration and after LCW calibration. The data and simulation agree very well in this comparison, except in the lowest momentum bin which has 5% discrepancy that has already been seen in similar measurements.

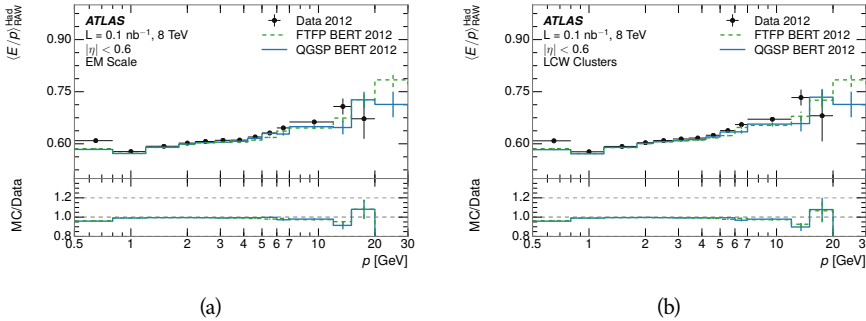


Figure 52: Comparison of the response of the hadronic calorimeter as a function of track momentum (a) at the EM-scale and (b) after the LCW calibration.

A similar comparison can be made in the electromagnetic calorimeter by selecting particles which have no associated energy in the hadronic calorimeter. These results are measured in terms of $\langle E/p \rangle_{\text{COR}}^{\text{EM}}$, where EM designates that only clusters in the electromagnetic calorimeter are included and COR designates that the neutral background is subtracted as the neutral background is present in this case. Figure 53 shows the analogous comparisons to Figure 52 in

2486 the electromagnetic calorimeter. In this case the disagreement between data and
 2487 simulation is more pronounced, with discrepancies as high as 5% over a larger
 2488 range of momenta. This level of discrepancy indicates that the description of
 2489 the electromagnetic calorimeter is actually the dominant source of discrepancy
 2490 in the combined distributions in Section 8.2.4.

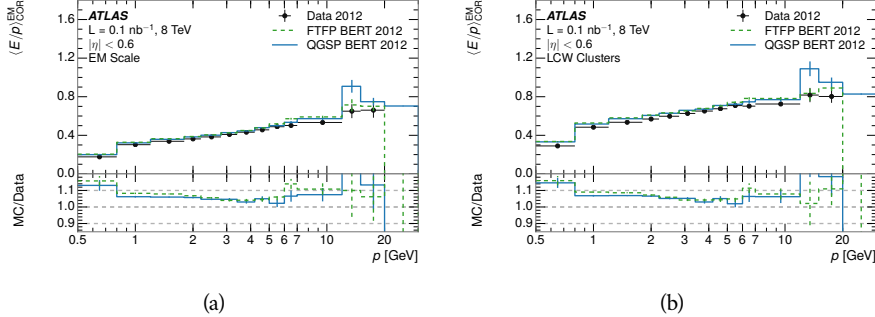


Figure 53: Comparison of the response of the EM calorimeter as a function of track momentum (a) at the EM-scale and (b) with the LCW calibration.

2491 **NOTE: There are more studies that I skipped for brevity that could be in-**
 2492 **cluded if interesting. E/p at different cluster threshold settings, E/p with**
 2493 **pileup, E/p with cells. I also left out a lot of eta bins that appear in the**
 2494 **paper so that this section didn't turn into 20 pages of plots.**

2495 8.3 IDENTIFIED PARTICLE RESPONSE

2496 The inclusive response measurement for hadrons can be augmented by measur-
 2497 ing the response for specific particle species. The simulation models each parti-
 2498 cle type separately, and understanding the properties of each is important in con-
 2499 straining the uncertainty on jets. In order to select and measure specific hadrons,
 2500 this section relies on the displaced decays of long-lived particles. Such decays
 2501 can be identified by reconstructing secondary vertices with a requirement on
 2502 mass. In particular, Λ , $\bar{\Lambda}$, and K_S^0 can be used to select a pure sample of protons,
 2503 antiprotons, and pions, respectively.

2504 8.3.1 DECAY RECONSTRUCTION

2505 The measurement of response for identified particles uses the same selection as
 2506 for inclusive particles (Section 8.1.3) with a few additions. Each event used is
 2507 required to have at least one secondary vertex, and the tracks are required to
 2508 match to that vertex rather than the primary vertex. Pions are selected from
 2509 decays of $K_S^0 \rightarrow \pi^+ \pi^-$, which is the dominant decay for K_S^0 to charged particles.
 2510 Protons are selected from decays of $\Lambda \rightarrow \pi^- p$ and antiprotons from $\bar{\Lambda} \rightarrow \pi^+ \bar{p}$,
 2511 which are similarly the dominant decays of Λ and $\bar{\Lambda}$ to charged particles. The
 2512 species of parent hadron in these decays is determined by reconstructing the
 2513 mass of the tracks associated to the secondary vertex. The sign of the higher

momentum decay particle can distinguish between Λ and $\bar{\Lambda}$, which of course have the same mass, as the proton or antiproton is kinematically favored to have higher momentum. Examples of the reconstructed masses used to select these decays are shown in Figure 54.

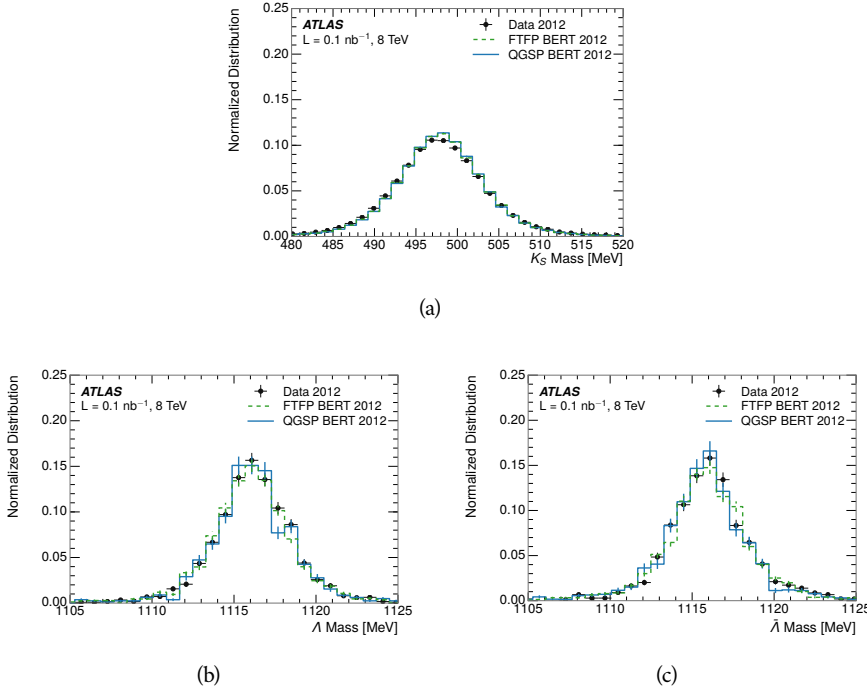


Figure 54: The reconstructed mass peaks of (a) K_S^0 , (b) Λ , and (c) $\bar{\Lambda}$ candidates.

The dominant backgrounds for the identified particle decays are nuclear interactions and combinatoric sources. These are suppressed by the kinematic requirements on the tracks as well as an additional veto which removes candidates that are consistent with both a Λ or $\bar{\Lambda}$ and a K_S^0 hypothesis, which is possible because of the different assumptions on particle mass in each case [22]. After these requirements, the backgrounds are found to be negligible compared to the statistical errors on these measurements.

8.3.2 IDENTIFIED RESPONSE

With these techniques the E/p distributions are extracted in data and simulation for each particle species and shown in Figure 55. These distributions are shown for a particular bin of E_a ($2.2 < E_a/\text{GeV} < 2.8$), rather than p . E_a is the energy available to be deposited in the calorimeter: for pions $E_a = \sqrt{p^2 + m^2}$, for protons $E_a = \sqrt{p^2 + m^2} - m$, and for antiprotons $E_a = \sqrt{p^2 + m^2} + m$. The features of the E/p distributions are similar to the inclusive case. There is a small negative tail from noise and a large fraction of tracks with zero energy from particles which do not reach the calorimeter. The long positive tail is noticeably more pronounced for antiprotons because of the additional energy generated by the annihilation in addition to the neutral background.

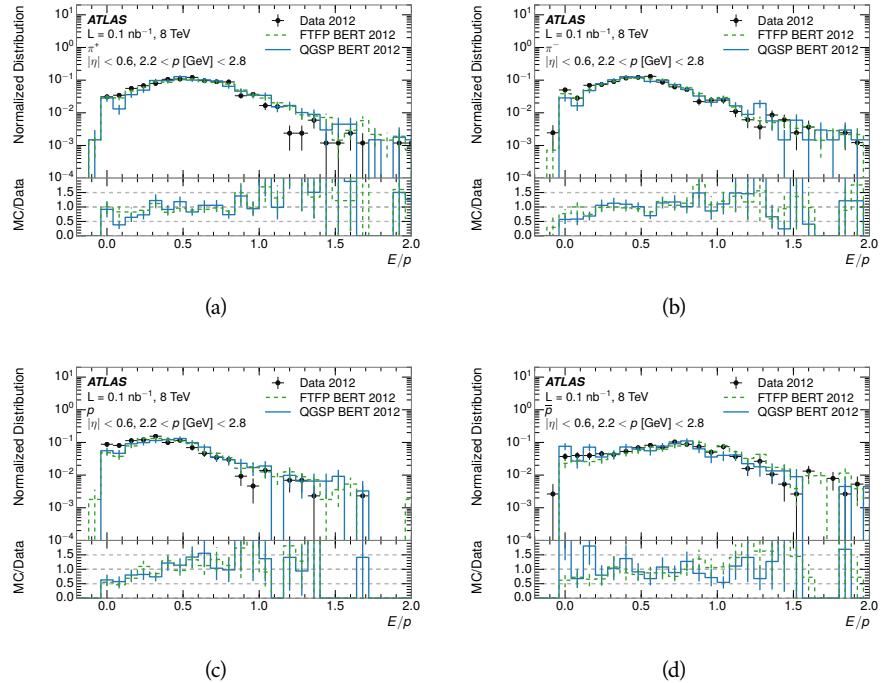


Figure 55: The E/p distribution for isolated (a) π^+ , (b) π^- , (c) proton, and (d) anti-proton tracks.

2536 The zero fraction is further explored in Figure 56 for pions and protons in data
 2537 and simulation. The simulation consistently underestimates the zero fraction
 2538 independent of particle species, which implies that this discrepancy is not caused
 2539 by the model of a particular species but rather a feature common to all.

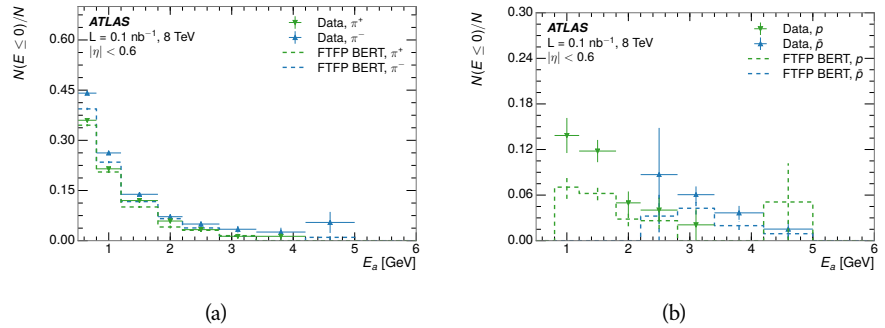


Figure 56: The fraction of tracks with $E \leq 0$ for identified (a) π^+ and π^- , and (b) proton and anti-proton tracks

2540 It is also interesting to compare the response between the different particle
 2541 species. One approach to do this is to measure the difference in $\langle E/p \rangle$ between
 2542 two types, which has the advantage of removing the neutral background. These
 2543 differences are shown in various combinations in Figure 57. The response for
 2544 π^+ is greater on average than the response to π^- because of a charge-exchange
 2545 effect which causes the production of additional neutral pions in the showers of

2546 π^+ [44]. The response for π^+ is also greater on average than the response to p ,
 2547 because a large fraction of the energy of π^+ hadrons is converted to an electro-
 2548 magnetic shower [45, 46]. However, the \bar{p} response is significantly higher than
 2549 the response to π^- because of the annihilation of the antiproton. FTFP_BERT
 2550 does a better job of modeling this effect than QGSP_BERT because of their differ-
 2551 ent descriptions of \bar{p} interactions with material.

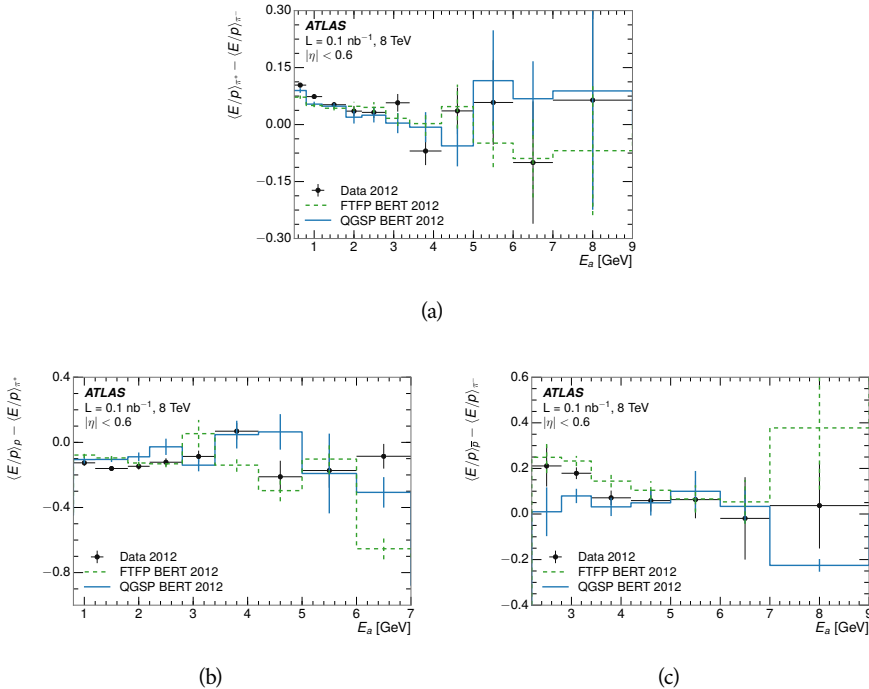


Figure 57: The difference in $\langle E/p \rangle$ between (a) π^+ and π^- (b) p and π^+ , and (c) \bar{p} and π^- .

2552 It is also possible to remove the neutral background from these response dis-
 2553 tributions using the same technique as in Section 8.2.3. The technique is largely
 2554 independent of the particle species and so can be directly applied to $\langle E/p \rangle$ for
 2555 pions. The $\langle E/p \rangle_{\text{COR}}$ distributions for pions are shown in Figure 58, which are
 2556 very similar to the inclusive results. The inclusive hadrons are comprised mostly
 2557 of pions, so this similarity is not surprising. It is also possible to see the small
 2558 differences between π^+ and π^- response here, where $\langle E/p \rangle_{\text{COR}}$ is higher on av-
 2559 erage for π^+ . The agreement between data and simulation is significantly worse
 2560 for the π^- distributions than for the π^+ , with a discrepancy greater than 10%
 2561 below 2-3 GeV.

2562 8.3.3 ADDITIONAL SPECIES IN SIMULATION

2563 The techniques above provide a method to measure the response separately for
 2564 only pions and protons. However the hadrons which forms jets include a num-
 2565 ber of additional species such as kaons and neutrons. The charged kaons are
 2566 an important component of the inclusive charged hadron distribution, which is
 2567 comprised of roughly 60-70% pions, 15-20% kaons, and 5-15% protons. These

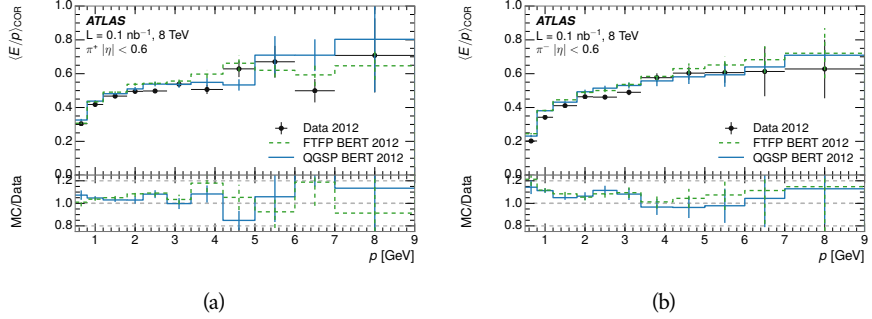


Figure 58: $\langle E/p \rangle_{\text{COR}}$ as a function of track momentum for (a) π^+ tracks and (b) π^- tracks.

are difficult to measure in data at the ATLAS detector, although a template subtraction technique has been proposed which may be effective with larger sample sizes [21]. The simulation of these particles includes noticeable differences in response at low energies, which are shown in Figure 59 for FTFP_BERT. The significant differences in response between low energy protons and antiprotons are accounted for above in the definitions of E_a .

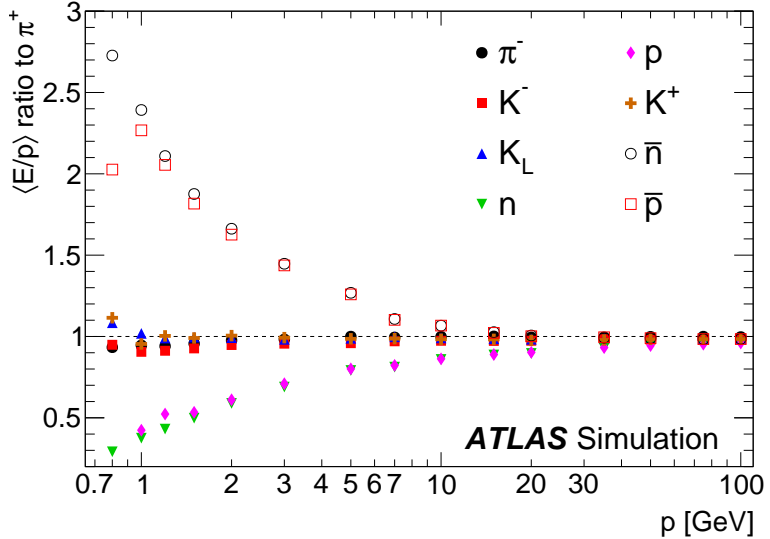


Figure 59: The ratio of the calorimeter response to single particles of various species to the calorimeter response to π^+ with the physics list FTFP_BERT.

8.4 SUMMARY

These various measurements of calorimeter response shown above for data and simulation illuminate the accuracy of the simulation of hadronic interactions at the ATLAS detector. The results were done using 2010 and 2012 data at 7 and 8 TeV, but reflect the most current understanding of the detector alignment and geometry. A number of measurements focusing on a comparison between pro-

2580 tons and antiprotons suggest that FTFP_BERT models those interaction more
2581 accurately than QGSP_BERT. These measurements, among others, were the moti-
2582 vation to switch the default Geant4 simulation from FTFP_BERT to QGSP_BERT
2583 for all ATLAS samples.

2584 Even with these updates, there are a number of small, approximately 5%, dis-
2585 crepancies in response between the data and simulation at low energies. At
2586 higher energies the simulation of hadronic interactions is very consistent with
2587 data. Chapter 9 discusses how to use these observed differences to constrain the
2588 jet energy scale and its associated uncertainties.

2589

2590 JET ENERGY RESPONSE AND UNCERTAINTY

2591 9.1 MOTIVATION

2592 As jets form a major component of many physics analyses at ATLAS, it is crucial
 2593 to carefully calibrate the measurement of jet energies and to derive an uncer-
 2594 tainty on that measurement. These uncertainties have often been the dominant
 2595 systematic uncertainty in high-energy analyses at the LHC. Dijet and multijet
 2596 balance techniques provide a method to constrain the JES and its uncertainty in
 2597 data, and provide the default values used for ATLAS jet measurements at most
 2598 energies [47]. These techniques are limited by their reliance on measuring jets
 2599 in data, so they are statistically limited in estimating the jet energy scale at the
 2600 highest jet energies. This chapter presents another method for estimating the jet
 2601 energy scale and its uncertainty which builds up a jet from its components and
 2602 thus can be naturally extended to high jet momentum. Throughout this chapter
 2603 the jets studied are simulated using Pythia8 with the CT10 parton distribution
 2604 set [48] and the AU2 tune [25], and corrections are taken from the studies includ-
 2605 ing data and simulation in Chapter 8.

2606 As described in Section 7.4, jets are formed from topological clusters of energy
 2607 in the calorimeters using the anti- k_t algorithm. These clusters originate from a
 2608 diverse spectrum of particles, in terms of both species and momentum, leading to
 2609 significantly varied jet properties and response between jets of similar produced
 2610 momentum. Figure 60 shows the simulated distribution of particles within jets
 2611 at a few examples energies. The E/p measurements provide a thorough under-
 2612 standing of the dominant particle content of jets, the charged hadrons.

2613 9.2 UNCERTAINTY ESTIMATE

2614 Simulated jets are not necessarily expected to correctly model the energy de-
 2615 posits in the calorimeters, because of the various discrepancies discussed in Chap-
 2616 ter 8. To evaluate a jet energy response, the simulated jet energies are compared
 2617 to a corrected jet built up at the particle level. Each cluster in a jet is associated
 2618 to the truth particle which deposited it, and the energy in that cluster is then
 2619 corrected for a number of effects based on measurements in data. The primary
 2620 corrections come from the single hadron response measurements in addition to
 2621 response measured using the combined test beam which covers higher momen-
 2622 tum particles [49]. These corrections include both a shift (Δ), in order to make
 2623 the simulation match the average response in data, and an uncertainty (σ) asso-
 2624 ciated with the ability to constrain the difference between data and simulation.
 2625 Some of the dominant sources of uncertainty are itemized in Table 8 with typi-
 2626 cal values, and the full list considered is described in detail in the associated pa-

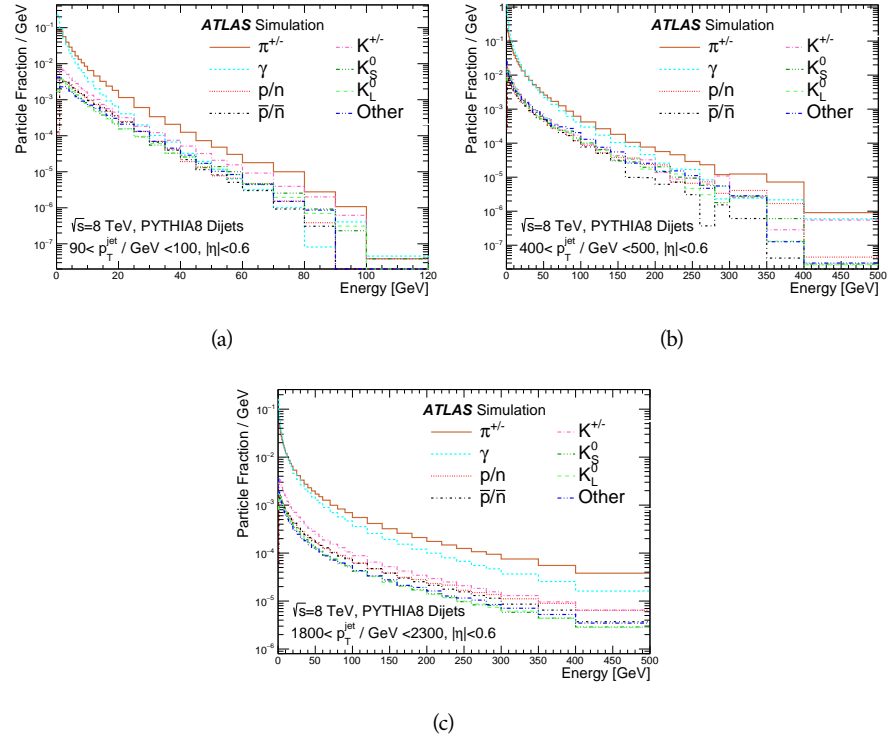


Figure 60: The spectra of true particles inside anti- k_t , $R = 0.4$ jets with (a) $90 < p_T/\text{GeV} < 100$, (b) $400 < p_T/\text{GeV} < 500$, and (c) $1800 < p_T/\text{GeV} < 2300$.

2627 per [21]. These uncertainties cover differences between the data and simulation
 2628 in the modeling of calorimeter response to a given particle. No uncertainties are
 2629 added for the difference between particle composition of jets in data and simu-
 2630 lation.

2631 From these terms, the jet energy scale and uncertainty is built up from indi-
 2632 vidual energy deposits in simulation. Each uncertainty term is treated indepen-
 2633 dently, and are taken to be gaussian distributed. The resulting scale and uncer-
 2634 tainty is shown in Figure 61, where the mean response is measured relative to
 2635 the calibrated energy reported by simulation. The dominant uncertainties come
 2636 from the statistical uncertainties on the E/p measurements at lower energies and
 2637 the additional uncertainty for out of range measurements at higher energies. The
 2638 total uncertainty from this method at intermediate jet energies is comparable to
 2639 other simulation-based methods [50] and is about twice as large as in-situ meth-
 2640 ods using data [47]. This method is the only one which provides an estimation
 2641 above 1.8 TeV, however, and so is still a crucial technique in analyses that search
 2642 for very energetic jets.

2643 These techniques can also be used to measure the correlation between bins of
 2644 average reconstructed jet momentum across a range of p_T and $|\eta|$, where cor-
 2645 relations are expected because of a similarity in particle composition at similar
 2646 energies. Figure 62 shows these correlations, where the uncertainties on jets in
 2647 neighboring bins are typically between 30% and 60% correlated. The uncertainty
 2648 on all jets becomes significantly correlated at high energies and larger pseudora-

Abbrev.	Description	Δ (%)	σ (%)
In situ E/p	The comparison of $\langle E/p \rangle_{\text{COR}}$ as described in Chapter 8 with statistical uncertainties from 500 MeV to 20 GeV.	0-3	1-5
CTB	The main $\langle E/p \rangle$ comparison uncertainties, binned in p and $ \eta $, as derived from the combined test beam results, from 20 to 350 GeV [49].	0-3	1-5
E/p Zero Fraction	The difference in the zero-fraction between data and MC simulation from 500 MeV to 20 GeV.	5-25	1-5
E/p Threshold	The uncertainty in the EM calorimeter response from the potential mismodeling of threshold effects in topological clustering.	0	0-10
Neutral	The uncertainty in the calorimeter response to neutral hadrons based on studies of physics model variations.	0	5-10
K_L	An additional uncertainty in the response to neutral K_L in the calorimeter based on studies of physics model variations.	0	20
E/p Misalignment	The uncertainty in the p measurement from misalignment of the ID.	0	1
Hadrons, $p > 350$ GeV	A flat uncertainty for all particles above the energy range or outside the longitudinal range probed with the combined test beam.	0	10

Table 8: The dominant sources of corrections and systematic uncertainties in the [JES](#) estimation technique, including typical values for the correcting shift (Δ) and the associated uncertainty (σ).

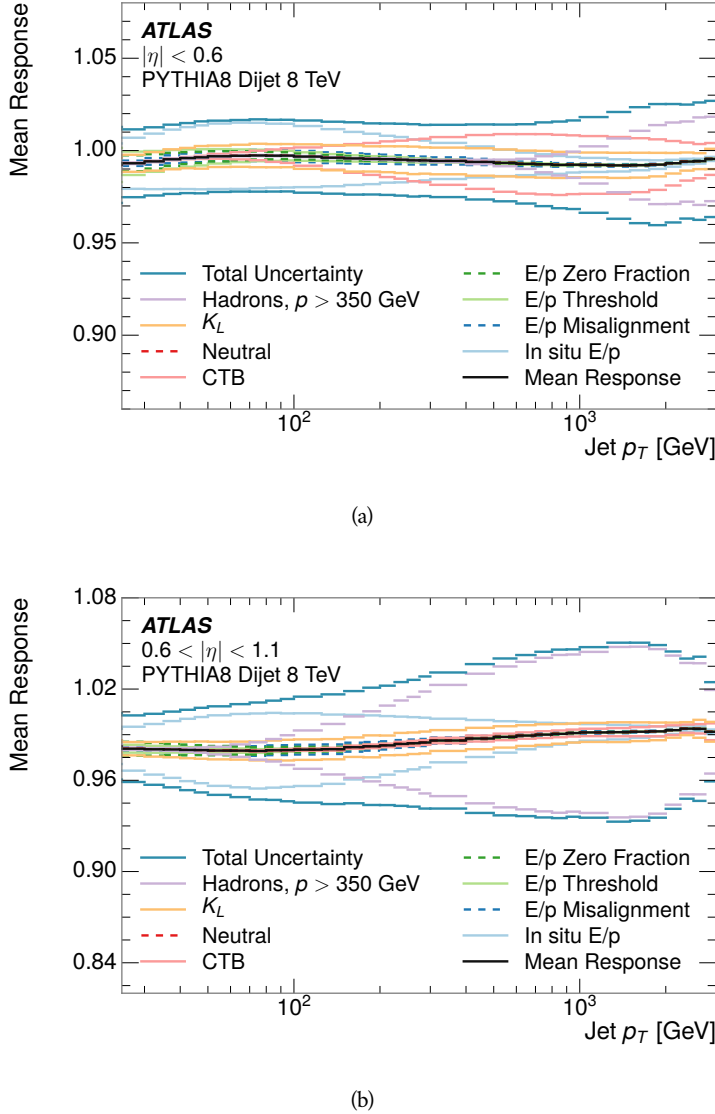


Figure 61: The [JES](#) uncertainty contributions, as well as the total [JES](#) uncertainty, as a function of jet p_T for (a) $|\eta| < 0.6$ and (b) $0.6 < |\eta| < 1.1$.

2649 pilities, when the uncertainty becomes dominated by the single term reflecting
 2650 out of range particles.

2651 9.3 SUMMARY

2652 The technique described above provides a jet energy scale and uncertainty by
 2653 building up jet corrections from the energy deposits of constituent particles. The
 2654 E/p measurements are crucial in providing corrections for the majority of parti-
 2655 cles in the jets. The uncertainty derived this way is between 2 and 5% and is about
 2656 twice as large at corresponding momentum than jet balance methods. However
 2657 this is the only uncertainty available for very energetic jets using 2012 data and
 2658 simulation, and repeating this method with Run 2 data and simulation will be

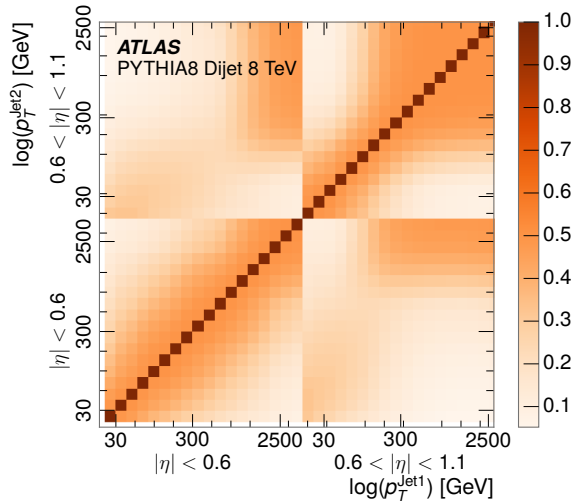


Figure 62: The **JES** correlations as a function of jet p_T and $|\eta|$ for jets in the central region of the detector.

2659 important in providing an uncertainty for the most energetic jets in 13 TeV col-
2660 lisions.

2661

PART V

2662

SEARCH FOR LONG-LIVED PARTICLES

2663

You can put some informational part preamble text here.

2664

2665 LONG-LIVED PARTICLES IN ATLAS

2666 As discussed in Section 2.6, various limitations in the SM suggest a need for new
 2667 particles at the TeV scale. A wide range of extensions to the Standard Model
 2668 predict that these new particles can have lifetimes greater than approximately
 2669 one-hundredth of a nanosecond. These include theories with universal extra-
 2670 dimensions [51, 52], with new fermions [53], and with leptoquarks [54]. Many
 2671 SUSY theories also produce these Long-Lived Particles (LLPs), in both R-Parity
 2672 violating [55–57] and R-Parity conserving [58–61] formulations. Split super-
 2673 symmetry [62, 63], for example, predicts long-lived gluinos with O(TeV) masses.
 2674 This search focuses specifically on the SUSY case, but many of the results are
 2675 generic to any model with LLPs.

2676 Long-lived gluinos or squarks carry color-charge and will thus hadronize into
 2677 color neutral bound states called R-Hadrons. These are composit particles like
 2678 the usual hadrons but with one supersymmetric constituent, for example $\tilde{g}q\bar{q}$
 2679 and $\tilde{q}\bar{q}$. Through this hadronization process, the neutral gluino can acquire a
 2680 charge. Gluino pair production, $pp \rightarrow \tilde{g}\tilde{g}$ has the largest cross sectional increase
 2681 with the increase in energy to 13 TeV, and so this search focuses on gluino R-
 2682 Hadrons. Planned future updates will extend the case to explicitly include squark
 2683 and chargino models, but the method covers any long-lived, charged, massive
 2684 particle.

2685 10.1 EVENT TOPOLOGY

2686 The majority of SUSY models predict that gluinos will be produced in pairs at
 2687 the LHC, through processes like $pp \rightarrow q\bar{q} \rightarrow \tilde{g}\tilde{g}$ and $pp \rightarrow gg \rightarrow \tilde{g}\tilde{g}$, where the
 2688 gluon mode dominates for the collision energy and gluino masses considered
 2689 for this search. During their production, the long-lived gluinos hadronize into
 2690 color singlet bound states including $\tilde{g}q\bar{q}$, $\tilde{g}qqq$, and even $\tilde{g}g$ [64]. The probability
 2691 to form the gluon-only bound states is a free parameter usually taken to be 0.1,
 2692 while the meson states are favored among the R-Hadrons [65]. The charged and
 2693 neutral states are approximately equally likely for mesons, so the R-Hadrons will
 2694 be charged roughly 50% of the time.

2695 These channels produce R-Hadrons with large p_T , comparable to their mass,
 2696 so that they typically propagate with $0.2 < \beta < 0.9$ [65]. The fragmentation that
 2697 produces these hadrons is very hard, so the jet structure around the R-Hadron
 2698 is minimal, with less than 5 GeV of summed particle momentum expected in a
 2699 cone of $\Delta R < 0.25$ around the R-Hadron [65]. After hadronization, depending
 2700 on the gluino lifetime, the R-Hadrons then decay into hadrons and a LSP [64].

2701 In summary, the expected event for pair-produced long-lived gluinos is very
 2702 simple: two isolated, high-momentum R-Hadrons that propagate through the
 2703 detector before decaying into jets. The observable features of such events depend

2704 strongly on the interaction of the R-Hadron with the material of the detector and
 2705 also its lifetime. Section 10.1.1 describes the interactions of R-Hadrons which
 2706 reach the various detector elements in ATLAS and Section 10.1.2 provides a sum-
 2707 mary of the observable event descriptions for R-Hadrons of various lifetimes.

2708 10.11 DETECTOR INTERACTIONS

2709 After approximately 0.2 ns, the R-Hadron reaches the pixel detector. If charged,
 2710 it deposits energy into the material through repeated single collisions that result
 2711 in ionization of the silicon substrate [10]. Because of its comparatively low β ,
 2712 the ionization energy can be significantly greater than expected for SM particles
 2713 because the most-probable energy loss grows significantly as β decreases [10].
 2714 This large ionization can be measured through the ToT read out from the pixel
 2715 detector as described in Section 7.1.2. Large ionization in the inner detector is
 2716 one of the major characteristic features of LLPs.

2717 Throughout the next few nanoseconds, the R-Hadron propagates through the
 2718 remainder of the inner detector. A charged R-Hadron will provide hits in each
 2719 of these systems as would any other charged particle, and can be reconstructed
 2720 as a track. The track reconstruction provides a measurement of its trajectory
 2721 and thus its momentum as described in Section 7.1. The large momentum is
 2722 another characteristic feature of massive particles produced at the LHC. **Note: At**
2723 this point I am failing to mention that the TRT provides a possible dE/dx
2724 measurement, because no one uses it as far as I know.

2725 As of roughly 20 ns, the R-Hadron enters the calorimeter where it interacts
 2726 hadronically with the material. Because of its large mass and momentum, the
 2727 R-Hadron does not typically stop in the calorimeter, but rather deposits a small
 2728 fraction of its energy through repeated interactions with nucleons. The proba-
 2729 bility of interaction between the gluino itself and a nucleon is low because the
 2730 cross section drops off with the inverse square of its mass, so the interactions are
 2731 primarily governed by the light constituents [66]. Each of these interactions can
 2732 potentially change that quark content and thus change the sign of the R-Hadron,
 2733 so that the charge at exit is typically uncorrelated with the charge at entry [65].
 2734 The total energy deposited in the calorimeters during the propagation is small
 2735 compared to the kinetic energy of the R-Hadron, around 20-40 GeV, so that
 2736 E/p is typically less than 0.1 [65].

2737 Then, 30 ns after the collision, it reaches the muon system, where it again
 2738 ionizes in the material if charged and can be reconstructed as a muon track. Be-
 2739 cause of the charge-flipping interactions in the calorimeter, this track may have
 2740 the opposite sign of the track reconstructed in the inner detector, or there may
 2741 be a track present when there was none in the inner detector and vice-versa. The
 2742 propagation time at the typically lower β results in a significant delay compared
 2743 to muons, and that delay can be assessed in terms of a time-of-flight measure-
 2744 ment. Because of the probability of charge-flip and late arrival, there is a signif-
 2745 icant chance that an R-Hadron which was produced with a charge will not be
 2746 identified as a muon. The long time-of-flight is another characteristic feature of
 2747 R-Hadrons which are reconstructed as muons.

2748 10.1.2 LIFETIME DEPENDENCE

2749 The above description assumed a lifetime long enough for the R-Hadron to exit
 2750 the detector, which through this search is referred to as “stable”, even though
 2751 the particle may decay after exiting the detector. There are several unique sig-
 2752 natures at shorter lifetimes where the R-Hadron decays in various parts of the
 2753 inner detector; these lifetimes are referred to as “metastable”.

2754 The shortest case where the R-Hadron is considered metastable is for life-
 2755 times around 0.01 ns, where the particle decays before reaching any of the de-
 2756 tector elements. Although the R-Hadrons are produced opposite each other in
 2757 the transverse plane, each R-Hadron decays to a jet and an LSP. The LSPs are not
 2758 measured, so the produced jets can be significantly imbalanced in the transverse
 2759 plane which results in large missing energy. That missing energy can be used
 2760 to trigger candidate events, and provides the most efficient trigger option for
 2761 shorter lifetimes. Additionally, the precision of the tracking system allows the
 2762 displaced vertex of the R-Hadron decay to be reconstructed from the charged
 2763 particles in the jet. The distance of that vertex from the interaction point can
 2764 be used to distinguish R-Hadron decays from other processes. Figure 63 shows
 2765 a schematic diagram of an example R-Hadron event with such a lifetime. The
 2766 diagram is not to scale, but instead illustrates the detector interactions in the
 2767 pixel detector, calorimeters, and muon system. It includes a representation of
 2768 the charged R-Hadron and the neutral R-Hadron, as well as the LSPs and jets
 2769 (shown as charged hadrons) produced in the decay. Neutral hadrons may also
 2770 be produced in the decay but are not depicted. Previous searches on ATLAS have
 2771 used the displaced vertex to target LLP decays [67].

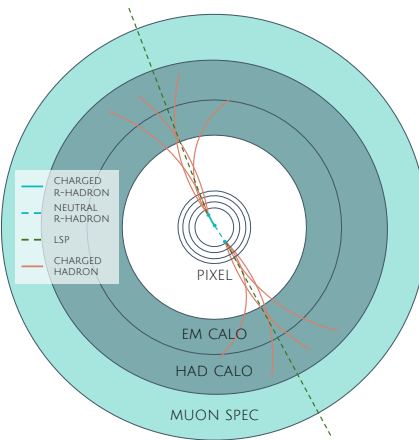


Figure 63: A schematic diagram of an R-Hadron event with a lifetime around 0.01 ns.
 The diagram includes one charged R-Hadron (solid blue), one neutral R-Hadron (dashed blue), LSPs (dashed green) and charged hadrons (solid orange). The pixel detector, calorimeters, and muon system are illustrated but not to scale.

2772 The next distinguishable case occurs at lifetimes greater than 0.1 ns, where
 2773 the R-Hadron forms a partial track in the inner detector. If the decay products
 2774 are sufficiently soft, they may not be reconstructed, and this forms a unique sig-

2775 nature of a disappearing track. An example of such an event is illustrated in
 2776 Figure 64, which shows the short track in the inner detector and the undetected
 2777 soft charged hadron and LSP that are produced. A dedicated search on ATLAS used
 2778 the disappearing track signature to search for LLP in Run 1 [68]. **zNote: might**
 2779 **not be worth mentioning the disappearing track here since it is actually a**
 2780 **chargino search, the soft pion is pretty unique to charginos.**

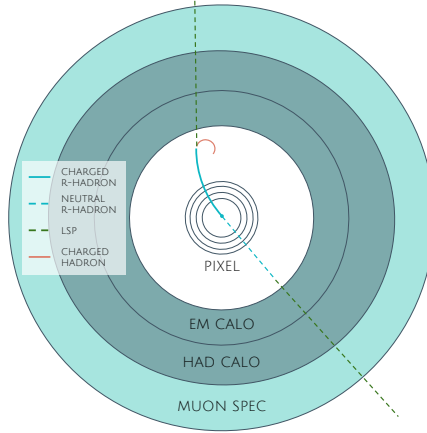


Figure 64: A schematic diagram of an R-Hadron event with a lifetime around 4 ns. The diagram includes one charged R-Hadron (solid blue), one neutral R-Hadron (dashed blue), LSPs (dashed green) and a charged hadron (solid orange). The pixel detector, calorimeters, and muon system are illustrated but not to scale.

2781 If the decay products are not soft, the R-Hadron daughters form jets, resulting
 2782 in an event-level signature of up to two high-momentum tracks, jets, and signif-
 2783 icant missing energy. The missing energy has the same origin as in the case of
 2784 0.01 ns lifetimes, from the decay to unmeasured particles, and again can be large.
 2785 The high-momentum tracks will also have the characteristically high-ionization
 2786 of massive, long-lived particles in the inner detector. Figure 65 illustrates an ex-
 2787 ample event with one charged R-Hadron which decays after approximately 10 ns,
 2788 and shows how the jets from the decay can still be reconstructed in the calorime-
 2789 ter. Several previous searches on ATLAS from Run 1 have used this signature to
 2790 search for R-Hadrons [69, 70], including a dedicated search for metastable parti-
 2791 cles [71].

2792 If the lifetime is longer than several nanoseconds, in the range of 15-30 ns,
 2793 the R-Hadron decay can occur in or after the calorimeters, but prior to reaching
 2794 the muon system. This case is similar to the above, although the jets may not be
 2795 reconstructed, and is covered by many of the same search strategies. The events
 2796 still often have large missing energy, although it is generated through different
 2797 mechanisms. The R-Hadrons do not deposit much energy in the calorimeters, so
 2798 a neutral R-Hadron will not enter into the missing energy calculation. A charged
 2799 R-Hadron opposite a neutral R-Hadron will thus generate significant missing en-
 2800 ergy, and close to 50% of pair-produced R-Hadron events fall into this category.
 2801 If both R-Hadrons are neutral then the missing energy will be low because nei-
 2802 ther is detected. Two charged R-Hadrons will also result in low missing energy
 2803 because both are reconstructed as tracks and will balance each other in the trans-

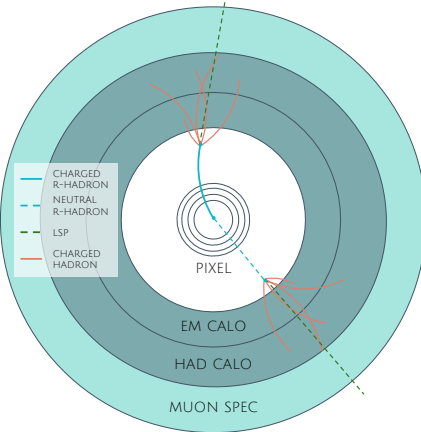


Figure 65: A schematic diagram of an R-Hadron event with a lifetime around 5 ns. The diagram includes one charged R-Hadron (solid blue), one neutral R-Hadron (dashed blue), LSPs (dashed green) and charged hadrons (solid orange). The pixel detector, calorimeters, and muon system are illustrated but not to scale.

2804 verse plane. A small fraction of the time, one of the charged R-Hadron tracks may
 2805 fail quality requirements and thus be excluded from the missing energy calcula-
 2806 tion and again result in significant missing energy. Figure 66 illustrates another
 2807 example event with one charged R-Hadron which decays after approximately 20
 2808 ns, and shows how the jets from the decay might not be reconstructed.

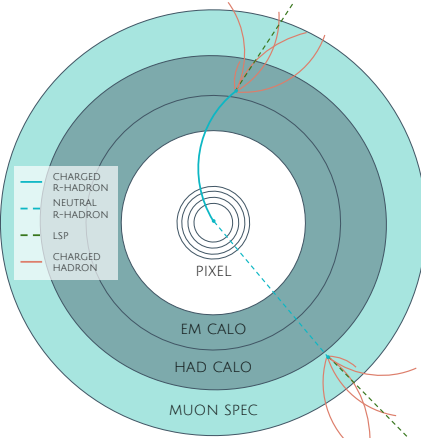


Figure 66: A schematic diagram of an R-Hadron event with a lifetime around 20 ns. The diagram includes one charged R-Hadron (solid blue), one neutral R-Hadron (dashed blue), LSPs (dashed green) and charged hadrons (solid orange). The pixel detector, calorimeters, and muon system are illustrated but not to scale.

2809 The longest lifetimes, the stable case, has all of the features of the 30-50 ns case
 2810 but with the addition of muon tracks for any R-Hadrons that exit the calorimeter
 2811 with a charge. That muon track can provide additional information from time-
 2812 of-flight measurements to help identify LSPs. An example of the event topology
 2813 for one charged and one neutral stable R-Hadron is shown in Figure 67. Some
 2814 searches on ATLAS have included this information to improve the search reach
 2815 for stable particles [70, 72].

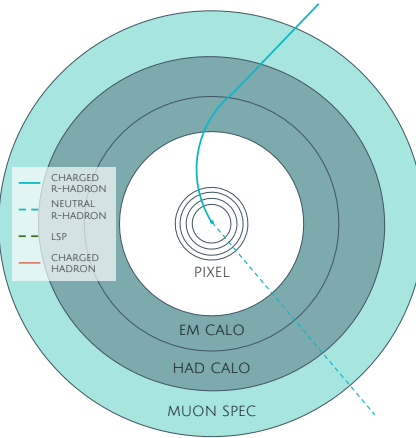


Figure 67: A schematic diagram of an R-Hadron event with a lifetime around 20 ns. The diagram includes one charged R-Hadron (solid blue) and one neutral R-Hadron (dashed blue). The pixel detector, calorimeters, and muon system are illustrated but not to scale.

2816 10.2 SIMULATION

2817 All of the event topologies discussed above are explored by simulations of R-
 2818 Hadron events in the [ATLAS](#) detector. A large number of such samples are gen-
 2819 erated to determine signal efficiencies, to measure expected yields, and to esti-
 2820 mate uncertainties. The primary interaction, pair production of gluinos with
 2821 masses between 400 and 3000 GeV, is simulated using [Pythia 6.4.27](#) [73]
 2822 with the AUET2B [74] set of tuned parameters for the underlying event and the
 2823 [CTEQ6L1](#) [48] PDF set. The simulated interactions include a modeling of pileup
 2824 by adding secondary, minimum bias interactions from both the same (in-time
 2825 pileup) and nearby (out-of-time pileup) bunch crossings. This event generation
 2826 is then augmented with a dedicated hadronization routine to hadronize the long-
 2827 lived gluinos into final states with R-Hadrons [75], with the probability to form
 2828 a gluon-gluino bound set at 10% [76].

2829 The cross sections used for these processes are calculated at next-to-leading
 2830 order ([NLO](#)) in the strong coupling constant with a resummation of soft-gluon
 2831 emmission at next-to-leading logarithmic ([NLL](#)) [77–81]. The nominal predic-
 2832 tions and the uncertainties for each mass point are taken from an envelope of
 2833 cross-section predictions using different PDF sets and factorization and renor-
 2834 malization scales [82].

2835 The R-Hadrons then undergo a full detector simulation [], where the interac-
 2836 tions of the R-Hadrons with the material of the detector are described by dedi-
 2837 cated [Geant4](#) [18] routines. These routines model the interactions described in
 2838 Section 10.1.1, including the ionizing interactions in the silicon modules of the
 2839 inner detector and the R-Hadron-nucleon interactions in the calorimeters [83,
 2840 84]. The specific routine chosen to describe the interactions of the R-Hadrons
 2841 with nucleons, the “generic model”, uses a pragmatic approach where the scatter-
 2842 ing cross section is taken to be a constant 12 mb per light quark. In this model

2843 the gluino itself does not interact at all except through its role as a reservoir of
2844 kinetic energy.

2845 The lifetimes of these R-Hadrons are then simulated at several working points,
2846 $\tau = 0.1, 1.0, 3.0, 10, 30, 50$ and detector stable, where the particle is required to
2847 decay after propagating for a time compatible with its lifetime. Only one decay
2848 mode is simulated for these samples, $\tilde{g} \rightarrow q\bar{q}\tilde{\chi}_1^0$ with the neutralino mass set to
2849 100 GeV, which is chosen because it has the highest sensitivity among all of the
2850 modes studied in previous searches [71]. Heavier neutralinos have similar results
2851 but generate less missing energy which reduces the efficiency of triggering.

2852 All of the simulated events are then reconstructed using the same software
2853 used for collision data. The fully reconstructed events are then reweighted to
2854 match the distribution of initial state radiation in an alternative sample of events,
2855 generated with MG5_aMC@NLO [85], which has a more accurate description of ra-
2856 diate effects than Pythia6. This reweighting provides a more accurate descrip-
2857 tion of the momentum of the gluino-gluino system and is important in modeling
2858 the efficiency of triggering and offline event selection.

2859

2860 EVENT SELECTION

2861 The [LLPs](#) targeted by this search differ in their interactions with the detector from
 2862 [SM](#) particles primarily because of their large mass. When produced at the ener-
 2863 gies available at the [LHC](#), that large mass results in a low β (typically $0.2 < \beta <$
 2864 0.9). Such slow-moving particles heavily ionize in detector material. Each layer
 2865 of the pixel detector provides a measurement of that ionization, through [ToT](#), as
 2866 discussed in Section 7.1.2. The ionization in the pixel detector, quantified in
 2867 terms of dE/dx , provides the major focus for this search technique, along with
 2868 the momentum measured in the entire inner detector. It is effective both for its
 2869 discriminating power and its use in reconstructing a particle's mass, and it can
 2870 be used for a wide range of masses and lifetimes as discussed in Section 10.1.2.
 2871 However dE/dx needs to be augmented with a few additional selection require-
 2872 ments to provide a mechanism for triggering and to further reduce backgrounds.

2873 Ionization itself is not currently accessible for triggering, so this search in-
 2874 stead relies on E_T^{miss} to trigger signal events. Although triggering on E_T^{miss} can
 2875 be inefficient, E_T^{miss} is often large for many production mechanisms of [LLPs](#), as
 2876 discussed in Section 10.1.

2877 The use of ionization to reject [SM](#) backgrounds relies on well-measured, high-
 2878 momentum tracks, so some basic requirements on quality and kinematics are
 2879 placed on the tracks considered in this search. These quality requirements have
 2880 been significantly enhanced in Run 2 by a newly introduced tracking variable
 2881 that is very effective in removing highly-ionizing backgrounds caused by over-
 2882 lapping tracks. A few additional requirements are placed on the tracks consid-
 2883 ered for [LLP](#) candidates that increase background rejection by targeting specific
 2884 types of [SM](#) particles. These techniques provide a significant analysis improve-
 2885 ment over previous iterations of ionization-based searches on ATLAS by provid-
 2886 ing additional background rejection with minimal loss in signal efficiency.

2887 The ionization measurement with the Pixel detector can be calibrated to pro-
 2888 vide an estimator of $\beta\gamma$. That estimate, together with the momentum measure-
 2889 ment provided by tracking, can be used to reconstruct a mass for each track
 2890 which traverses the pixel detector. That mass variable will be peaked at the [LLP](#)
 2891 mass for any signal, and provides an additional tool to search for an excess. In
 2892 addition to an explicit requirement on ionization, this search constructs a mass-
 2893 window for each targeted signal mass in order to evaluate any excess of events
 2894 and to set limits.

2895 The strategy discussed here is optimized for lifetimes of $O(1) - O(10)$ ns.
 2896 Pixel ionization is especially useful in this regime as particles only need to prop-
 2897 agate through the first seven layers of the inner detector, about 37 cm from the
 2898 beam axis. The search is still competitive with other searches for [LLPs](#) at longer
 2899 lifetimes, because the primary discriminating variables are still applicable even
 2900 for particles that do not decay within the detector [72]. Although the majority of

2901 the requirements will be the same for all lifetimes, two signal regions are defined
 2902 to optimize separately for intermediate and long lifetime particles.

2903 11.1 TRIGGER

2904 Triggering remains a significant difficulty in defining an event selection with
 2905 high signal efficiency in a search for LLPs. There are no triggers available in
 2906 the current ATLAS system that can fire directly from a high momentum track
 2907 with large ionization (Section 6.6). Although in some configurations a charged
 2908 LLP can fire muon triggers, this requirement introduces significant model depen-
 2909 dence on both the allowed lifetimes and the interactions in the calorimeter [65],
 2910 as discussed in Section 10.1.1.

2911 For a search targeting particles which may decay prior to reaching the muon
 2912 system, the most efficient available trigger is based on missing energy [65]. As
 2913 discussed in Section 10.1, signal events can produce significant E_T^{miss} by a few
 2914 mechanisms. At the trigger level however, the missing energy is only calculated
 2915 using the calorimeters (Section 6.6) where the R-Hadrons deposit little energy.
 2916 So, at short lifetimes, E_T^{miss} measured in the calorimeter is generated by an im-
 2917 balance between the jets and undetected LSPs produced in R-Hadron decays. At
 2918 longer lifetimes, without the decay products, missing energy is only produced in
 2919 the calorimeters when the R-Hadrons recoil against an initial state radiation (ISR)
 2920 jet.

2921 These features are highlighted in Figure 68, which shows the E_T^{miss} distribu-
 2922 tions for simulated short lifetime (3 ns) and stable R-Hadron events. The figure
 2923 includes both the offline E_T^{miss} , the missing energy calculated with all available
 2924 information, and Calorimeter E_T^{miss} , the missing energy calculated using only
 2925 information available at the calorimeter which approximates the missing energy
 2926 available at the trigger. The short lifetime sample has significantly greater E_T^{miss}
 2927 and Calorimeter E_T^{miss} than the stable sample as expected. For the stable sam-
 2928 ple, a small fraction of events with very large E_T^{miss} (about 5%) migrate into the
 2929 bin with very small Calorimeter E_T^{miss} because the E_T^{miss} produced by a charged
 2930 R-Hadron track opposite a neutral R-Hadron track does not contribute any miss-
 2931 ing energy in the calorimeters.

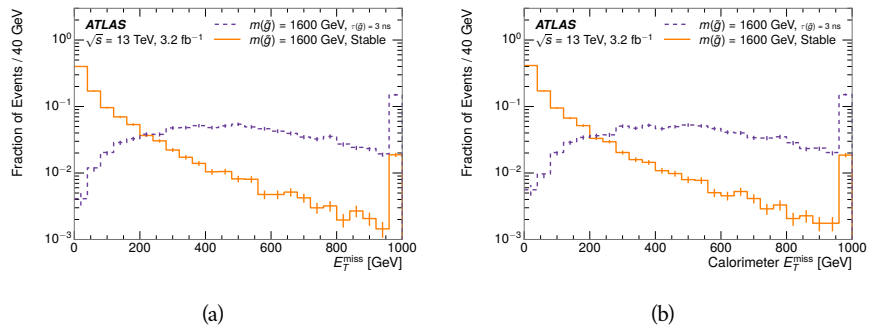


Figure 68: The distribution of (a) E_T^{miss} and (b) Calorimeter E_T^{miss} for simulated signal events before the trigger requirement.

2932 So, either case to some extent relies on kinematic degrees of freedom to pro-
 2933 duce missing energy, as the pair-produced LLPs tend to balance each other in
 2934 the transverse plain. That balance results in a relatively low efficiency for long-
 2935 lifetime particles, roughly 40%, and efficiencies between 65% and 95% for shorter
 2936 lifetimes depending on both the mass and the lifetime. For long lifetimes in par-
 2937 ticular, the presence of ISR is important in providing an imbalance in the trans-
 2938 verse plane, and is an important aspect of modeling the selection efficiency for
 2939 R-Hadron events.

2940 The missing energy trigger with the lowest threshold available is chosen for
 2941 this selection in order to maximize the trigger efficiency. During 2015 data col-
 2942 lection this was the HLT_xe70 trigger, which used a 50 GeV threshold on miss-
 2943 ing energy at LVL1 and a 70 GeV threshold on missing energy at the HLT. These
 2944 formation of the trigger decision for missing energy was discussed in more detail
 2945 in Section 6.6.

2946 11.2 KINEMATICS AND ISOLATION

2947 After the trigger requirement, each event is required to have a primary vertex
 2948 reconstructed from at least two well-measured tracks in the inner detector, each
 2949 with $p_T > 400$ MeV. If more than one such vertex exists, the primary vertex
 2950 is taken to be the one with the largest summed track momentum for all tracks
 2951 associated to that vertex. The offline reconstructed E_T^{miss} is required to be above
 2952 130 GeV to additionally reject SM backgrounds. The transverse missing energy
 2953 is calculated using fully reconstructed and calibrated offline objects, as described
 2954 in Section 7.5. In particular the E_T^{miss} definition in this selection uses jets recon-
 2955 structed with the anti- k_t algorithm with radius $R = 0.4$ from clusters of energy
 2956 in the calorimeter (Section 7.4) and with $p_T > 20$ GeV, as well as reconstructed
 2957 muons, electrons, and tracks not identified as another object type.

2958 The E_T^{miss} distributions are shown for data and a few simulated signals in Fig-
 2959 ure 69, after the trigger requirement. The cut placed at 130 GeV is 95% effi-
 2960 cient for metastable and 90% efficient for stable particles, after the trigger re-
 2961 quirement, because of the missing energy generating mechanisms discussed pre-
 2962 viously. The distribution of data in this figure and subsequent figures in this sec-
 2963 tion can be interpreted as the distribution of backgrounds, as any signal contam-
 2964 ination would be negligible if present at these early stages of the selection (prior
 2965 to the final requirement on ionization). The background falls rapidly with miss-
 2966 ing energy, motivating the direct requirement on E_T^{miss} for the signal region. Al-
 2967 though a tighter requirement than the specified value of 130 GeV would seem to
 2968 increase the search potential from these early distributions, other requirements
 2969 are more optimal when taken as a whole. The specific values for each require-
 2970 ment in signal region were optimized considering the increase in discovery reach
 2971 for tightening the requirement on each discriminating variable. **NOTE: If space**
 2972 **and time permit, I will add a whole section about signal region optimiza-**
 2973 **tion..**

2974 It is typically the practice for searches for new physics on ATLAS to place an
 2975 offline requirement on the triggering variable that is sufficiently tight to guar-

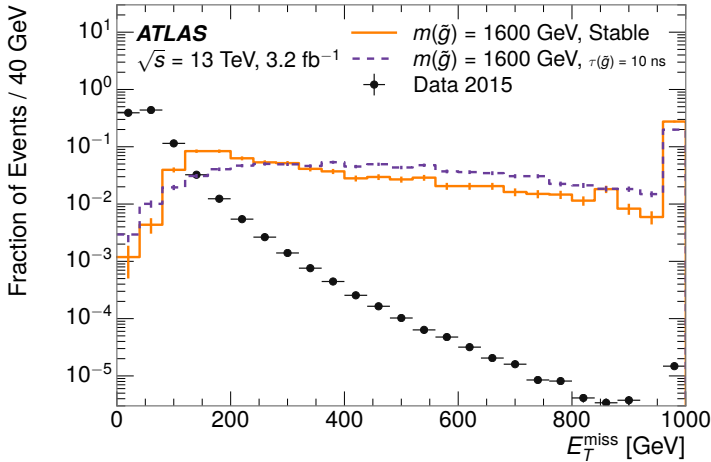


Figure 69: The distribution of E_T^{miss} for data and simulated signal events, after the trigger requirement.

2976 antee that the event would pass the trigger. Such a tight requirement makes the
 2977 uncertainty on the trigger efficiency of the simulation negligible, as modeling the
 2978 regime where the trigger is only partially efficient can be difficult. In this analy-
 2979 sis, however, because of the atypical interactions of R-Hadrons with the tracker
 2980 and the calorimeter, the offline requirement on E_T^{miss} is not sufficient to guar-
 2981 antee a 100% trigger efficiency even at large values, as can be seen in Figure 70.
 2982 This figure shows the efficiency for passing the HLT_xe70 trigger as a function
 2983 of the requirement on E_T^{miss} , which plateaus to roughly 85% even at large values.
 2984 This plateau does not reach 100% because events which have large offline miss-
 2985 ing energy from a neutral R-Hadron produced opposite of a charged R-Hadron
 2986 can have low missing energy in the calorimeters. The Calorimeter E_T^{miss} , on the
 2987 other hand, does not have this effect and reaches 100% efficiency at large values
 2988 because it is the quantity that directly corresponds to the trigger threshold. In
 2989 both cases the efficiency of triggering is greater for the short lifetime sample be-
 2990 cause the late decays to hadrons and LSPs produce an imbalance in the calorime-
 2991 ters even though they may not be reconstructed offline as tracks or jets. For this
 2992 reason, the requirement on E_T^{miss} is determined by optimizing the background
 2993 rejection even though it corresponds to a value of trigger efficiency significantly
 2994 below 1.0.

2995 Potential signal events are then required to have at least one candidate LLP
 2996 track. Although the LLPs are produced in pairs, many models do not consistently
 2997 yield two charged particles. For example, in the R-Hadron model highlighted
 2998 here, only 20% of events have two charged R-Hadrons while 47% of events have
 2999 just one. A signal region requiring two charged candidates could be a powerful
 3000 improvement in background rejection for a larger dataset, but it is not consid-
 3001 ered in this version of the analysis as it was found to be unnecessary to reject the
 3002 majority of backgrounds.

3003 For a track to be selected as a candidate, it must have $p_T > 50 \text{ GeV}$ and pass
 3004 basic quality requirements. The track must be associated to the primary vertex.

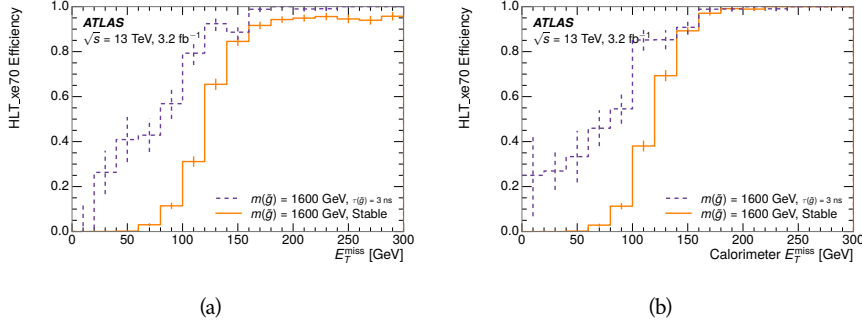


Figure 70: The trigger efficiency for the HLT_xe70 trigger requirement as a function of (a) E_T^{miss} and (b) Calorimeter E_T^{miss} for simulated signal events.

It must also have at least seven clusters in the silicon layers in the inner detector to ensure an accurate measurement of momentum. Those clusters must include one in the innermost layer if the extrapolated track is expected to pass through that layer. And to ensure a reliable measurement of ionization, the track is required to have at least two clusters in the pixel detector that provide a measurement of dE/dx .

At this point in the selection, there is a significant high-ionization background from multiple tracks that significantly overlap in the inner detector. Previous version of this analysis have rejected these overlaps by an explicit overlap rejection between pairs of fully reconstructed tracks, typically by requiring no additional tracks within a cone around the candidate. This technique, however, fails to remove the background from tracks that overlap so precisely that the tracks cannot be separately resolved, which can be produced in very collimated photon conversions or decays of pions.

A new method, added in Run 2, identifies cluster shapes that are likely formed by multiple particles based on a neural network classification algorithm. The number of clusters that are classified this way in the pixel detector for a given track is called N_{split} . As the shape of clusters requires significantly less spatial separation to identify overlaps than it does to reconstruct two fully resolved tracks, this variable is more effective at rejecting backgrounds from overlaps. Figure 71 shows the dependence of ionization on N_{split} ; as N_{split} increases the most probable value of dE/dx grows significantly up to twice the expected value when $N_{\text{split}} = 4$.

This requirement is very successful in reducing the long positive tail of the dE/dx distributions, as can be seen in Figure 72. Comparing the distribution for “baseline tracks”, tracks with only the above requirements on clusters applied and before the requirement on N_{split} , to the distribution with $N_{\text{split}} = 0$, it is clear that the fraction of tracks with large dE/dx is reduced by several orders of magnitude. The tracks without split hits are very close to the dE/dx distribution of identified muons, which are extremely well isolated on average. Figure 72 also includes the distribution of dE/dx in an example signal simulation to demonstrate how effective dE/dx is as a discriminating variable with this isolation applied. The background falls rapidly for $dE/dx > 1.8 \text{ MeVg}^{-1}\text{cm}^2$

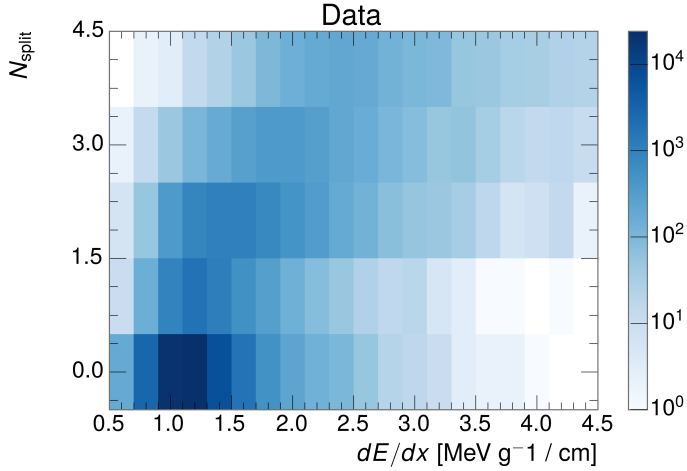


Figure 71: The dependence of dE/dx on N_{split} in data after basic track hit requirements have been applied.

3038 while the majority of the signal, approximately 90% depending on the mass, falls
 3039 above that threshold. Over 90% of LLP tracks in simulated signal events pass the
 3040 N_{split} -based isolation requirement.

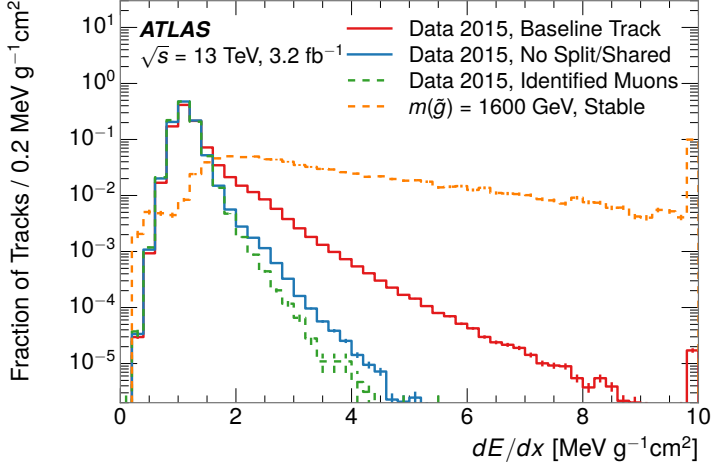


Figure 72: The distribution of dE/dx with various selections applied in data and simulated signal events.

3041 A few additional kinematic requirements are imposed to help reduce SM back-
 3042 grounds. The momentum of the candidate track must be at least 150 GeV, and
 3043 the uncertainty on that measurement must be less than 50%. The distribution of
 3044 momentum is shown in Figure 73 for tracks in data and simulated signal events
 3045 after the previously discussed requirements on clusters, transverse momentum,
 3046 and isolation have been imposed. The signal particles are much harder on aver-

age than their backgrounds because of the high energy interactions required to produce them. The transverse mass, M_T , defined as

$$M_T = \sqrt{2p_T E_T^{\text{miss}}(1 - \cos(\Delta\phi(E_T^{\text{miss}}, \text{track})))} \quad (20)$$

estimates the mass of a decay of to a single charged particle and an undetected particle and is required to be greater than 130 GeV to reject contributions from the decay of W bosons. Figure 74 shows the distribution of M_T for data and simulated signal events. The signal is distributed over a wide range of M_T , with about 90% above the threshold value of 130 GeV. The data shows a dual-peaked structure, where the first peak comes from W boson decays and the second peak is a kinematic shaping from the requirements on E_T^{miss} and the track p_T in dijet events.

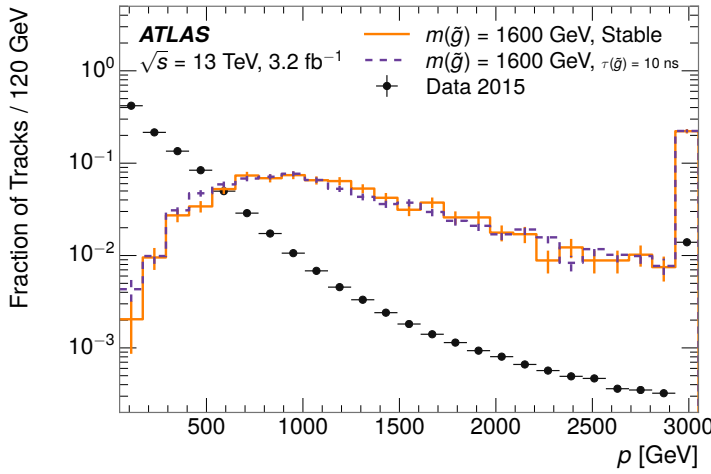


Figure 73: The distribution of track momentum for data and simulated signal events, after previous selection requirements have been applied.

11.3 PARTICLE SPECIES REJECTION

The amount of ionization deposited by particles with low mass and high momentum has a large positive tail [10], so backgrounds can be formed by a wide variety of SM processes when various charged particles have a few randomly large deposits of energy in the pixel detector. Those backgrounds can be additionally reduced by targeting other interactions with the detector where they are expected to have different behavior than R-Hadrons. The interactions with the detector depend on the types of particles produced rather than the processes which produce them, so this search forms a series of rejections to remove backgrounds from individual particle species. These rejections focus on using additional features of the event, other than the kinematics of the candidate track, as they can provide a powerful source of background rejection with very high signal efficiency. However, the lifetime of an R-Hadron can significantly change its

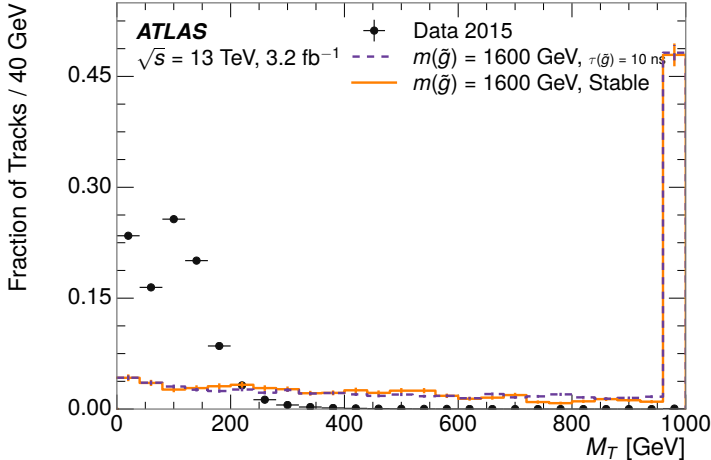


Figure 74: The distribution of M_T for data and simulated signal events, after previous selection requirements have been applied.

3070 detector characteristics, as discussed in Section 10.1.2. To accommodate these
 3071 differences, the SM rejections defined in this section are split to form two signal
 3072 regions, one for long-lifetimes particles, the stable region ($50 \leq \tau[\text{ns}] < \infty \text{ ns}$),
 3073 and one for intermediate lifetime particles, the metastable region ($0.4 < \tau[\text{ns}] <$
 3074 50).

3075 Jets can be very effectively rejected by considering the larger-scale isolation of
 3076 the candidate track. In this case the isolation focuses on the production of nearby
 3077 particles as a jet-veto, rather than the isolation from overlapping tracks based on
 3078 N_{split} that was used to reduce high-ionization backgrounds. As explained in Sec-
 3079 tion 10.1, the fragmentation process which produces an R-Hadron is very hard
 3080 and thus is not expected to produce additional particles with a summed momen-
 3081 tum of more than 5 GeV. The jet-veto uses the summed momentum of tracks
 3082 with a cone of $\Delta R < 0.25$, referred to as p_T^{Cone} , which is shown in Figure 75 for
 3083 data and simulated signal events. In the data this value has a peak at zero from
 3084 isolated tracks such as leptons, and a long tail from jets which contains as much
 3085 as 80% of the background above 20 GeV at this stage of the selection. In signal
 3086 events p_T^{Cone} is strongly peaked at zero and significantly less than 1% of signal
 3087 events have p_T^{Cone} above 20 GeV. This makes a requirement of $p_T^{\text{Cone}} < 20 \text{ GeV}$
 3088 a very effective method to reject background without losing signal efficiency.
 3089 For the stable signal region, this cut is further tightened to $p_T^{\text{Cone}} < 5 \text{ GeV}$ as
 3090 it is the most effective variable remaining to extend the search reach for long
 3091 lifetimes.

3092 Even for fully isolated particles, there are additional methods to reject each
 3093 type of particle using information in the muon system and calorimeters. Muons
 3094 can be identified very reliably using the tracks in the muon system, as described
 3095 in Section 7.3. For intermediate lifetimes the LLPs do not survive long enough
 3096 to reach the muon system, and so muons are vetoed by rejecting tracks that as-
 3097 sociate to a muon with medium muon identification requirements (Section 7.3).
 3098 For longer lifetimes, this rejection is not applied because LLPs which reach the

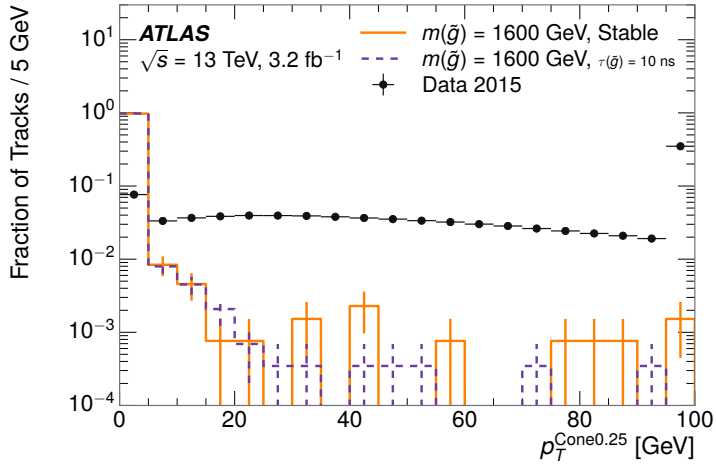


Figure 75: The distribution of summed tracked momentum within a cone of $\Delta R < 0.25$ around the candidate track for data and simulated signal events, after previous selection requirements have been applied.

3099 muon system can be identified as muons as often as 30% of the time in simulated
 3100 samples.

3101 Calorimeter-based particle rejection relies on the expected small deposits of
 3102 energy from LLPs. When the lifetime is long enough to reach the calorimeter, a
 3103 LLP deposits little of its energy as it traverses the material, as discussed in Sec-
 3104 tion 10.1. Even when the particle does decay before the calorimeter, the major-
 3105 ity of its energy is carried away by the LSP and not deposited in the calorimeter.
 3106 In both cases the energy is expected to be distributed across the layers of the
 3107 calorimeters and not peaked in just one layer. This can be quantified in terms
 3108 of E/p , the ratio of calorimeter energy of a nearby jet to the track momentum,
 3109 and f_{EM} , the fraction of energy in that jet within the electromagnetic calorime-
 3110 ter. When no jets fall within a cone of 0.05 of the particle, E/p and f_{EM} are both
 3111 defined as zero. E/p is expected to be above 1.0 for typical SM particles because
 3112 of calibration and the contributions from other nearby particles, as discussed in
 3113 Chapter 8. At these momenta there is no significant zero fraction due to inter-
 3114 actions with the detector or insufficient energy deposits (see Section 8.2.2). f_{EM}
 3115 is peaked close to 1.0 for electrons, and distributed between 10% and 90% for
 3116 hadrons.

3117 These trends can be seen in the two dimensional distribution for signal in
 3118 Figure 76 for stable and metastable (10 ns) events. The majority of R-Hadrons
 3119 in both samples fall into the bin for $E/p = 0$ and $f_{\text{EM}} = 0$ because the majority
 3120 of the time there is no associated jet. In the stable sample, when there often is
 3121 an associated jet, E/p is typically still below 0.1, and the f_{EM} is predominantly
 3122 under 0.8. In the metastable sample, on the other hand, E/p is larger but still
 3123 typically below 0.1 because of actual jets produced during the decay. The f_{EM} is
 3124 much lower on average in this case, below 0.1, because the 10 ns lifetime particles
 3125 rarely decay before passing through the electromagnetic calorimeter. Figure 76
 3126 also includes simulated Z decays to electrons or tau leptons. From the decays

3127 to electrons it is clear that the majority of electrons have f_{EM} above 0.9. The
 3128 tau decays include a variety of products. Muons can be seen in the bin where
 3129 $E/p = 0$ and $f_{\text{EM}} = 0$ because they do not have an associated jet. Electrons fall
 3130 into the range where $E/p > 1$ and $f_{\text{EM}} > 0.9$. Hadronic tau decays are the most
 3131 common, and fall in the range of $0.1 < f_{\text{EM}} < 0.9$ and $E/p > 1.0$.

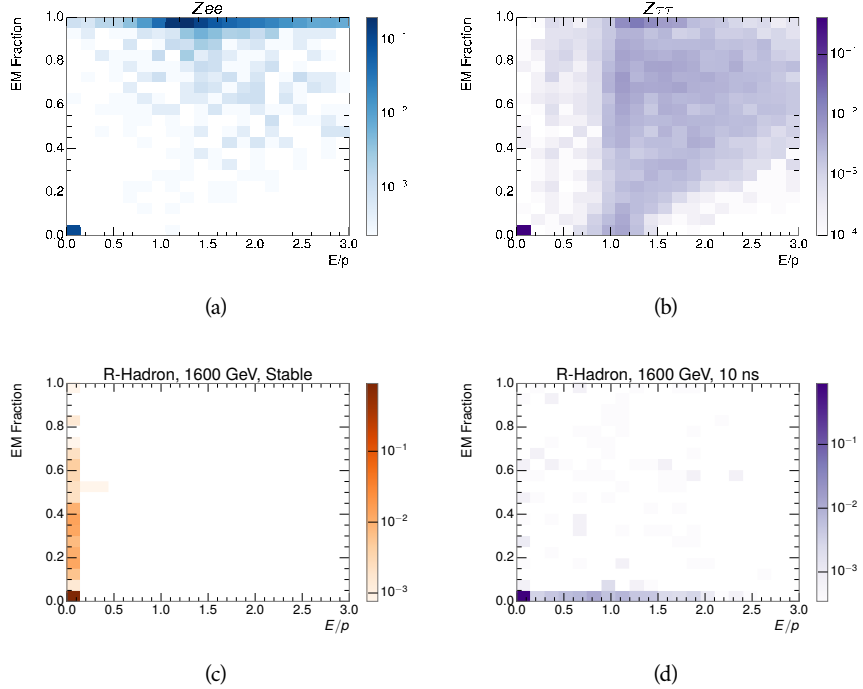


Figure 76: The normalized, two-dimensional distribution of E/p and f_{EM} for simulated
 (a) $Z \rightarrow ee$, (b) $Z \rightarrow \tau\tau$, (c) 1200 GeV Stable R-Hadron events, and (d) 1200
 GeV, 10 ns R-Hadron events.

3132 These differences motivate an electron rejection by requiring an f_{EM} below
 3133 0.9. Similarly, isolated hadrons are rejected by requiring $E/p < 1.0$. These re-
 3134 quirements combine to remove the majority of isolated electrons and hadrons
 3135 but retain over 95% of the simulated signal across a range of masses and lifetimes.

3136 11.4 IONIZATION

3137 The final requirement on the candidate track is the primary discriminating vari-
 3138 able, the ionization in the pixel detector. That ionization is measured in terms
 3139 of dE/dx , which was shown for data and simulated signal events in Figure 72.
 3140 dE/dx is dramatically greater for the high mass signal particles than the back-
 3141 grounds, which start to fall immediately after the minimally ionizing peak at 1.1
 3142 $\text{MeV g}^{-1} \text{cm}^2$. The dE/dx for candidate tracks must be greater than a pseudorapidity-
 3143 dependent threshold, specifically $1.80 - 0.11|\eta| + 0.17\eta^2 - 0.05\eta^3 \text{ MeV g}^{-1} \text{ cm}^{-2}$,
 3144 in order to correct for an approximately 5% dependence of the MIP peak on η .
 3145 The requirement was chosen as part of the signal region optimization, and man-

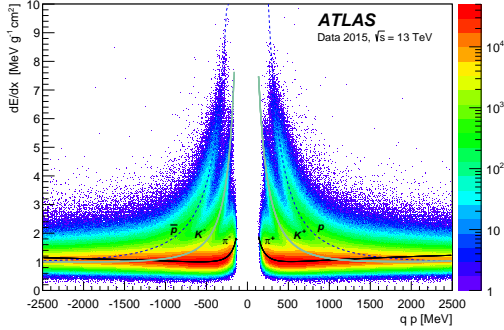


Figure 77: Two-dimensional distribution of dE/dx versus charge signed momentum (qp) for minimum-bias tracks. The fitted distributions of the most probable values for pions, kaons and protons are superimposed.

ages to reduce the backgrounds by a factor of 100 while remaining 70-90% efficient for simulated signal events depending on the mass.

11.4.1 MASS ESTIMATION

The mean value of ionization in silicon is governed by the Bethe equation and the most probable value follows a Landau-Vavilov distribution [10]. Those forms inspire a parametric description of dE/dx in terms of $\beta\gamma$,

$$(dE/dx)_{MPV}(\beta\gamma) = \frac{p_1}{\beta^{p_3}} \ln(1 + [p_2 \beta\gamma]^{p_5}) - p_4 \quad (21)$$

which performs well in the range $0.3 < \beta\gamma < 1.5$. This range includes the expected range of $\beta\gamma$ for the particles targeted for this search, with $\beta\gamma \approx 2.0$ for lower mass particles ($O(100 \text{ GeV})$) and up to $\beta\gamma \approx 0.5$ for higher mass particles ($O(1000 \text{ GeV})$). The parameters, p_i , are fit using a 2015 data sample of low-momentum pions, kaons, and protons as described in Ref. [86]. Figure 77 shows the two-dimensional distribution of dE/dx and momentum along with the above fitted values for $(dE/dx)_{MPV}$.

The above equation (21) is then numerically inverted to estimate $\beta\gamma$ and the mass for each candidate track. In simulated signal events, the mean of this mass value reproduces the generated mass up to around 1800 GeV to within 3%, and 3% shift is applied to correct for this difference. The mass distributions prior to this correction are shown for a few stable mass points in Figure 78. The large widths of these distributions come from the high variability in energy deposits in the pixel detector as well as the uncertainty on momentum measurements at high momentum, but the means converge to the expected values.

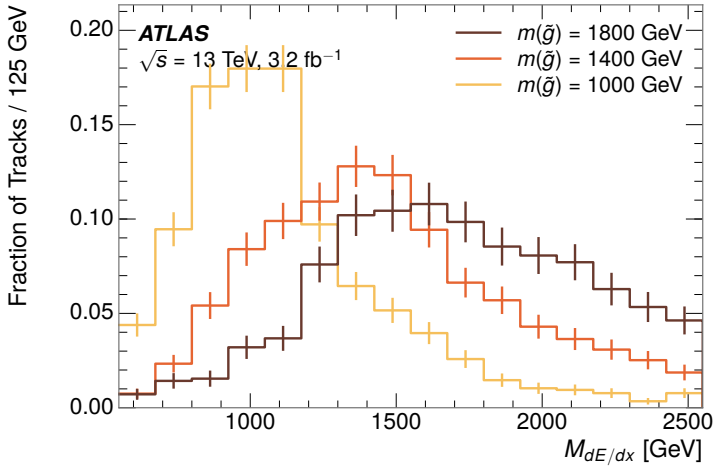


Figure 78: The distribution of mass estimated using dE/dx for simulated stable R-Hadrons with masses between 1000 and 1600 GeV.

This analysis evaluates expected yields and the resulting cross sectional limits using windows in this mass variable. The windows are formed by fitting mass distributions in simulated signal events like those in Figure 78 to Gaussian distributions and taking all events that fall within $\pm 1.4\sigma$ of the mean. As can be seen in Figure 78, typical values for this width are $\sigma \approx 300 - 500$ GeV depending on the generated mass.

11.5 EFFICIENCY

The numbers of events passing each requirement through ionization are shown in Table 9 for the full 2015 dataset and a simulated 1600 GeV, 10 ns lifetime R-Hadron sample. The table highlights the overall acceptance \times efficiency for signal events, which for this example is 19%. Between SM rejection and ionization, this signal region reduces the background of tracks which pass the kinematic requirements down by an additional factor of almost 2000.

There is a strong dependence of this efficiency on lifetime and mass, with efficiencies dropping to under 1% at low lifetimes. Figure 79 shows the dependence on both mass and lifetime for all signal samples considered in this search. The dependence on mass is relatively slight and comes predominantly from the increasing fraction of R-Hadrons which pass the ionization cut with increasing mass. The trigger and E_T^{miss} requirements are most efficient for particles that decay before reaching the calorimeters. However, the chance of a particle to be reconstructed as a high-quality track decreases significantly at low lifetimes as the particle does not propagate sufficiently through the inner detector. These effects lead to a maximum in the selection efficiency for lifetimes around 10-30 ns.

The inefficiency of this signal region at short lifetimes comes almost exclusively from an acceptance effect, in that the particles do not reach the necessary

Selection	Exp. Signal Events	Observed Events in 3.2 fb^{-1}
Generated	26.0 ± 0.3	
E_T^{miss} Trigger	24.8 ± 0.3 (95%)	
$E_T^{\text{miss}} > 130 \text{ GeV}$	23.9 ± 0.3 (92%)	
Track Quality and $p_T > 50$	10.7 ± 0.2 (41%)	368324
Isolation Requirement	9.0 ± 0.2 (35%)	108079
Track $p > 150 \text{ GeV}$	6.6 ± 0.2 (25%)	47463
$M_T > 130 \text{ GeV}$	5.8 ± 0.2 (22%)	18746
Electron and Hadron Veto	5.5 ± 0.2 (21%)	3612
Muon Veto	5.5 ± 0.2 (21%)	1668
Ionization Requirement	5.0 ± 0.1 (19%)	11

Table 9: The expected number of events at each level of the selection for metastable 1600 GeV , 10 ns R-Hadrons, along with the number of events observed in data, for 3.2 fb^{-1} . The simulated yields are shown with statistical uncertainties only. The total efficiency \times acceptance is also shown for the signal.

3193 layers of the SCT. This can be seen more clearly by defining a fiducial region
 3194 which includes events with at least one R-Hadron that is produced with non-
 3195 zero charge, $p_T > 50 \text{ GeV}$, $p > 150 \text{ GeV}$, $|\eta| < 2.5$, and a decay distance greater
 3196 than 37 cm in the transverse plane. At short (1 ns) lifetimes, the acceptance into
 3197 this region is as low as 4%. Once this acceptance is accounted for, the selection
 3198 efficiency ranges from 25% at lifetimes of 1 ns up to 45% at lifetimes of 10 ns.

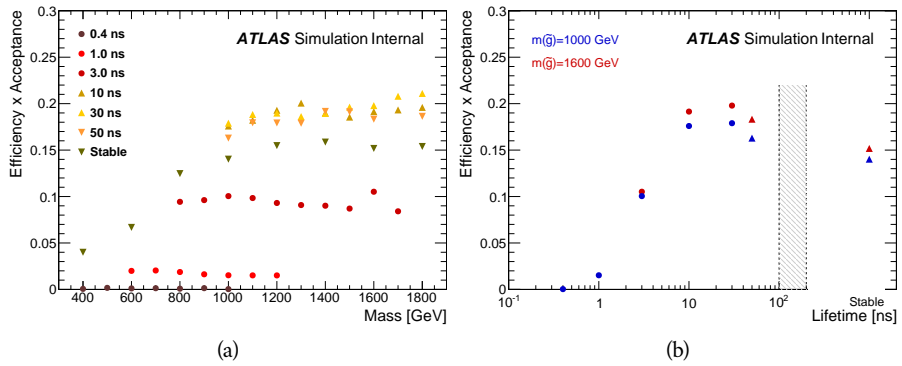


Figure 79: The acceptance \times efficiency as a function of R-Hadron (a) mass and (b) lifetime. (a) shows all of the combinations of mass and lifetime considered in this search, and (b) highlights the lifetime dependence for 1000 GeV and 1600 GeV R-Hadrons.

3199

3200 BACKGROUND ESTIMATION

3201 The event selection discussed in the previous section focuses on detector sig-
 3202 natures, emphasizing a single high-momentum, highly-ionizing track. That track
 3203 is then required to be in some way inconsistent with the expected properties
 3204 of SM particles, with various requirements designed to reject jets, hadrons,
 3205 electrons, and muons (Section 11.3). Therefore the background for this search comes
 3206 entirely from reducible backgrounds that are outliers of various distributions in-
 3207 cluding dE/dx , f_{EM} , and p_T^{Cone} . The simulation can be tuned in various ways to
 3208 do an excellent job of modeling the average properties of each particle type [87],
 3209 but it is not necessarily expected to accurately reproduce outliers. For this rea-
 3210 sons, the background estimation used for this search is estimated entirely using
 3211 data.

3212 12.1 BACKGROUND SOURCES

3213 SM charged particles with lifetimes long enough to form tracks in the inner de-
 3214 tector can be grouped into three major categories based on their detector inter-
 3215 actions: hadrons, electrons, and muons. Every particle that enters into the back-
 3216 ground for this search belongs to one of these types. Relatively pure samples of
 3217 tracks from each of these types can be formed in data by inverting the various
 3218 rejection techniques in Section 11.3. Specifically, muons are selected requiring
 3219 medium muon identification, electrons requiring $E/p > 1.0$ and $f_{\text{EM}} > 0.95$,
 3220 and hadrons requiring $E/p > 1.0$ and $f_{\text{EM}} < 0.95$.

3221 Figure 80 shows the distributions of momentum and dE/dx for these cate-
 3222 gories in data, after requiring the event level selection as well as the track re-
 3223 quirements on p_T , hits, and N_{split} , as discussed in Section 11.2. Simulated signal
 3224 events are included for reference. These distribution are only illustrative of the
 3225 differences between types, as the rejection requirements could alter their shape.
 3226 This is especially significant for momentum which enters directly into E/p and
 3227 can indirectly affect muon identification. However the various types show clear
 3228 differences in both distributions. The distributions of momentum are not nec-
 3229 cessarily expected to match between the various types because the production
 3230 mechanisms for each type result in different kinematic distributions. dE/dx is
 3231 also different between types because of incomplete isolation; although the re-
 3232 quirement on N_{split} helps to reduce the contribution of nearby particles it does
 3233 not completely remove the effect of overlaps. Muons are better isolated because
 3234 they do not have the additional particle from hadronization present for hadrons
 3235 and they are significantly less likely do interact with the detector and produce
 3236 secondary particles compared to hadrons and electrons. Thus muons have the
 3237 smallest fraction of dE/dx above the threshold of $1.8 \text{ MeVg}^{-1}\text{cm}^2$; hadrons and
 3238 electrons have a larger fraction above this threshold.

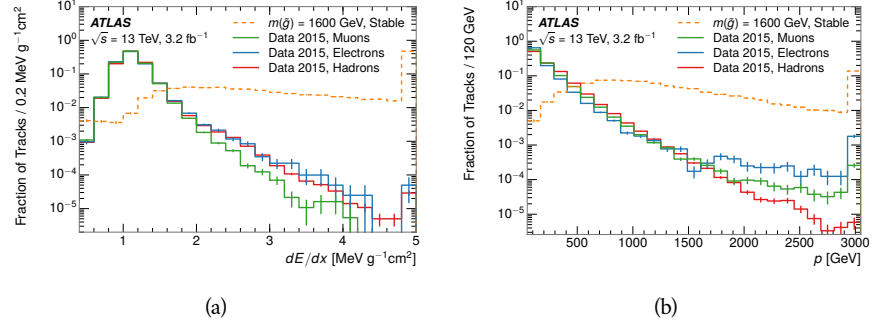


Figure 80: The distribution of (a) dE/dx and (b) momentum for tracks in data and simulated signal after requiring the event level selection and the track selection on p_T , hits, and N_{split} . Each sub-figure shows the normalized distributions for tracks classified as hadrons, electrons, and muons in data and R-Hadrons in the simulated signal.

3239 It is difficult to determine what fraction of each particle type enters into the fi-
 3240 nal signal region. The background method will not have significant dependence
 3241 on the relative contributions of each species, but it is useful to understand the
 3242 differences between each when considering the various tests of the method.

3243 12.2 PREDICTION METHOD

3244 The data-driven background estimation relies on the independence between ion-
 3245 ization and other kinematic variables in the event. For standard model particles
 3246 with momenta above 50 GeV, dE/dx is not correlated with momentum; though
 3247 there is a slight relativistic rise as momentum increases, the effect is small com-
 3248 pared to the width of the distribution of ionization energy deposits.. So, the
 3249 proposed method to estimate the mass distribution of the signal region is to use
 3250 momentum from a track with low dE/dx (below the threshold value) and to com-
 3251 bine it with a random dE/dx value from a dE/dx template. The resulting track is
 3252 just as likely as the original, so a number of such random generations provide the
 3253 expected distributions of momentum and ionization. These are then combined
 3254 using the parametrization described in Section 11.4.1 to form a distribution of
 3255 mass for the signal region.

3256 Algorithmically this method is implemented by forming two distinct Control
 3257 Regions (**CR**s). The first **CR**, CR1, is formed by applying the entire event selec-
 3258 tion from Chapter 11 up to the dE/dx and mass requirements. The dE/dx re-
 3259 quirement is instead inverted for this region. Because of the independence of
 3260 dE/dx , the tracks in this control region have the same kinematic distribution
 3261 as the tracks in the signal region, and are used to measure a two-dimensional
 3262 template of p and η . The second **CR**, CR2, is formed from the event selection
 3263 through the dE/dx requirement, but with an inverted E_T^{miss} requirement. The
 3264 tracks in this control region are expected to have similar dE/dx distributions to
 3265 the signal region before the ionization requirement, and so this region is used to
 3266 measure a two-dimensional template of dE/dx and η .

3267 The contribution of any signal to the control regions is minimized by the in-
 3268 verted selection requirements. Only less than 10% of simulated signal events
 3269 have either dE/dx or E_T^{miss} below the threshold values in the original signal re-
 3270 gion, while the backgrounds are significantly enhanced by inverting those re-
 3271 quirements. The signal contamination is less than 1% in both control regions
 3272 for all of the simulated masses and lifetimes considered in this analysis.

3273 With those measured templates, the shape of the mass estimation is generated
 3274 by first selecting a random (p, η) combination from CR1. This momentum
 3275 value is combined with a dE/dx value taken from the appropriate distribution
 3276 of dE/dx for the selected η from CR2. The use of η in both random samplings
 3277 controls for any correlation between p , dE/dx , and η . Those values are then
 3278 used to calculate a mass in the same way that is done for regular tracks in data,
 3279 see Section 11.4.1. As this procedure includes all dE/dx values, the cut at 1.8
 3280 MeVg $^{-1}$ cm 2 is then enforced to fully model the signal region. The generated
 3281 mass distribution is then normalized by scaling the background estimate to the
 3282 data in the region $M < 160$ GeV, where signals of this type have already been
 3283 excluded [71]. This normalization uses the distributions of mass generated with-
 3284 out the ionization requirement.

3285 The statistical uncertainties on these background distributions are calculated
 3286 by independently fluctuating each bin of the input templates according to their
 3287 Poisson uncertainties. These fluctuations are repeated a large number of times,
 3288 and the uncertainty on the resulting distribution is taken as the root mean square
 3289 (RMS) deviation of the fluctuations from the average. As the procedure uses one
 3290 million random combinations to generate the distributions, The statistical un-
 3291 certainty from the actual random generations is negligible compared to the un-
 3292 certainty from measuring the templates.

3293 12.3 VALIDATION

3294 The validity of the background estimation technique can be evaluated in both
 3295 data and simulation. The underlying assumption that random combinations of
 3296 dE/dx and momentum can predict a mass distribution in an orthogonal region
 3297 can be tested using simulated samples where concerns like multiple particle types
 3298 can be controlled. Using the same technique in another set of signal-depleted
 3299 regions in data then extends this confidence to the more complicated case where
 3300 several particle species are inherently included.

3301 12.3.1 CLOSURE IN SIMULATION

3302 The first test of the procedure is done using a simulated sample of $W \rightarrow \mu\nu$
 3303 decays. These types of events provide the ingredients required to test the back-
 3304 ground estimate, E_T^{miss} and isolated tracks, with high statistics. In this example
 3305 there is no signal, so simulated events in the orthogonal CRs are used to estimate
 3306 the shape of the mass distribution of the simulated events in the signal region. To
 3307 reflect the different topology for W boson decays, the CRs use slightly modified
 3308 definitions. In all CRs, the requirement of $p > 150$ GeV and the SM rejection

3309 requirements are removed. Additionally, for the signal region the requirement
 3310 on E_T^{miss} is relaxed to 30 GeV and the corresponding inverted requirement on
 3311 CR2 is also set at 30 GeV.

3312 With these modified selections, the simulated and randomly generated distri-
 3313 butions of $M_{dE/dx}$ are shown in Figure 81. This figure includes the mass distri-
 3314 butions before and after the requirement on dE/dx , which significantly shapes
 3315 the distributions. In both cases the background estimation technique repro-
 3316 duces the shape of $M_{dE/dx}$ in the signal region. There is a small difference in the pos-
 3317 itive tail of the mass distribution prior to the ionization cut, where the random
 3318 events underestimate the fraction of tracks with mass above 150 GeV by about
 3319 20%. After the ionization requirement, however, this discrepancy is not present
 3320 and the two distributions agree to within statistical uncertainties.

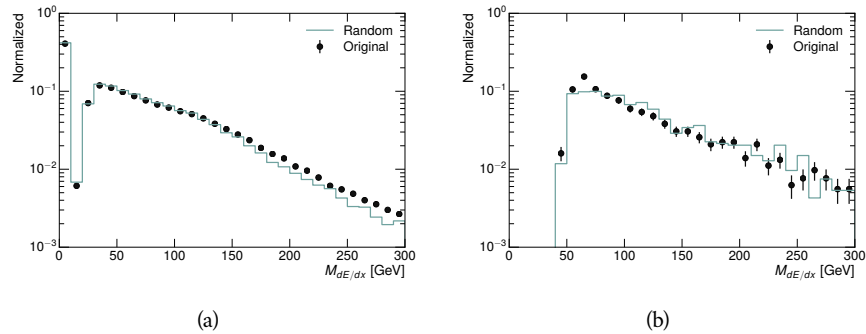


Figure 81: The distribution of $M_{dE/dx}$ (a) before and (b) after the ionization requirement for tracks in simulated W boson decays and for the randomly generated back-
 ground estimate.

3321 This ability to reproduce the shape of the mass distribution in simulated events
 3322 shows that the technique works as expected. No significant biases are acquired
 3323 in using low dE/dx events to select kinematic templates or in using low E_T^{miss}
 3324 events to select ionization templates, as either would result in a mismodeling of
 3325 the shape of the mass distribution. The simulated events contain only one par-
 3326 ticle type, however, so this test only establishes that the technique works well
 3327 when the the CRs are populated by exactly the same species.

3328 12.3.2 VALIDATION REGION IN DATA

3329 The second test of the background estimate is performed using data in an or-
 3330 thogonal validation region. The validation region, and the corresponding CRs,
 3331 are formed using the same selection requirements as in the nominal method but
 3332 with a modified requirement on momentum, $50 < p[\text{GeV}] < 150$. This allows
 3333 the technique to be checked in a region with very similar properties but where
 3334 the signal is depleted, as the majority of the signal has momentum above 150
 3335 GeV while the backgrounds are enhanced below that threshold. Any biases on
 3336 the particle composition of the CRs for the signal region will be reflected in the
 3337 CRs used to estimate the mass distribution in the validation region.

3338 Figure 82 shows the measured and randomly generated mass distributions for
 3339 data before and after the ionization requirement. The background estimate does
 3340 an excellent job of modeling the actual background before the ionization require-
 3341 ment, with good agreement to within the statistical uncertainties out to the limit
 3342 of the mass distribution. There are very few events in the validation region after
 3343 the ionization requirement, but the few observed events are consistent with the
 3344 background prediction. The good agreement in this validation region provides
 3345 a confirmation that the technique works even in the full-complexity case with
 3346 multiple particle types entering the distributions. Any bias from changes in par-
 3347 ticle composition between regions is small compared to statistical uncertainties.

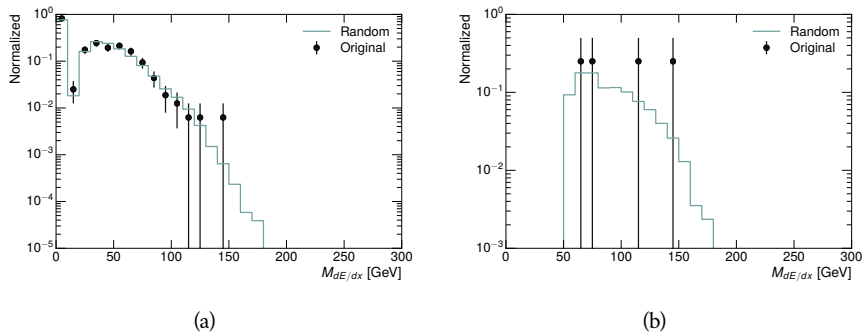


Figure 82: The distribution of $M_{dE/dx}$ (a) before and (b) after the ionization require-
 ment for tracks in the validation region and for the randomly generated back-
 ground estimate.

3348

3349 SYSTEMATIC UNCERTAINTIES AND RESULTS

3350 13.1 SYSTEMATIC UNCERTAINTIES

3351 A number of systematic uncertainties affect the interpretation of the results of
 3352 the search. These uncertainties can broken down into two major categories,
 3353 those which affect the estimate of the background using data and those which
 3354 affect the measurement of the signal yield estimated with simulated events. The
 3355 total measured systematic uncertainties are 7% for the background estimation
 3356 and approximately 32% for the signal yield depending on lifetime. These system-
 3357atic uncertainties are expected to be small compared to the statistical fluctuations
 3358 of the measured yields so that measured cross-sectional limits will be dominated
 3359 by statistical uncertainties. The following sections describe each source of sys-
 3360 tematic uncertainty for each of the two types.

3361 13.1.1 BACKGROUND ESTIMATE

3362 The systematic uncertainties on the background estimate come primarily from
 3363 considering alternative methods for generating the background distributions.
 3364 These uncertainties are small compared to the statistical uncertainties on the
 3365 background estimate which come from the limited statistics in measuring the
 3366 template distributions, as described in Section 12.2. They are summarized in
 3367 Table 10.

Source of Uncertainty:	Value [%]
Analytic Description of dE/dx	4.0
Muon Fraction (Stable Region only)	3.0
IBL Ionization Correction	3.8
Normalization	3.0
Total (Metastable Region):	6.3
Total (Stable Region):	7.0

Table 10: A summary of the sources of systematic uncertainty for the data-driven background in the signal region. If the uncertainty depends on the mass, the maximum values are reported.

3368 13.1.1.1 ANALYTIC DESCRIPTION OF DE/DX

3369 The background estimate uses a binned template distribution to estimate the
 3370 dE/dx of tracks in the signal region, as described in Section 12.2. It is also possi-

ble to fit that measured distribution to a functional form to help smooth the distribution in the tails of dE/dx where the template is driven by a small number of tracks. Both Landau convolved with a Gaussian and Crystal Ball functions are considered as the functional form and used to re-estimate the background distribution. The deviations compared to the nominal method are found to be 4%, and this is taken as a systematic uncertainty to cover the inability carefully predict the contribution from the long tail of dE/dx where there are few measurements available in data.

3379 13.11.2 MUON FRACTION

3380 The stable region of the analysis explicitly includes tracks identified as muons,
 3381 which have a known difference in their dE/dx distributions compared to non-
 3382 muon tracks (Section 12.1). To account for a difference in muon fraction be-
 3383 tween the background region and the signal region for this selection, the dE/dx
 3384 templates for muons and non-muons are measured separately and then the rel-
 3385 ative fraction of each is varied in the random generation. The muon fraction
 3386 is varied by its statistical uncertainty and the resulting difference of 3% in back-
 3387 ground yield is taken as the systematic uncertainty.

3388 13.11.3 IBL CORRECTIONS

3389 The IBL, described in Section 6.3.1, received a significant dose of radiation during
 3390 the data collection in 2015. The irradiation can cause a drift in the frontend
 3391 electronics and thus alter the dE/dx measurement which includes the ToT output
 3392 by the IBL. These effects are corrected for in the nominal analysis by scaling the
 3393 dE/dx measurements by a constant factor derived for each run to match the
 3394 average dE/dx value to a reference run where the IBL was known to be stable
 3395 to this effect. However, this corrective factor does not account for inter-run
 3396 variations. To account for this potential drift of dE/dx , the correction procedure
 3397 is repeated by varying the corrections up and down by the maximal run-to-run
 3398 variation from the full data-taking period, which results in an uncertainty of
 3399 3.8%.

3400 13.11.4 NORMALIZATION

3401 As described in Section 12.2, the generated distribution of masses is normalized
 3402 in a shoulder region ($M < 160$ GeV) where signals have been excluded by pre-
 3403 vious analyses. That normalization factor is varied by its statistical uncertainty
 3404 and the resulting fluctuation in the mass distribution of 3% is taken as a system-
 3405 atic uncertainty on the background estimate.

3406 13.12 SIGNAL YIELD

3407 The systematic uncertainties on the signal yield can be divided into three cate-
 3408 gories; those on the simulation process, those on the modeling of the detector
 3409 efficiency or calibration, and those affecting the overall signal yield. They are
 3410 summarized in Table 10. The largest uncertainty comes from the uncertainty

3411 on the production cross section for gluinos, which is the dominant systematic
 3412 uncertainty in this analysis.

Source of Uncertainty	-[%]	+[%]
ISR Modeling (Metastable Region)	1.5	1.5
ISR Modeling (Stable Region)	14	14
Pile-up Reweighting	1.1	1.1
Trigger Efficiency Reweighting	0.9	0.9
E_T^{miss} Scale	1.1	2.2
Ionization Parametrization	7.1	0
Momentum Parametrization	0.3	0.0
Electron Rejection	0.0	0.0
Hadron Rejection	0.0	0.0
μ Identification	4.3	4.3
Luminosity	5	5
Signal size uncertainty	28	28
Total (Metastable Region)	30	29
Total (Stable Region)	33	32

Table 11: A summary of the sources of systematic uncertainty for the simulated signal yield. The uncertainty depends on the mass and lifetime, and the maximum negative and positive values are reported in the table.

3413 13.1.2.1 ISR MODELING

3414 As discussed in Section 10.2, MadGraph is expected to reproduce the distribution
 3415 of ISR in signal events more accurately than the nominal Pythia samples. The
 3416 analysis reweights the distribution of ISR in the simulated signal events to match
 3417 the distribution found in generated MadGraph samples. This has an effect on the
 3418 selection efficiency in the signal samples, where ISR contributes to the generation
 3419 of E_T^{miss} . To account for the potential inaccuracy on the simulation of ISR at high
 3420 energies, half of the difference between the signal efficiency with the reweighted
 3421 distribution and the original distribution is taken as a systematic uncertainty.

3422 13.1.2.2 PILEUP REWEIGHTING

3423 The simulated events were generated prior to data collection with an estimate of
 3424 the average number of interactions per bunch crossing. This estimate does not
 3425 match the value of pileup during actual data collection, but a large fraction of the
 3426 simulated events would be discarded in order to match the distribution in data.
 3427 Therefore the simulated signal events are not reweighted for pileup by default
 3428 in the analysis. The effect of the pileup on signal efficiency is not expected to
 3429 depend on the mass or lifetime of the generated signal events, which allows all

3430 of the generated signal events to be used together to assess the pileup dependence.
 3431 To account for the potential effect of the difference in the number of interactions
 3432 per bunch crossing between data and simulation, the difference in yield between
 3433 the nominal signal events and the reweighted events averaged over all masses
 3434 and lifetimes is taken as a systematic uncertainty on the yield for each mass and
 3435 lifetime (1.1%).

3436 13.1.2.3 TRIGGER EFFICIENCY REWEIGHTING

3437 As described in Section 11.2, the selection for this analysis does not require a suf-
 3438 ficiently large value of E_T^{miss} to be above the plateau of trigger efficiency. There-
 3439 fore, some signal events which would otherwise pass the event selection can be
 3440 excluded because of the trigger requirement. These effects can be difficult to es-
 3441 timate in simulation, and thus are constrained by comparing data and simulated
 3442 events in an alternative W boson region which uses decays to muons to find a rel-
 3443 atively pure sample of events with missing energy. The trigger efficiency for data
 3444 and simulated W events are shown in Figure 83. The comparison between data
 3445 and MC in this region constrains the simulation of the trigger efficiency. The
 3446 simulated signal events are reweighted by the ratio of data to simulation in the
 3447 W boson decays, while the difference between the data and simulation in those
 3448 decays is taken as a systematic uncertainty. This results in an uncertainty of only
 3449 0.9% as the majority of events are well above the plateau and the disagreement
 3450 between data and simulation is small even below that plateau.

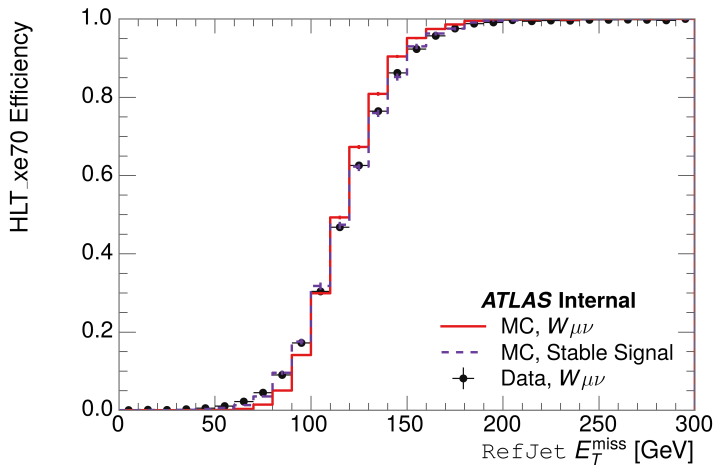


Figure 83: The trigger efficiency for the HLT_xe70 trigger requirement as a function of Calorimeter E_T^{miss} for simulated data events with a W boson selection. Simulated signal events and simulated W boson events are also included.

3451 13.1.2.4 MISSING TRANSVERSE MOMENTUM SCALE

3452 The ATLAS Combined Performance (CP) group provides a default recommenda-
 3453 tion for systematic variations of jets and missing energy (**note: I'm not quite**
 3454 **sure what to cite for this - I don't see any papers from the jet/met group**

Systematic Variation	-[%]	+[%]
JET_GroupedNP_1	-0.7	1.3
JET_GroupedNP_2	-0.7	1.2
JET_GroupedNP_3	-0.5	1.3

Table 12: Example of the contributing systematic variations to the total systematic for the E_T^{miss} Scale, as measured in a 1200 GeV, Stable R-Hadron signal sample.

3455 **after this was implemented).** These variations enter into this analysis only in
 3456 the requirement on E_T^{miss} . The effect of the measured scale of E_T^{miss} is evaluated
 3457 by varying the E_T^{miss} scale according to the one sigma variations provided by all
 3458 **CP** recommendations on objects affecting event kinematics in simulated signal
 3459 events. Missing energy is reconstructed from fully reconstructed objects so any
 3460 systematic uncertainties affecting jets, muons, electrons, or the E_T^{miss} soft terms
 3461 are included. The only non-negligible contributions found using this method are
 3462 itemized in Table 12 for an example signal sample (1200 GeV, Stable R-Hadron),
 3463 where the systematic is measured as the relative difference in the final signal ef-
 3464 ficiency after applying the associated variation through the CP tools. The only
 3465 variations that are significant are the grouped jet systematic variations, which
 3466 combine recommended jet systematic uncertainties into linearly independent
 3467 variations.

3468 As the peak of the reconstructed E_T^{miss} distribution in the signal is significantly
 3469 above the current threshold for events which pass the trigger requirement, the
 3470 effect of scale variation is expected to be small, which is consistent with the mea-
 3471 sured systematic of approximately 2%. Events which do not pass the trigger re-
 3472 quirement usually fail because there are no ISR jets in the event to balance the
 3473 R -hadrons' transverse momentum, so the reconstructed E_T^{miss} is low and there-
 3474 fore also expected to be not very sensitive to scale changes.

3475 13.1.2.5 MOMENTUM PARAMETRIZATION

3476 The uncertainty on the signal efficiency from track momentum is calculated us-
 3477 ing the **CP** group recommendations for tracks. In particular, only one recom-
 3478 mended systematic variation affects track momentum, the sagitta bias for q/P .
 3479 This uncertainty is propagated to the final selection efficiency by varying the
 3480 track momentum by the recommended one sigma variation, and the associated
 3481 uncertainty is found to be negligible (0.3%).

3482 13.1.2.6 IONIZATION REQUIREMENT

3483 The dE/dx distributions in data and simulated events have different most prob-
 3484 able values, which is due in part to radiation effects in the detector that are not
 3485 fully accounted for in the simulation. The difference does not affect the mass
 3486 measurement used in this analysis, as independent calibrations are done in sim-
 3487 ulation and in data. However, it does affect the efficiency of the high dE/dx
 3488 selection requirement. To calculate the size of the effect on the signal efficiency,

3489 the dE/dx distribution in signal simulation is scaled by a scale factor obtained
 3490 from comparing the dE/dx distribution of inclusive tracks in data and in sim-
 3491 ulation. The difference in efficiency for this sample with a scaled dE/dx dis-
 3492 tribution, relative to the nominal case, is taken as a systematic uncertainty on
 3493 signal efficiency. The uncertainty is as large as 7% for low masses and falls to a
 3494 negligible effect for large masses.

3495 13.1.2.7 ELECTRON AND JET REJECTION

3496 The systematic uncertainty on the electron rejection is measured by varying the
 3497 EM fraction requirement significantly, from 0.95 to 0.9. This is found to have
 3498 a less than 0.04% effect on signal acceptance, on average, and so is completely
 3499 negligible. Similarly, the uncertainty on jet rejection is measured by tightening
 3500 the E/p requirement from 0.5 to 0.4. This is found to have no effect on signal
 3501 acceptance, so again the systematic is again negligible.

3502 13.1.2.8 MUON VETO

3503 The metastable signal region requires that the candidate tracks are not identi-
 3504 fied as medium muons because the majority of R-Hadrons in the lifetime range
 3505 included in that region do not reach the muon spectrometers before they de-
 3506 cay. However, the exponential tail of the R-Hadron lifetime distribution results
 3507 in some R-Hadrons traversing the muon spectrometer. These can still fail the
 3508 muon medium identification because they can fail on the requirement on the
 3509 number of precision hits required to pass the loose selection because they ar-
 3510 rive late to the muon spectrometer. This can be seen in Figure 84, which shows
 3511 the efficiency of the muon veto as a function of $1/\beta$, for two simulated stable
 3512 R-Hadron samples.

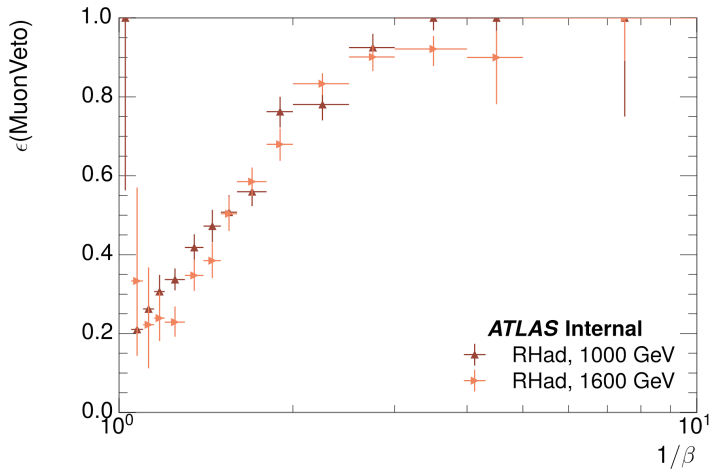


Figure 84: The efficiency of the muon veto for R -hadrons of two different masses, as a function of $1/\beta$ for simulated R-Hadron tracks.

3513 Thus, the efficiency of the muon veto depends on the timing resolution of
 3514 the spectrometer, so an uncertainty is applied to the signal efficiency to cover

3515 differences in timing resolution between data and simulation. First, a sample of
 3516 $Z \rightarrow \mu\mu$ events is selected in data in which one of the muons has a late arrival
 3517 time measured in the MDT. Then the reconstructed β distribution is compared
 3518 to the distribution in simulated $Z \rightarrow \mu\mu$ events; the difference between these
 3519 two distributions reflects the difference in timing resolution between data and
 3520 simulation. To emulate this difference in simulated signal events, the magnitude
 3521 of the difference is used to scale and shift the true β distribution of R-Hadrons in
 3522 simulation. Signal events are then reweighted based on this varied β distribution,
 3523 and the difference in the efficiency of the muon veto selection is compared with
 3524 the nominal and reweighted true β distributions. The difference in muon veto
 3525 efficiency is taken as a systematic uncertainty of the muon veto.

3526 The comparison of reconstructed β between data and simulation is performed
 3527 separately in the barrel, transition, and endcap regions of the spectrometer, and
 3528 the reweighting of the true β distribution in signal is done per region. The com-
 3529 parison of average reconstructed MDT β between data and simulation for the
 3530 barrel region is shown in Figure 85 for $Z \rightarrow \mu\mu$ events. As expected, The uncer-
 3531 tainty is found to be negligible for R-hadrons with short lifetimes, and is only
 3532 significant for lifetimes above 30 ns.

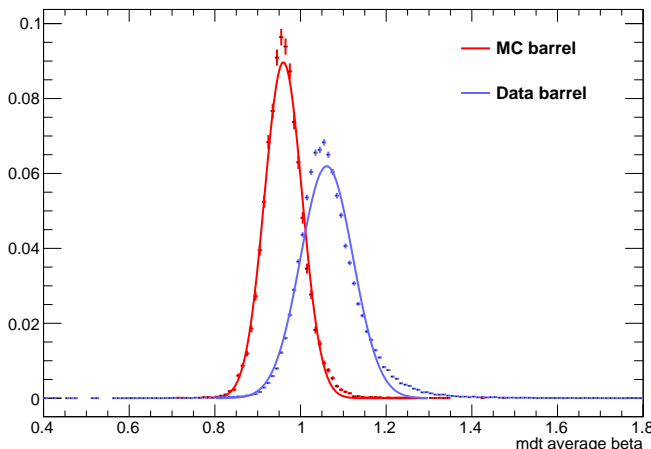


Figure 85: The average reconstructed MDT β distribution for $Z \rightarrow \mu\mu$ events in which
 one of the muons is reconstructed as a slow muon, for both data and simula-
 tion. A gaussian fit is superimposed.

3533 13.1.2.9 LUMINOSITY

3534 The luminosity uncertainty is provided by a luminosity measurement on ATLAS
 3535 and was measured to be 5% at the time of the publication of this analysis.

3536 13.1.2.10 SIGNAL SIZE

3537 As discussed in Section 10.2, the signal cross sections are calculated at NLO in the
 3538 strong coupling constant with a resummation of soft-gluon emission at NLL. The
 3539 uncertainties on those cross sections are between 14% to 28% for the R-Hadrons

Selection Region	Expected Background	Data
Stable	$17.2 \pm 2.6 \pm 1.2$	16
Metastable	$11.1 \pm 1.7 \pm 0.7$	11

Table 13: The estimated number of background events and the number of observed events in data for the specified selection regions prior to the requirement on mass. The background estimates show statistical and systematic uncertainties.

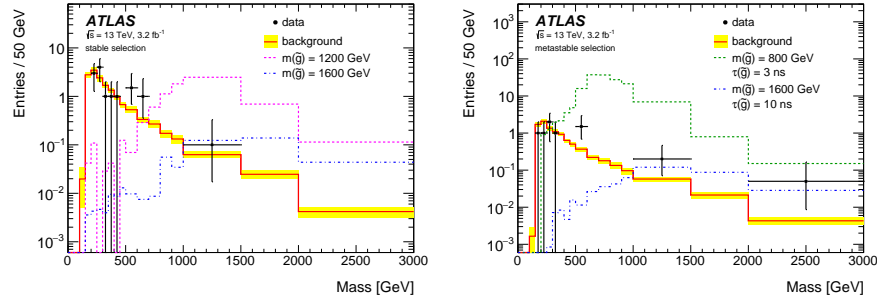


Figure 86: The observed mass distribution of events in data and the generated background distribution in (a) the stable and (b) the metastable signal region. A few example simulated signal distributions are superimposed.

3540 in the range of 400 to 1800 GeV [83, 84], where the uncertainty increases with
 3541 the mass.

3542 13.2 FINAL YIELDS

3543 This full analysis was performed using the 3.2 fb^{-1} from the 2015 data-taking.
 3544 Using the selections discussed in Chapter 11, sixteen events were observed in
 3545 the stable signal region and eleven events were observed in the metastable signal
 3546 region, prior to requirements on the candidate track mass. The background esti-
 3547 mate discussed in Chapter 12 predicts $17 \pm 2.6(\text{stat}) \pm 1.2(\text{syst})$ events for the
 3548 stable region and $11.1 \pm 1.7(\text{stat}) \pm 0.7(\text{syst})$ events for the metastable region.
 3549 These counts are summarized in Table 13.

3550 The mass estimated using dE/dx (Section 11.4.1) provides the final discrimi-
 3551 nating variable, where the signal would be expected as an excess in the falling ex-
 3552 ponential tail of the expected background. The observed distribution of masses
 3553 is shown in Figure 86, along with the predicted distribution from the background
 3554 estimate for each signal region. Both include a few example simulated signal dis-
 3555 tributions, which show the scale of an excess were the R-Hadron signals present.
 3556 Their is no statistically significant evidence of an excess in the data over the back-
 3557 ground estimation. From this distribution it is clearly possible to rule out signals
 3558 with lower masses, around 1200 GeV, which have larger cross sections.

3559 13.3 CROSS SECTIONAL LIMITS

3560 Because there is no observed significant excess of events in the signal region, this
 3561 analysis sets upper limits on the allowed cross section for R-Hadron production.
 3562 These limits are set for each mass point by counting the observed events in data,
 3563 along with the expected background and simulated signal events, in windows of
 3564 mass. The mass windows are formed by fitting the distribution of signal events to
 3565 a Gaussian distribution, and the window is then $\pm 1.4\sigma$ around the center of that
 3566 Gaussian. Two examples of the windows formed by this procedure are shown
 3567 in Tables 14-15, for the stable and 10 ns working points. The corresponding
 3568 counts of observed data, expected background, and simulated signal for those
 3569 same working points are shown in Tables 16-17. Appendix B includes the mass
 3570 windows and counts for all of the considered signal points.

$m(\tilde{g})$ [GeV]	Left Extremum [GeV]	Right Extremum [GeV]
1000	655	1349
1100	734	1455
1200	712	1631
1300	792	1737
1400	717	1926
1500	815	2117
1600	824	2122
1700	900	2274
1800	919	2344

Table 14: The left and right extremum of the mass window for each generated mass point with a 10 ns lifetime.

$m(\tilde{g})$ [GeV]	Left Extremum [GeV]	Right Extremum [GeV]
800	627	1053
1000	726	1277
1200	857	1584
1400	924	1937
1600	993	2308
1800	1004	2554

Table 15: The left and right extremum of the mass window used for each generated stable mass point.

3571 The 95% confidence level upper limits on the cross sections for a large grid of
 3572 masses (between 800 and 1800 GeV) and lifetimes (between 0.4 and stable) are
 3573 extracted from these counts with the CL_S method using the profile likelihood

$m(\tilde{g})$ [GeV]	Expected Signal	Expected Background	Observed Data
800	462.83 ± 14.86	1.764 ± 0.080	2.0
1000	108.73 ± 3.38	1.458 ± 0.070	1.0
1200	31.74 ± 0.95	1.137 ± 0.060	1.0
1400	10.22 ± 0.29	1.058 ± 0.058	1.0
1600	3.07 ± 0.09	0.947 ± 0.054	1.0
1800	1.08 ± 0.05	0.940 ± 0.054	1.0

Table 16: The expected number of signal events, the expected number of background events, and the observed number of events in data with their respective statistical errors within the respective mass window for each generated stable mass point

$m(\tilde{g})$ [GeV]	Expected Signal	Expected Background	Observed Data
1000	144.48 ± 5.14	1.499 ± 0.069	2.0
1100	73.19 ± 2.61	1.260 ± 0.060	2.0
1200	41.54 ± 1.41	1.456 ± 0.067	2.0
1300	22.58 ± 0.77	1.201 ± 0.058	2.0
1400	12.70 ± 0.42	1.558 ± 0.071	2.0
1500	6.73 ± 0.24	1.237 ± 0.060	2.0
1600	3.90 ± 0.13	1.201 ± 0.058	2.0
1700	2.27 ± 0.07	1.027 ± 0.052	2.0
1800	1.34 ± 0.04	1.019 ± 0.052	2.0

Table 17: The expected number of signal events, the expected number of background events, and the observed number of events in data with their respective statistical errors within the respective mass window for each generated mass point with a lifetime of 10 ns.

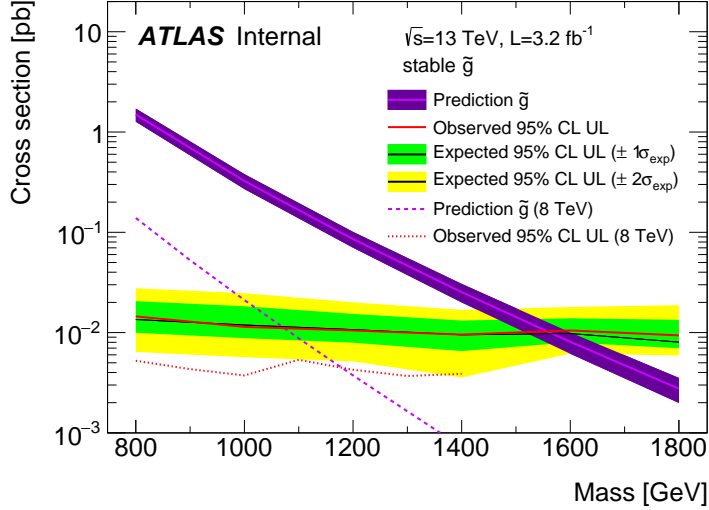


Figure 87: The observed and expected cross section limits as a function of mass for the stable simulated signal. The predicted cross section values for the corresponding signals are included.

ratio as a test statistic [88]. For this procedure, the systematic uncertainties estimated for the signal and background yields are treated as Gaussian-distributed nuisance parameters. The uncertainty on the normalization of the expected background distribution is included in the expected background events. At this point the expected cross section limit is calculated for both the metastable and stable signal region for each lifetime point, and the region with the best expected limit is selected for each lifetime. Using that procedure, the metastable region is used for lifetimes up to and including 30 ns, and the stable region for lifetimes above it.

The resulting cross-sectional upper limits are shown as a function of mass in Figure 87 and Figure 88 for each lifetime considered. The limits are interpolated linearly between each mass point, and the dependence of the limit on the mass is small as the efficiency is relatively constant for large R-Hadron masses. There is however a strong dependence on lifetime, as discussed in Section 11.5, where the probability to form a fully reconstructed track and the kinematic freedom to produce E_T^{miss} result in a local maximum in the limit at 10–30 ns. The figures also include the expected cross section for pair-produced gluino R-Hadrons for reference. For the 10 ns and stable cross section limits, both the observed limit and expected cross section for the Run 1, 8 TeV version of this analysis are included. There the cross sectional limits are lower because of the increased available luminosity, while the signal cross sections were also much lower because of the lower collision energy.

13.4 MASS LIMITS

The cross-sectional limits can then be used to derive a lower mass limit for gluino R-Hadrons by comparing them to the theoretically predicted production cross

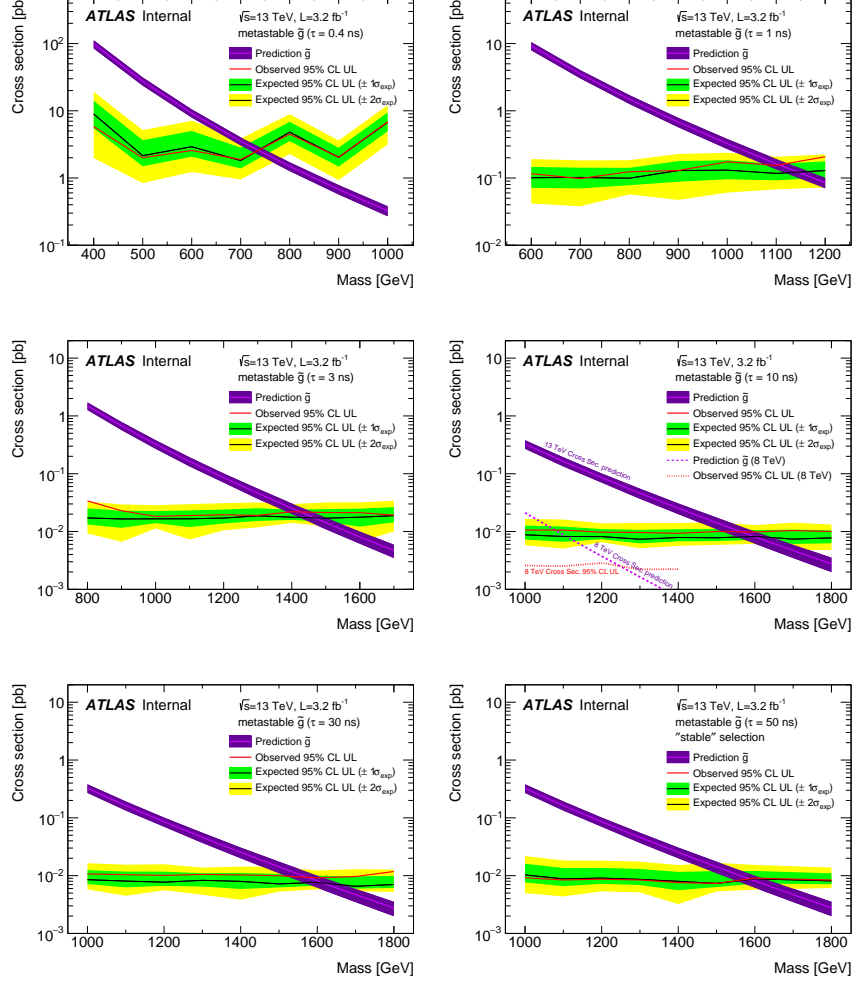


Figure 88: The observed and expected cross section limits as a function of mass for each generated lifetime. The predicted cross section values for the corresponding signals are included.

3599 sections. These mass limits range from only 740 GeV at the lowest lifetimes con-
 3600 sidered, where the selection efficiency is very low, to up to 1580 GeV at 30 ns
 3601 where the selection efficiency is maximized. The observed and expected mass
 3602 limits for each lifetime point are detailed in Table 18, which also lists which se-
 3603 lection region was used for each lifetime. These excluded range of masses as a
 3604 function of lifetime is also shown in Figure 89. The Run 1 limits are included for
 3605 comparison; the limits have increased by about 200 GeV on average. The search
 3606 has also improved since the previous incarnation from Run 1 in optimizing the
 3607 region between 30 GeV and detector-stable lifetimes by introducing the second
 3608 signal region. The definition of the stable region prevents the significant drop
 3609 in mass limit that occurred above 30 GeV in the Run 1 analysis.

Selection	τ [ns]	$M_{\text{obs}} > [\text{GeV}]$	$M_{\text{exp}} > [\text{GeV}]$
Metastable	0.4	740	730
"	1.0	1110	1150
"	3.0	1430	1470
"	10	1570	1600
"	30	1580	1620
Stable	50	1590	1590
"	stable	1570	1580

Table 18: The observed and expected 95% CL lower limit on mass for gluino R-Hadrons for each considered lifetime.

3610 13.5 CONTEXT FOR LONG-LIVED SEARCHES

3611 This search plays an important role in the current, combined [ATLAS](#) search for
 3612 long lived particles. The mass limits provided by various [ATLAS](#) searches for
 3613 long-lived gluino R-Hadrons can be seen in Figure 90. This search provides the
 3614 most competitive limit for lifetimes between 3 ns up through very long lifetimes,
 3615 where it is still competitive with dedicated searches for stable particles. The lim-
 3616 its placed on gluino production are very similar to the limits on promptly decay-
 3617 ing models.

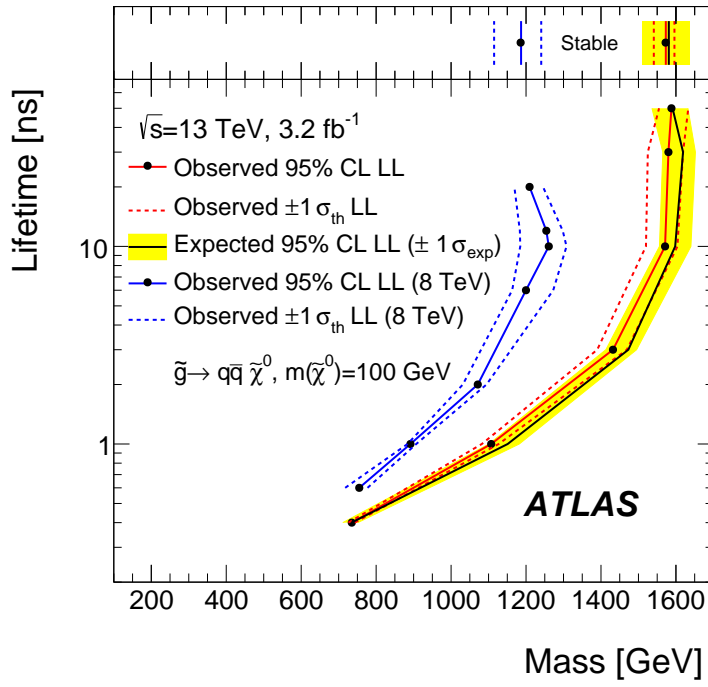


Figure 89: The excluded range of masses as a function of gluino lifetime. The expected lower limit (LL), with its experimental $\pm 1\sigma$ band, is given with respect to the nominal theoretical cross-section. The observed 95% LL obtained at $\sqrt{s} = 8 \text{ TeV}$ [71] is also shown for comparison.

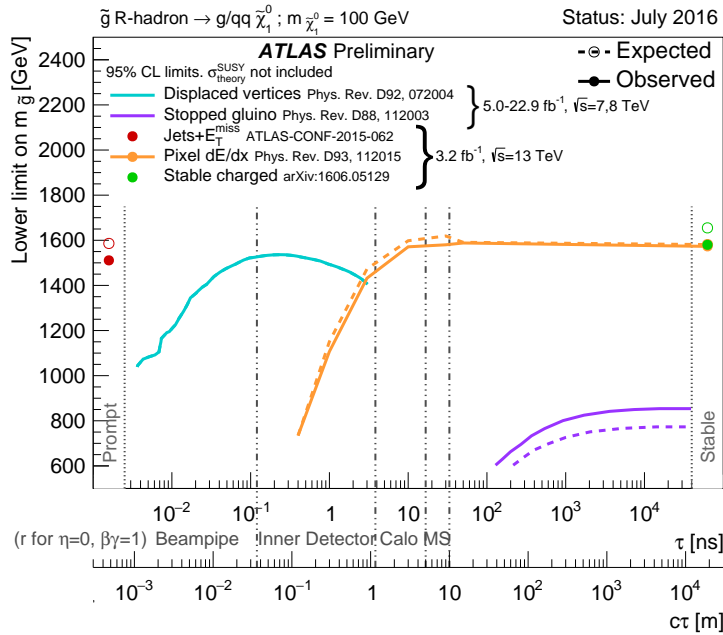


Figure 90: The constraints on the gluino mass as a function of lifetime for a split-supersymmetry model with the gluino R-Hadrons decaying into a gluon or light quarks and a neutralino with mass of 100 GeV. The solid lines indicate the observed limits, while the dashed lines indicate the expected limits. The area below the curves is excluded. The dots represent results for which the particle is assumed to be prompt or stable.

3618

PART VI

3619

CONCLUSIONS

3620

You can put some informational part preamble text here.

14

3621

3622 SUMMARY AND OUTLOOK

3623 14.1 SUMMARY

3624 14.2 OUTLOOK

3625

PART VII

3626

APPENDIX

3627

A

3628

3629 INELASTIC CROSS SECTION

B

3630

3631 EXPANDED R-HADRON YIELDS AND LIMITS

$m(\tilde{g})$ [GeV]	Left Extremum [GeV]	Right Extremum [GeV]
1000	682	1387
1100	763	1478
1200	801	1606
1300	809	1841
1400	861	2011
1500	920	2032
1600	952	2173
1800	1017	2422

Table 19: The left and right extremum of the mass window for each generated mass point with a 50 ns lifetime.

$m(\tilde{g})$ [GeV]	Left Extremum [GeV]	Right Extremum [GeV]
1000	689	1321
1100	746	1513
1200	788	1670
1300	860	1734
1400	833	1925
1500	852	2048
1600	833	2283
1700	946	2379
1800	869	2505

Table 20: The left and right extremum of the mass window for each generated mass point with a 30 ns lifetime.

$m(\tilde{g})$ [GeV]	Left Extremum [GeV]	Right Extremum [GeV]
1000	655	1349
1100	734	1455
1200	712	1631
1300	792	1737
1400	717	1926
1500	815	2117
1600	824	2122
1700	900	2274
1800	919	2344

Table 21: The left and right extremum of the mass window for each generated mass point with a 10 ns lifetime.

$m(\tilde{g})$ [GeV]	Left Extremum [GeV]	Right Extremum [GeV]
800	531	1065
900	576	1165
1000	610	1345
1100	635	1432
1200	663	1563
1300	620	1667
1400	742	1727
1500	761	1937
1600	573	2000
1700	621	2182

Table 22: The left and right extremum of the mass window used for each generated mass point with a lifetime of 3 ns.

$m(\tilde{g})$ [GeV]	Left Extremum [GeV]	Right Extremum [GeV]
600	411	758
700	385	876
800	486	970
900	406	987
1000	408	1136
1100	555	1196
1200	516	1378

Table 23: The left and right extremum of the mass window used for each mass point with a lifetime of 1 ns.

$m(\tilde{g})$ [GeV]	Left Extremum [GeV]	Right Extremum [GeV]
400	204	510
500	295	639
600	288	702
700	323	701
800	190	771
900	277	677
1000	249	688

Table 24: The left and right extremum of the mass window for each generated mass point with a lifetime of 0.4 ns.

$m(\tilde{g})$ [GeV]	Left Extremum [GeV]	Right Extremum [GeV]
800	627	1053
1000	726	1277
1200	857	1584
1400	924	1937
1600	993	2308
1800	1004	2554

Table 25: The left and right extremum of the mass window used for each generated stable mass point.

$m(\tilde{g})$ [GeV]	Expected Signal	Expected Background	Observed Data
1000	131.18 ± 6.35	1.803 ± 0.081	1.0 ± 1.0
1100	71.11 ± 3.35	1.409 ± 0.069	1.0 ± 1.0
1200	37.18 ± 1.75	1.310 ± 0.066	1.0 ± 1.0
1300	20.76 ± 0.95	1.431 ± 0.069	1.0 ± 1.0
1400	12.63 ± 0.57	1.273 ± 0.065	1.0 ± 1.0
1500	6.57 ± 0.29	1.115 ± 0.059	1.0 ± 1.0
1600	3.56 ± 0.16	1.041 ± 0.057	1.0 ± 1.0
1800	1.27 ± 0.05	0.918 ± 0.053	1.0 ± 1.0

Table 26: The expected number of signal events, the expected number of background events, and the observed number of events in data with their respective statistical errors within the respective mass window for each generated mass point with a lifetime of 50 ns.

$m(\tilde{g})$ [GeV]	Expected Signal	Expected Background	Observed Data
1000	144.65 ± 6.34	1.328 ± 0.063	2.0 ± 1.4
1100	75.28 ± 3.27	1.255 ± 0.060	2.0 ± 1.4
1200	40.51 ± 1.75	1.193 ± 0.058	2.0 ± 1.4
1300	20.91 ± 0.93	0.997 ± 0.051	2.0 ± 1.4
1400	11.97 ± 0.51	1.131 ± 0.056	2.0 ± 1.4
1500	6.81 ± 0.28	1.111 ± 0.055	2.0 ± 1.4
1600	4.19 ± 0.16	1.193 ± 0.058	2.0 ± 1.4
1700	2.42 ± 0.09	0.963 ± 0.050	2.0 ± 1.4
1800	1.46 ± 0.05	1.138 ± 0.056	3.0 ± 1.7

Table 27: The expected number of signal events, the expected number of background events, and the observed number of events in data with their respective statistical errors within the respective mass window for each generated mass point with a lifetime of 30 ns.

$m(\tilde{g})$ [GeV]	Expected Signal	Expected Background	Observed Data
1000	144.48 ± 5.14	1.499 ± 0.069	2.0 ± 1.4
1100	73.19 ± 2.61	1.260 ± 0.060	2.0 ± 1.4
1200	41.54 ± 1.41	1.456 ± 0.067	2.0 ± 1.4
1300	22.58 ± 0.77	1.201 ± 0.058	2.0 ± 1.4
1400	12.70 ± 0.42	1.558 ± 0.071	2.0 ± 1.4
1500	6.73 ± 0.24	1.237 ± 0.060	2.0 ± 1.4
1600	3.90 ± 0.13	1.201 ± 0.058	2.0 ± 1.4
1700	2.27 ± 0.07	1.027 ± 0.052	2.0 ± 1.4
1800	1.34 ± 0.04	1.019 ± 0.052	2.0 ± 1.4

Table 28: The expected number of signal events, the expected number of background events, and the observed number of events in data with their respective statistical errors within the respective mass window for each generated mass point with a lifetime of 10 ns.

$m(\tilde{g})$ [GeV]	Expected Signal	Expected Background	Observed Data
800	362.97 ± 14.68	1.841 ± 0.080	5.0 ± 2.2
900	169.20 ± 6.69	1.710 ± 0.076	3.0 ± 1.7
1000	84.78 ± 3.23	1.727 ± 0.076	2.0 ± 1.4
1100	40.06 ± 1.60	1.679 ± 0.075	2.0 ± 1.4
1200	20.06 ± 0.81	1.598 ± 0.072	2.0 ± 1.4
1300	10.76 ± 0.43	1.851 ± 0.080	2.0 ± 1.4
1400	5.52 ± 0.22	1.374 ± 0.064	2.0 ± 1.4
1500	3.16 ± 0.13	1.355 ± 0.064	2.0 ± 1.4
1600	2.13 ± 0.11	2.235 ± 0.093	3.0 ± 1.7
1700	1.10 ± 0.06	1.995 ± 0.085	2.0 ± 1.4

Table 29: The expected number of signal events, the expected number of background events, and the observed number of events in data with their respective statistical errors within the respective mass window for each generated mass point with a lifetime of 3 ns.

$m(\tilde{g})$ [GeV]	Expected Signal	Expected Background	Observed Data
600	431.80 ± 36.60	2.418 ± 0.099	3.0 ± 1.7
700	192.77 ± 15.28	3.267 ± 0.126	3.0 ± 1.7
800	69.63 ± 5.90	2.125 ± 0.089	3.0 ± 1.7
900	28.91 ± 2.59	3.114 ± 0.121	3.0 ± 1.7
1000	13.64 ± 1.22	3.359 ± 0.129	5.0 ± 2.2
1100	6.13 ± 0.57	1.879 ± 0.081	3.0 ± 1.7
1200	3.24 ± 0.30	2.387 ± 0.098	5.0 ± 2.2

Table 30: The expected number of signal events, the expected number of background events, and the observed number of events in data with their respective statistical errors within the respective mass window for each generated mass point with a lifetime of 1 ns.

$m(\tilde{g})$ [GeV]	Expected Signal	Expected Background	Observed Data
400	181.71 ± 75.59	6.780 ± 0.238	4.0 ± 2.0
500	103.88 ± 30.05	4.310 ± 0.160	4.0 ± 2.0
600	28.34 ± 9.34	4.868 ± 0.177	4.0 ± 2.0
700	13.62 ± 4.00	3.908 ± 0.147	4.0 ± 2.0
800	2.75 ± 1.15	9.001 ± 0.308	8.0 ± 2.8
900	2.25 ± 0.71	5.045 ± 0.183	5.0 ± 2.2
1000	0.34 ± 0.19	6.026 ± 0.214	6.0 ± 2.4

Table 31: The expected number of signal events, the expected number of background events, and the observed number of events in data with their respective statistical errors within the respective mass window for each generated mass point with a lifetime of p4 ns.

$m(\tilde{g})$ [GeV]	Expected Signal	Expected Background	Observed Data
800	462.83 ± 14.86	1.764 ± 0.080	2.0 ± 1.4
1000	108.73 ± 3.38	1.458 ± 0.070	1.0 ± 1.0
1200	31.74 ± 0.95	1.137 ± 0.060	1.0 ± 1.0
1400	10.22 ± 0.29	1.058 ± 0.058	1.0 ± 1.0
1600	3.07 ± 0.09	0.947 ± 0.054	1.0 ± 1.0
1800	1.08 ± 0.05	0.940 ± 0.054	1.0 ± 1.0

Table 32: The expected number of signal events, the expected number of background events, and the observed number of events in data with their respective statistical errors within the respective mass window for each generated stable mass point

- 3633 [1] A. D. Martin, W. J. Stirling, R. S. Thorne, and G. Watt. “Parton distributions
3634 for the LHC”. In: *Eur. Phys. J.* C63 (2009), pp. 189–285. doi: [10.1140/epjc/s10052-009-1072-5](https://doi.org/10.1140/epjc/s10052-009-1072-5). arXiv: [0901.0002 \[hep-ph\]](https://arxiv.org/abs/0901.0002).
- 3636 [2] Prajwal Raj Kafle, Sanjib Sharma, Geraint F. Lewis, and Joss Bland-Hawthorn.
3637 “On the Shoulders of Giants: Properties of the Stellar Halo and the Milky
3638 Way Mass Distribution”. In: *Astrophys. J.* 794.1 (2014), p. 59. doi: [10.1088/0004-637X/794/1/59](https://doi.org/10.1088/0004-637X/794/1/59). arXiv: [1408.1787 \[astro-ph.GA\]](https://arxiv.org/abs/1408.1787).
- 3640 [3] Lyndon Evans and Philip Bryant. “LHC Machine”. In: *JINST* 3 (2008), S08001.
3641 doi: [10.1088/1748-0221/3/08/S08001](https://doi.org/10.1088/1748-0221/3/08/S08001).
- 3642 [4] C Lefevre. “LHC: the guide (English version). Guide du LHC (version anglaise)”.
3643 2009. URL: <https://cds.cern.ch/record/1165534>.
- 3644 [5] “LEP Design Report Vol.1”. In: (1983).
- 3645 [6] ATLAS Collaboration. “The ATLAS Experiment at the CERN Large Hadron
3646 Collider”. In: *JINST* 3 (2008), S08003. doi: [10.1088/1748-0221/3/08/S08003](https://doi.org/10.1088/1748-0221/3/08/S08003).
- 3648 [7] S. Chatrchyan et al. “The CMS experiment at the CERN LHC”. In: *JINST*
3649 3 (2008), S08004. doi: [10.1088/1748-0221/3/08/S08004](https://doi.org/10.1088/1748-0221/3/08/S08004).
- 3650 [8] A. Augusto Alves Jr. et al. “The LHCb Detector at the LHC”. In: *JINST* 3
3651 (2008), S08005. doi: [10.1088/1748-0221/3/08/S08005](https://doi.org/10.1088/1748-0221/3/08/S08005).
- 3652 [9] K. Aamodt et al. “The ALICE experiment at the CERN LHC”. In: *JINST* 3
3653 (2008), S08002. doi: [10.1088/1748-0221/3/08/S08002](https://doi.org/10.1088/1748-0221/3/08/S08002).
- 3654 [10] K. A. Olive et al. “Review of Particle Physics”. In: *Chin. Phys. C38* (2014),
3655 p. 090001. doi: [10.1088/1674-1137/38/9/090001](https://doi.org/10.1088/1674-1137/38/9/090001).
- 3656 [11] Daniel Froidevaux and Paris Sphicas. “General-Purpose Detectors for the
3657 Large Hadron Collider”. In: *Annual Review of Nuclear and Particle Science*
3658 56.1 (2006), pp. 375–440. doi: [10.1146/annurev.nucl.54.070103.181209](https://doi.org/10.1146/annurev.nucl.54.070103.181209). URL: <http://dx.doi.org/10.1146/annurev.nucl.54.070103.181209>.
- 3661 [12] M Capeans, G Darbo, K Einsweiller, M Elsing, T Flick, M Garcia-Sciveres,
3662 C Gemme, H Pernegger, O Rohne, and R Vuillermet. *ATLAS Insertable B-*
3663 *Layer Technical Design Report*. Tech. rep. CERN-LHCC-2010-013. ATLAS-
3664 TDR-19. 2010. URL: <https://cds.cern.ch/record/1291633>.
- 3665 [13] T. Cornelissen, M. Elsing, S. Fleischmann, W. Liebig, and E. Moyse. “Con-
3666 cepts, Design and Implementation of the ATLAS New Tracking (NEWT)”.
3667 In: (2007). Ed. by A. Salzburger.
- 3668 [14] “Performance of the ATLAS Inner Detector Track and Vertex Reconstruc-
3669 tion in the High Pile-Up LHC Environment”. In: (2012).

- 3670 [15] ATLAS Collaboration. “A neural network clustering algorithm for the AT-
 3671 LAS silicon pixel detector”. In: *JINST* 9 (2014), P09009. doi: [10.1088/1748-0221/9/09/P09009](https://doi.org/10.1088/1748-0221/9/09/P09009). arXiv: [1406.7690 \[hep-ex\]](https://arxiv.org/abs/1406.7690).
- 3673 [16] ATLAS Collaboration. “Electron reconstruction and identification efficiency
 3674 measurements with the ATLAS detector using the 2011 LHC proton–proton
 3675 collision data”. In: *Eur. Phys. J. C* 74 (2014), p. 2941. doi: [10.1140/epjc/s10052-014-2941-0](https://doi.org/10.1140/epjc/s10052-014-2941-0). arXiv: [1404.2240 \[hep-ex\]](https://arxiv.org/abs/1404.2240). PERF-2013-03.
- 3677 [17] Matteo Cacciari, Gavin P. Salam, and Gregory Soyez. “The anti- k_t jet clus-
 3678 tering algorithm”. In: *JHEP* 04 (2008), p. 063. doi: [10.1088/1126-6708/2008/04/063](https://doi.org/10.1088/1126-6708/2008/04/063). arXiv: [0802.1189 \[hep-ph\]](https://arxiv.org/abs/0802.1189).
- 3680 [18] S. Agostinelli et al. “GEANT4: A simulation toolkit”. In: *Nucl. Instrum. Meth.*
 3681 A 506 (2003), pp. 250–303. doi: [10.1016/S0168-9002\(03\)01368-8](https://doi.org/10.1016/S0168-9002(03)01368-8).
- 3682 [19] ATLAS Collaboration. “A study of the material in the ATLAS inner de-
 3683 tector using secondary hadronic interactions”. In: *JINST* 7 (2012), P01013.
 3684 doi: [10.1088/1748-0221/7/01/P01013](https://doi.org/10.1088/1748-0221/7/01/P01013). arXiv: [1110.6191 \[hep-ex\]](https://arxiv.org/abs/1110.6191).
 3685 PERF-2011-08.
- 3686 [20] ATLAS Collaboration. “Electron and photon energy calibration with the
 3687 ATLAS detector using LHC Run 1 data”. In: *Eur. Phys. J. C* 74 (2014), p. 3071.
 3688 doi: [10.1140/epjc/s10052-014-3071-4](https://doi.org/10.1140/epjc/s10052-014-3071-4). arXiv: [1407.5063 \[hep-ex\]](https://arxiv.org/abs/1407.5063). PERF-2013-05.
- 3690 [21] ATLAS Collaboration. “A measurement of the calorimeter response to sin-
 3691 gle hadrons and determination of the jet energy scale uncertainty using
 3692 LHC Run-1 pp -collision data with the ATLAS detector”. In: (2016). arXiv:
 3693 [1607.08842 \[hep-ex\]](https://arxiv.org/abs/1607.08842). PERF-2015-05.
- 3694 [22] ATLAS Collaboration. “Single hadron response measurement and calorime-
 3695 ter jet energy scale uncertainty with the ATLAS detector at the LHC”. In:
 3696 *Eur. Phys. J. C* 73 (2013), p. 2305. doi: [10.1140/epjc/s10052-013-2305-1](https://doi.org/10.1140/epjc/s10052-013-2305-1). arXiv: [1203.1302 \[hep-ex\]](https://arxiv.org/abs/1203.1302). PERF-2011-05.
- 3698 [23] ATLAS Collaboration. “The ATLAS Simulation Infrastructure”. In: *Eur.*
 3699 *Phys. J. C* 70 (2010), p. 823. doi: [10.1140/epjc/s10052-010-1429-9](https://doi.org/10.1140/epjc/s10052-010-1429-9).
 3700 arXiv: [1005.4568 \[hep-ex\]](https://arxiv.org/abs/1005.4568). SOFT-2010-01.
- 3701 [24] T. Sjöstrand, S. Mrenna, and P. Skands. “A Brief Introduction to PYTHIA
 3702 8.1”. In: *Comput. Phys. Commun.* 178 (2008), pp. 852–867. doi: [10.1016/j.cpc.2008.01.036](https://doi.org/10.1016/j.cpc.2008.01.036). arXiv: [0710.3820](https://arxiv.org/abs/0710.3820).
- 3704 [25] ATLAS Collaboration. *Summary of ATLAS Pythia 8 tunes*. ATL-PHYS-PUB-
 3705 2012-003. 2012. URL: <http://cds.cern.ch/record/1474107>.
- 3706 [26] A.D. Martin, W.J. Stirling, R.S. Thorne, and G. Watt. “Parton distributions
 3707 for the LHC”. In: *Eur. Phys. J. C* 63 (2009). Figures from the [MSTW Website](#),
 3708 pp. 189–285. doi: [10.1140/epjc/s10052-009-1072-5](https://doi.org/10.1140/epjc/s10052-009-1072-5). arXiv: [0901.0002](https://arxiv.org/abs/0901.0002).
- 3710 [27] A. Sherstnev and R.S. Thorne. “Parton Distributions for LO Generators”.
 3711 In: *Eur. Phys. J. C* 55 (2008), pp. 553–575. doi: [10.1140/epjc/s10052-008-0610-x](https://doi.org/10.1140/epjc/s10052-008-0610-x). arXiv: [0711.2473](https://arxiv.org/abs/0711.2473).

- 3713 [28] A. Ribon et al. *Status of Geant4 hadronic physics for the simulation of LHC*
 3714 *experiments at the start of LHC physics program.* CERN-LCGAPP-2010-02.
 3715 2010. URL: <http://lcgapp.cern.ch/project/docs/noteStatusHadronic2010.pdf>.
- 3716
- 3717 [29] M. P. Guthrie, R. G. Alsmiller, and H. W. Bertini. "Calculation of the cap-
 3718 ture of negative pions in light elements and comparison with experiments
 3719 pertaining to cancer radiotherapy". In: *Nucl. Instrum. Meth.* 66 (1968), pp. 29–
 3720 36. doi: [10.1016/0029-554X\(68\)90054-2](https://doi.org/10.1016/0029-554X(68)90054-2).
- 3721 [30] H. W. Bertini and P. Guthrie. "News item results from medium-energy
 3722 intranuclear-cascade calculation". In: *Nucl. Instr. and Meth. A* 169 (1971),
 3723 p. 670. doi: [10.1016/0375-9474\(71\)90710-X](https://doi.org/10.1016/0375-9474(71)90710-X).
- 3724 [31] V.A. Karmanov. "Light Front Wave Function of Relativistic Composite
 3725 System in Explicitly Solvable Model". In: *Nucl. Phys. B* 166 (1980), p. 378.
 3726 doi: [10.1016/0550-3213\(80\)90204-7](https://doi.org/10.1016/0550-3213(80)90204-7).
- 3727 [32] H. S. Fesefeldt. *GHEISHA program.* Pitha-85-02, Aachen. 1985.
- 3728 [33] G. Folger and J.P. Wellisch. "String parton models in Geant4". In: (2003).
 3729 arXiv: [nucl-th/0306007](https://arxiv.org/abs/hep-ph/0306007).
- 3730 [34] N. S. Amelin et al. "Transverse flow and collectivity in ultrarelativistic
 3731 heavy-ion collisions". In: *Phys. Rev. Lett.* 67 (1991), p. 1523. doi: [10.1103/PhysRevLett.67.1523](https://doi.org/10.1103/PhysRevLett.67.1523).
- 3732
- 3733 [35] N. S. Amelin et al. "Collectivity in ultrarelativistic heavy ion collisions". In:
 3734 *Nucl. Phys. A* 544 (1992), p. 463. doi: [10.1016/0375-9474\(92\)90598-E](https://doi.org/10.1016/0375-9474(92)90598-E).
- 3735
- 3736 [36] L. V. Bravina et al. "Fluid dynamics and Quark Gluon string model - What
 3737 we can expect for Au+Au collisions at 11.6 AGeV/c". In: *Nucl. Phys. A* 566
 3738 (1994), p. 461. doi: [10.1016/0375-9474\(94\)90669-6](https://doi.org/10.1016/0375-9474(94)90669-6).
- 3739 [37] L. V. Bravin et al. "Scaling violation of transverse flow in heavy ion colli-
 3740 sions at AGS energies". In: *Phys. Lett. B* 344 (1995), p. 49. doi: [10.1016/0370-2693\(94\)01560-Y](https://doi.org/10.1016/0370-2693(94)01560-Y).
- 3741
- 3742 [38] B. Andersson et al. "A model for low-pT hadronic reactions with general-
 3743 izations to hadron-nucleus and nucleus-nucleus collisions". In: *Nucl. Phys.*
 3744 *B* 281 (1987), p. 289. doi: [10.1016/0550-3213\(87\)90257-4](https://doi.org/10.1016/0550-3213(87)90257-4).
- 3745 [39] B. Andersson, A. Tai, and B.-H. Sa. "Final state interactions in the (nuclear)
 3746 FRITIOF string interaction scenario". In: *Z. Phys. C* 70 (1996), pp. 499–
 3747 506. doi: [10.1007/s002880050127](https://doi.org/10.1007/s002880050127).
- 3748 [40] B. Nilsson-Almqvist and E. Stenlund. "Interactions Between Hadrons and
 3749 Nuclei: The Lund Monte Carlo, Fritiof Version 1.6". In: *Comput. Phys. Com-*
 3750 *mun.* 43 (1987), p. 387. doi: [10.1016/0010-4655\(87\)90056-7](https://doi.org/10.1016/0010-4655(87)90056-7).
- 3751 [41] B. Ganhuyag and V. Uzhinsky. "Modified FRITIOF code: Negative charged
 3752 particle production in high energy nucleus nucleus interactions". In: *Czech.*
 3753 *J. Phys.* 47 (1997), pp. 913–918. doi: [10.1023/A:1021296114786](https://doi.org/10.1023/A:1021296114786).

- 3754 [42] ATLAS Collaboration. “Topological cell clustering in the ATLAS calorimeters and its performance in LHC Run 1”. In: (2016). arXiv: [1603.02934](https://arxiv.org/abs/1603.02934) [hep-ex].
- 3755
3756
3757 [43] Peter Speckmayer. “Energy Measurement of Hadrons with the CERN ATLAS Calorimeter”. Presented on 18 Jun 2008. PhD thesis. Vienna: Vienna, Tech. U., 2008. URL: <http://cds.cern.ch/record/1112036>.
- 3760 [44] CMS Collaboration. “The CMS barrel calorimeter response to particle beams from 2 to 350 GeV/c”. In: *Eur. Phys. J. C* 60.3 (2009). doi: [10.1140/epjc/s10052-009-0959-5](https://doi.org/10.1140/epjc/s10052-009-0959-5).
- 3763 [45] J. Beringer et al. (Particle Data Group). “Review of Particle Physics”. In: *Chin. Phys. C* 38 (2014), p. 090001. URL: <http://pdg.lbl.gov>.
- 3765 [46] P. Adragna et al. “Measurement of Pion and Proton Response and Longitudinal Shower Profiles up to 20 Nuclear Interaction Lengths with the ATLAS Tile Calorimeter”. In: *Nucl. Instrum. Meth. A* 615 (2010), pp. 158–181. doi: [10.1016/j.nima.2010.01.037](https://doi.org/10.1016/j.nima.2010.01.037).
- 3769 [47] ATLAS Collaboration. “Jet energy measurement and its systematic uncertainty in proton–proton collisions at $\sqrt{s} = 7$ TeV with the ATLAS detector”. In: *Eur. Phys. J. C* 75 (2015), p. 17. doi: [10.1140/epjc/s10052-014-3190-y](https://doi.org/10.1140/epjc/s10052-014-3190-y). arXiv: [1406.0076](https://arxiv.org/abs/1406.0076) [hep-ex]. PERF-2012-01.
- 3773 [48] Hung-Liang Lai, Marco Guzzi, Joey Huston, Zhao Li, Pavel M. Nadolsky, et al. “New parton distributions for collider physics”. In: *Phys. Rev. D* 82 (2010), p. 074024. doi: [10.1103/PhysRevD.82.074024](https://doi.org/10.1103/PhysRevD.82.074024). arXiv: [1007.2241](https://arxiv.org/abs/1007.2241) [hep-ph].
- 3777 [49] E. Abat et al. “Study of energy response and resolution of the ATLAS barrel calorimeter to hadrons of energies from 20 to 350 GeV”. In: *Nucl. Instrum. Meth. A* 621.1-3 (2010), pp. 134 – 150. doi: <http://dx.doi.org/10.1016/j.nima.2010.04.054>.
- 3781 [50] ATLAS Collaboration. “Jet energy measurement with the ATLAS detector in proton–proton collisions at $\sqrt{s} = 7$ TeV”. In: *Eur. Phys. J. C* 73 (2013), p. 2304. doi: [10.1140/epjc/s10052-013-2304-2](https://doi.org/10.1140/epjc/s10052-013-2304-2). arXiv: [1112.6426](https://arxiv.org/abs/1112.6426) [hep-ex]. PERF-2011-03.
- 3785 [51] Nausheen R. Shah and Carlos E. M. Wagner. “Gravitons and dark matter in universal extra dimensions”. In: *Phys. Rev. D* 74 (2006), p. 104008. doi: [10.1103/PhysRevD.74.104008](https://doi.org/10.1103/PhysRevD.74.104008). arXiv: [hep-ph/0608140](https://arxiv.org/abs/hep-ph/0608140) [hep-ph].
- 3788 [52] Jonathan L. Feng, Arvind Rajaraman, and Fumihiro Takayama. “Graviton cosmology in universal extra dimensions”. In: *Phys. Rev. D* 68 (2003), p. 085018. doi: [10.1103/PhysRevD.68.085018](https://doi.org/10.1103/PhysRevD.68.085018). arXiv: [hep-ph/0307375](https://arxiv.org/abs/hep-ph/0307375) [hep-ph].
- 3792 [53] Paul H. Frampton and Pham Quang Hung. “Long-lived quarks?” In: *Phys. Rev. D* 58 (5 1998), p. 057704. doi: [10.1103/PhysRevD.58.057704](https://doi.org/10.1103/PhysRevD.58.057704). URL: <http://link.aps.org/doi/10.1103/PhysRevD.58.057704>.

- 3796 [54] C. Friberg, E. Norrbin, and T. Sjostrand. “QCD aspects of leptoquark pro-
 3797 duction at HERA”. In: *Phys. Lett.* B403 (1997), pp. 329–334. doi: [10.1016/S0370-2693\(97\)00543-1](https://doi.org/10.1016/S0370-2693(97)00543-1). arXiv: [hep-ph/9704214](https://arxiv.org/abs/hep-ph/9704214) [hep-ph].
- 3799 [55] Herbert K. Dreiner. “An introduction to explicit R-parity violation”. In:
 3800 (1997). arXiv: [hep-ph/9707435](https://arxiv.org/abs/hep-ph/9707435).
- 3801 [56] Edmond L. Berger and Zack Sullivan. “Lower limits on R-parity-violating
 3802 couplings in supersymmetry”. In: *Phys. Rev. Lett.* 92 (2004), p. 201801. doi:
 3803 [10.1103/PhysRevLett.92.201801](https://doi.org/10.1103/PhysRevLett.92.201801). arXiv: [hep-ph/0310001](https://arxiv.org/abs/hep-ph/0310001).
- 3804 [57] R. Barbieri, C. Berat, M. Besancon, M. Chemtob, A. Deandrea, et al. “R-
 3805 parity violating supersymmetry”. In: *Phys. Rept.* 420 (2005), p. 1. doi: [10.1016/j.physrep.2005.08.006](https://doi.org/10.1016/j.physrep.2005.08.006). arXiv: [hep-ph/0406039](https://arxiv.org/abs/hep-ph/0406039).
- 3807 [58] M. Fairbairn et al. “Stable massive particles at colliders”. In: *Phys. Rept.* 438
 3808 (2007), p. 1. doi: [10.1016/j.physrep.2006.10.002](https://doi.org/10.1016/j.physrep.2006.10.002). arXiv: [hep-ph/0611040](https://arxiv.org/abs/hep-ph/0611040).
- 3810 [59] Christopher F. Kolda. “Gauge-mediated supersymmetry breaking: Intro-
 3811 duction, review and update”. In: *Nucl. Phys. Proc. Suppl.* 62 (1998), p. 266.
 3812 doi: [10.1016/S0920-5632\(97\)00667-1](https://doi.org/10.1016/S0920-5632(97)00667-1). arXiv: [hep-ph/9707450](https://arxiv.org/abs/hep-ph/9707450).
- 3813 [60] Howard Baer, Kingman Cheung, and John F. Gunion. “A Heavy gluino as
 3814 the lightest supersymmetric particle”. In: *Phys. Rev. D* 59 (1999), p. 075002.
 3815 doi: [10.1103/PhysRevD.59.075002](https://doi.org/10.1103/PhysRevD.59.075002). arXiv: [hep-ph/9806361](https://arxiv.org/abs/hep-ph/9806361).
- 3816 [61] S. James Gates Jr. and Oleg Lebedev. “Searching for supersymmetry in
 3817 hadrons”. In: *Phys. Lett. B* 477 (2000), p. 216. doi: [10.1016/S0370-2693\(00\)00172-6](https://doi.org/10.1016/S0370-2693(00)00172-6). arXiv: [hep-ph/9912362](https://arxiv.org/abs/hep-ph/9912362).
- 3819 [62] G. F. Giudice and A. Romanino. “Split supersymmetry”. In: *Nucl. Phys. B*
 3820 699 (2004), p. 65. doi: [10.1016/j.nuclphysb.2004.11.048](https://doi.org/10.1016/j.nuclphysb.2004.11.048). arXiv:
 3821 [hep-ph/0406088](https://arxiv.org/abs/hep-ph/0406088).
- 3822 [63] N. Arkani-Hamed, S. Dimopoulos, G. F. Giudice, and A. Romanino. “As-
 3823 pects of split supersymmetry”. In: *Nucl. Phys. B* 709 (2005), p. 3. doi: [10.1016/j.nuclphysb.2004.12.026](https://doi.org/10.1016/j.nuclphysb.2004.12.026). arXiv: [hep-ph/0409232](https://arxiv.org/abs/hep-ph/0409232).
- 3825 [64] Glennys R. Farrar and Pierre Fayet. “Phenomenology of the Production,
 3826 Decay, and Detection of New Hadronic States Associated with Supersym-
 3827 metry”. In: *Phys. Lett.* B76 (1978), pp. 575–579. doi: [10.1016/0370-2693\(78\)90858-4](https://doi.org/10.1016/0370-2693(78)90858-4).
- 3829 [65] A. C. Kraan, J. B. Hansen, and P. Nevski. “Discovery potential of R-hadrons
 3830 with the ATLAS detector”. In: *Eur. Phys. J.* C49 (2007), pp. 623–640. doi:
 3831 [10.1140/epjc/s10052-006-0162-x](https://doi.org/10.1140/epjc/s10052-006-0162-x). arXiv: [hep-ex/0511014](https://arxiv.org/abs/hep-ex/0511014)
 3832 [hep-ex].
- 3833 [66] Rasmus Mackeprang and David Milstead. “An Updated Description of
 3834 Heavy-Hadron Interactions in GEANT-4”. In: *Eur. Phys. J.* C66 (2010), pp. 493–
 3835 501. doi: [10.1140/epjc/s10052-010-1262-1](https://doi.org/10.1140/epjc/s10052-010-1262-1). arXiv: [0908.1868](https://arxiv.org/abs/0908.1868)
 3836 [hep-ph].

- 3837 [67] ATLAS Collaboration. “Search for massive, long-lived particles using mul-
 3838 titrack displaced vertices or displaced lepton pairs in pp collisions at $\sqrt{s} =$
 3839 8 TeV with the ATLAS detector”. In: *Phys. Rev. D* 92 (2015), p. 072004.
 3840 doi: [10.1103/PhysRevD.92.072004](https://doi.org/10.1103/PhysRevD.92.072004). arXiv: [1504.05162 \[hep-ex\]](https://arxiv.org/abs/1504.05162).
 3841 SUSY-2014-02.
- 3842 [68] ATLAS Collaboration. “Search for charginos nearly mass degenerate with
 3843 the lightest neutralino based on a disappearing-track signature in pp col-
 3844 lisions at $\sqrt{s} = 8$ TeV with the ATLAS detector”. In: *Phys. Rev. D* 88 (2013),
 3845 p. 112006. doi: [10.1103/PhysRevD.88.112006](https://doi.org/10.1103/PhysRevD.88.112006). arXiv: [1310.3675](https://arxiv.org/abs/1310.3675)
 3846 [hep-ex]. SUSY-2013-01.
- 3847 [69] ATLAS Collaboration. “Searches for heavy long-lived sleptons and R-Hadrons
 3848 with the ATLAS detector in pp collisions at $\sqrt{s} = 7$ TeV”. In: *Phys. Lett. B*
 3849 720 (2013), p. 277. doi: [10.1016/j.physletb.2013.02.015](https://doi.org/10.1016/j.physletb.2013.02.015). arXiv:
 3850 [1211.1597 \[hep-ex\]](https://arxiv.org/abs/1211.1597). SUSY-2012-01.
- 3851 [70] ATLAS Collaboration. “Searches for heavy long-lived charged particles
 3852 with the ATLAS detector in proton–proton collisions at $\sqrt{s} = 8$ TeV”. In:
 3853 *JHEP* 01 (2015), p. 068. doi: [10.1007/JHEP01\(2015\)068](https://doi.org/10.1007/JHEP01(2015)068). arXiv:
 3854 [1411.6795 \[hep-ex\]](https://arxiv.org/abs/1411.6795). SUSY-2013-22.
- 3855 [71] ATLAS Collaboration. “Search for metastable heavy charged particles with
 3856 large ionisation energy loss in pp collisions at $\sqrt{s} = 8$ TeV using the AT-
 3857 LAS experiment”. In: *Eur. Phys. J. C* 75 (2015), p. 407. doi: [10.1140/epjc/s10052-015-3609-0](https://doi.org/10.1140/epjc/s10052-015-3609-0). arXiv: [1506.05332 \[hep-ex\]](https://arxiv.org/abs/1506.05332). SUSY-
 3858 2014-09.
- 3860 [72] ATLAS Collaboration. “Search for heavy long-lived charged R -hadrons
 3861 with the ATLAS detector in 3.2 fb^{-1} of proton–proton collision data at
 3862 $\sqrt{s} = 13$ TeV”. In: *Phys. Lett. B* 760 (2016), pp. 647–665. doi: [10.1016/j.physletb.2016.07.042](https://doi.org/10.1016/j.physletb.2016.07.042). arXiv: [1606.05129 \[hep-ex\]](https://arxiv.org/abs/1606.05129).
- 3864 [73] Torbjorn Sjöstrand, Stephen Mrenna, and Peter Skands. “PYTHIA 6.4 Physics
 3865 and Manual”. In: *JHEP* 0605 (2006), p. 026. doi: [10.1088/1126-6708/2006/05/026](https://doi.org/10.1088/1126-6708/2006/05/026). arXiv: [hep-ph/0603175](https://arxiv.org/abs/hep-ph/0603175).
- 3867 [74] *Further ATLAS tunes of PYTHIA6 and Pythia 8*. Tech. rep. ATL-PHYS-PUB-
 3868 2011-014. Geneva: CERN, 2011. url: <https://cds.cern.ch/record/1400677>.
- 3870 [75] Aafke Christine Kraan. “Interactions of heavy stable hadronizing parti-
 3871 cles”. In: *Eur. Phys. J. C* 37 (2004), pp. 91–104. doi: [10.1140/epjc/s2004-01946-6](https://doi.org/10.1140/epjc/s2004-01946-6). arXiv: [hep-ex/0404001 \[hep-ex\]](https://arxiv.org/abs/hep-ex/0404001).
- 3873 [76] M. Fairbairn et al. “Stable massive particles at colliders”. In: *Phys. Rept.* 438
 3874 (2007), p. 1. doi: [10.1016/j.physrep.2006.10.002](https://doi.org/10.1016/j.physrep.2006.10.002). arXiv: [hep-ph/0611040](https://arxiv.org/abs/hep-ph/0611040).
- 3876 [77] W. Beenakker, R. Hopker, M. Spira, and P. M. Zerwas. “Squark and gluino
 3877 production at hadron colliders”. In: *Nucl. Phys. B* 492 (1997), p. 51. doi:
 3878 [10.1016/S0550-3213\(97\)00084-9](https://doi.org/10.1016/S0550-3213(97)00084-9). arXiv: [hep-ph/9610490](https://arxiv.org/abs/hep-ph/9610490).

- 3879 [78] A. Kulesza and L. Motyka. “Threshold resummation for squark-antisquark
 3880 and gluino-pair production at the LHC”. In: *Phys. Rev. Lett.* 102 (2009),
 3881 p. 111802. doi: [10.1103/PhysRevLett.102.111802](https://doi.org/10.1103/PhysRevLett.102.111802). arXiv: [0807.2405 \[hep-ph\]](https://arxiv.org/abs/0807.2405).
- 3883 [79] A. Kulesza and L. Motyka. “Soft gluon resummation for the production
 3884 of gluino-gluino and squark-antisquark pairs at the LHC”. In: *Phys. Rev.*
 3885 *D* 80 (2009), p. 095004. doi: [10.1103/PhysRevD.80.095004](https://doi.org/10.1103/PhysRevD.80.095004). arXiv:
 3886 [0905.4749 \[hep-ph\]](https://arxiv.org/abs/0905.4749).
- 3887 [80] Wim Beenakker, Silja Brensing, Michael Kramer, Anna Kulesza, Eric Lae-
 3888 nen, et al. “Soft-gluon resummation for squark and gluino hadroproduc-
 3889 tion”. In: *JHEP* 0912 (2009), p. 041. doi: [10.1088/1126-6708/2009/12/041](https://doi.org/10.1088/1126-6708/2009/12/041). arXiv: [0909.4418 \[hep-ph\]](https://arxiv.org/abs/0909.4418).
- 3891 [81] W. Beenakker, S. Brensing, M.n Kramer, A. Kulesza, E. Laenen, et al. “Squark
 3892 and Gluino Hadroproduction”. In: *Int. J. Mod. Phys. A* 26 (2011), p. 2637.
 3893 doi: [10.1142/S0217751X11053560](https://doi.org/10.1142/S0217751X11053560). arXiv: [1105.1110 \[hep-ph\]](https://arxiv.org/abs/1105.1110).
- 3894 [82] Michael Krämer et al. *Supersymmetry production cross sections in pp collisions*
 3895 *at $\sqrt{s} = 7 \text{ TeV}$* . 2012. arXiv: [1206.2892 \[hep-ph\]](https://arxiv.org/abs/1206.2892).
- 3896 [83] Rasmus Mackeprang and Andrea Rizzi. “Interactions of Coloured Heavy
 3897 Stable Particles in Matter”. In: *Eur. Phys. J.* C50 (2007), pp. 353–362. doi:
 3898 [10.1140/epjc/s10052-007-0252-4](https://doi.org/10.1140/epjc/s10052-007-0252-4). arXiv: [hep-ph/0612161](https://arxiv.org/abs/hep-ph/0612161)
 3899 [hep-ph].
- 3900 [84] Rasmus Mackeprang and David Milstead. “An Updated Description of
 3901 Heavy-Hadron Interactions in GEANT-4”. In: *Eur. Phys. J.* C66 (2010), pp. 493–
 3902 501. doi: [10.1140/epjc/s10052-010-1262-1](https://doi.org/10.1140/epjc/s10052-010-1262-1). arXiv: [0908.1868](https://arxiv.org/abs/0908.1868)
 3903 [hep-ph].
- 3904 [85] J. Alwall, R. Frederix, S. Frixione, V. Hirschi, F. Maltoni, O. Mattelaer, H. S.
 3905 Shao, T. Stelzer, P. Torrielli, and M. Zaro. “The automated computation of
 3906 tree-level and next-to-leading order differential cross sections, and their
 3907 matching to parton shower simulations”. In: *JHEP* 07 (2014), p. 079. doi:
 3908 [10.1007/JHEP07\(2014\)079](https://doi.org/10.1007/JHEP07(2014)079). arXiv: [1405.0301 \[hep-ph\]](https://arxiv.org/abs/1405.0301).
- 3909 [86] “dE/dx measurement in the ATLAS Pixel Detector and its use for particle
 3910 identification”. In: (2011).
- 3911 [87] ATLAS Collaboration. “The ATLAS Simulation Infrastructure”. In: *Eur.*
 3912 *Phys. J.* C70 (2010), pp. 823–874. doi: [10.1140/epjc/s10052-010-1429-9](https://doi.org/10.1140/epjc/s10052-010-1429-9). arXiv: [1005.4568 \[physics.ins-det\]](https://arxiv.org/abs/1005.4568).
- 3914 [88] Alexander L. Read. “Presentation of search results: The CL(s) technique”.
 3915 In: *J. Phys. G* 28 (2002). [11(2002)], pp. 2693–2704. doi: [10.1088/0954-3899/28/10/313](https://doi.org/10.1088/0954-3899/28/10/313).

3917 DECLARATION

3918 Put your declaration here.

3919 *Berkeley, CA, September 2016*

3920

Bradley Axen

3921

3922 COLOPHON

3923

Not sure that this is necessary.